Machine-learnt design guidelines for axial vanes in Supersonic turbines operating with non-ideal compressible flows

Shubham Jhamb

Technische Universiteit Delft

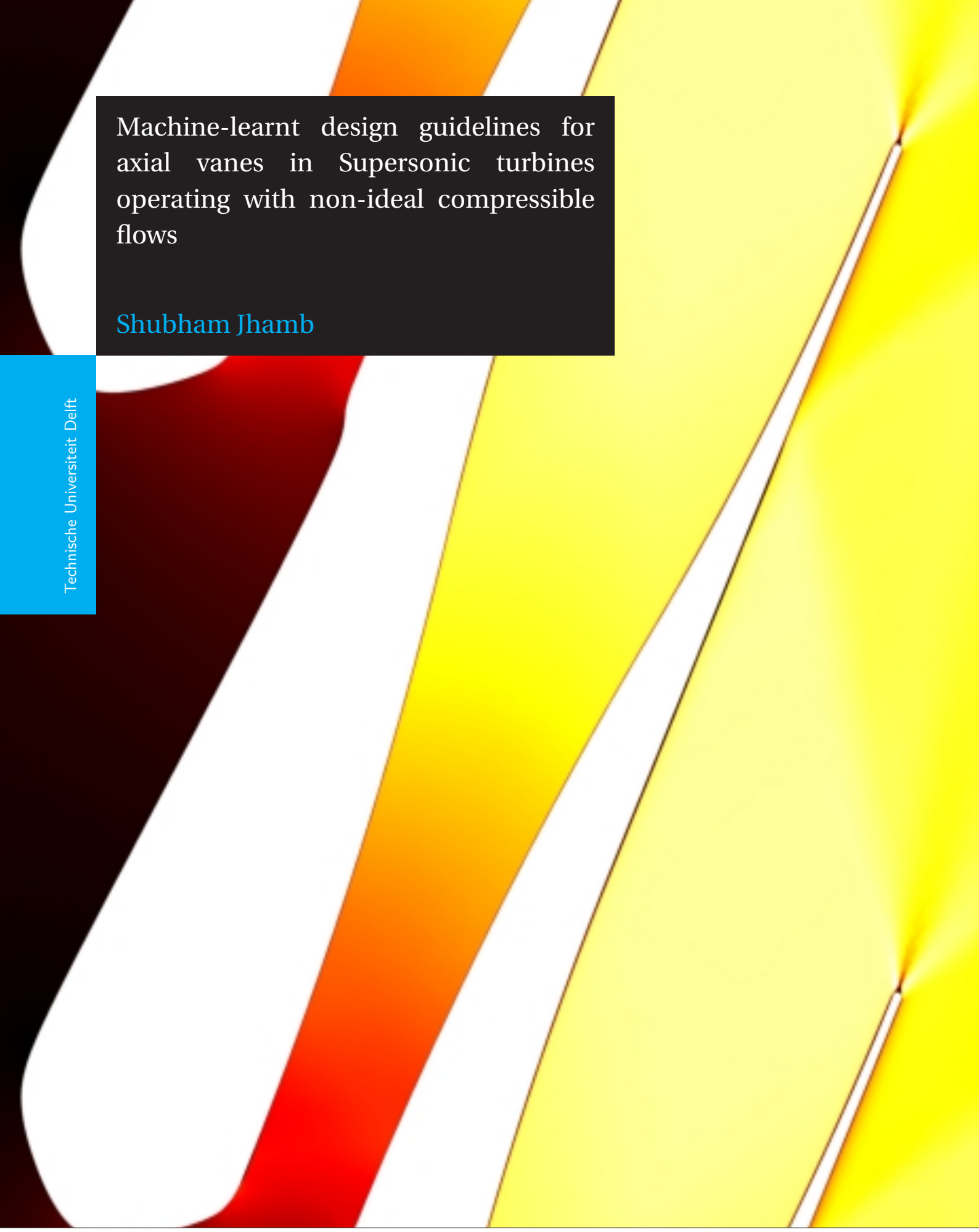

TU Delft Delft University of Technology

Challenge the future

Machine-learnt design guidelines for axial vanes in Supersonic turbines operating with non-ideal compressible flows

by

Shubham Jhamb

in partial fulfillment of the requirements for the course
AE Master Thesis

as a part for the degree of

Master of Science - Propulsion and Power
in Aerospace Engineering

at the Delft University of Technology,

Student number:	4711645	
Project duration:	March 1, 2019 – March 31, 2020	
Supervised by:	Dr. Ir. M. Pini	
	Ir. N. Anand	
Thesis Committee:	Dr. Ir. P. Colonna	TU Delft, Committee Chair
	Dr. Ir. M. Pini	TU Delft, Thesis Supervisor
	Dr. Ir. D. Modesti	TU Delft, External Examiner
	Ir. N. Anand	TU Delft, Daily Supervisor

TU Delft Delft University of Technology

PREFACE

Through the journey of educating myself and gaining knowledge in science and engineering, I found myself in TU Delft, learning about aero-planes and what drives them. My mind was drawn towards Internal Flows which developed my fundamental understanding in fluid dynamics in internal passages. The course of Turbo-machinery captivated me into this field and the lectures and the practical assignment by Prof. Dr. Matteo Pini helped me make up my mind about pursuing this new found interest. After discussing about a number of potential topics for my thesis, I was drawn to the topic of coming up with Design Guidelines for a supersonic turbine in Power and Propulsion applications. I dove into the fundamentals of turbo-machinery and fluid flows in subsonic, transonic and supersonic regimes, which helped me gain insight into underlying flow physics in these complex flow devices. This project led me into a turbulent journey of 12 months, a period through which I learnt and grew multi-dimensionally in time and project management. Through countless nights of burning the midnight oil, inspiring work by esteemed authors and some very illuminating discussions, I managed to give my best effort into delivering this project. This project started with me diving into the fundamentals of fluid dynamics and compressible flows. I then defined the design space needed to explore and created a research framework. To explore this design space and visualize trends from which to conclude, I started honing my coding skills in *Python* and familiarizing myself with existing open source design tools: MoC, AST, UMG2 and SU2 tools. With the help of this predefined toolset, I created my own semi-automated algorithm which could create a blade design and set up a simulation. This algorithm was also capable of validating and post-processing the results with minimal interference from the designer. To perform the simulations, I used the Faculty Cluster and completed the post-processing on my own system.

The learning curve in this project was steep and at the end of all this, I am very glad about undertaking this project and making a contribution to the scientific community. I believe these insights will be a useful guide into understanding and designing efficient unconventional axial and radial inflow turbines. To put all of this work in an easy and fluent to read document was a herculean task. I have made my best effort to make it an interesting read and have put all references in case the reader wants to explore these topics in detail.

This undertaking would have not been possible without the patience and guidance of my daily supervisor Ir. Nitish Anand. His critique and feedback have been essential in shaping this thesis work. I would like to acknowledge Dr. Pini's feedback and help in understanding various topics and results. I find it difficult to visualize the completion of this project without their invaluable help. Throughout this project, my parents (Shrimati Anjali and Sri Virendra Jhamb) and sister (Spardha) have been my bedrock, helping me, supporting and guiding me through the tough times. My friends in Delft have been nothing short of my family and I especially thank Irene, Adithya, Mina, Anurag, Ashwin and Tharun for being there to make my Masters an enlightening and fun experience.

Shubham Jhamb
Delft, March,2020

ABSTRACT

The scientific community is consistently focused on identifying new sources of energy, which can reduce the consequences of climate change and depleting natural resources. Organic Rankine Cycle (ORC) based power systems have been touted as one of the promising technologies of extracting thermal energy from waste-heat and renewable sources such as geothermal, solar radiation and biomass, to name a few. Use of an organic fluid makes it theoretically possible to design a compact, high volumetric flow turbine that can extract energy from sources with low temperature head. However, realization of this turbine becomes challenging because of their unsteady nature which stems from high expansion ratio across the cascade and low speed of sound in organic fluids. The expansion of fluid in these turbines occur in the dense gas supersonic regime where ideal gas assumptions do not hold and the flow is characterized by shock waves and expansion fans. The success of ORC systems thus depends on how well these effects are modeled into the design stage. Stator vanes have a major contribution to the stage losses in these high-expansion low reaction turbines. In current literature, there exists no co-relation that takes into account dense gas effects for the preliminary design of these stator vanes. Thus the objective of this thesis is to study the trend of stator losses with the variation of geometric design variables and inlet conditions, subsequently to qualitatively and quantitatively assess the performance of the blade and finally to propose new design correlations for the organic fluid Toluene. To achieve this objective, the stator design variables affecting 2D loss mechanisms are identified and a design space is constrained. It was hypothesized that the total losses are minimum for an optimum vane design corresponding to a unique value of post-expansion ratio. A semi-automated analysis framework was made, that assessed the fluid dynamic performance of vanes with varying post-expansion ratio, which upon analysis backed the hypothesis successfully. Further, the trend behavior of this optimum post-expansion ratio with design variables such as stator blade angle, total-static expansion ratio, nozzle solidity and fluid non-ideality is investigated and values of post-expansion ratio corresponding to optimum design vanes are obtained. These discrete optimum points are interpolated to obtain a continuous second order function which is the proposed co-relation that can be used for the preliminary design of a stator vane in an ORC turbine.

CONTENTS

List of Figures

List of Tables

NOMENCLATURE

Acronyms

$ADCT$	Automatic Design Chain Tool
$AIDA$	Automatic Identification of Research Trends
CHP	Combined Heat and Power Cycle
DoD	Degree of divergence
HSV	Horse Shoe Vortices
IEA	International Energy Agency
MoC	Method of Characteristics
$Mtoe$	Million Tonnes of Oil Equivalent
$NICFD$	Non-ideal Compressible fluid dynamics
NPS	New Policy Scenario
ORC	Organic Rankine Cycle
PS	Pressure Side
$RMSE$	Root-Mean-Square-Error
SA	Spalart-Allmaras
SS	Suction Side
UMG	Unstructured Mesh Grid

Stations

1	Stator outflow
2	Rotor outflow
a	Nozzle exit
b	Blade exit
o	Nozzle throat
t	Stator inflow

Symbols

β_2^*	Gauging angle
$\beta_{\text{opt, a1}}$	Optimum value of Post-expansion ratio
β_{a1}	Post Expansion Ratio
β_{t1}	Total-static Expansion Ratio
δ^*	Boundary Layer thickness
δ_w	Trailing Edge wedge angle
ϵ	Suction surface curvature
Γ	Fundamental derivative of gas dynamics
γ	Specific Heat capacity ratio
ϕ_{blade}	Metal blade angle
ψ	Deviation angle
ψ_T	Zweifel Coefficient
σ	Nozzle Solidity
θ	Momentum thickness
ξ_{2D}	Kinetic energy loss coefficient
ζ_{2D}	Entropy generation coefficient
$A_{a,o}$	Area ratio of area of nozzle exit to throat
b_m	Mean blade height
C	Chord Length
c	Clearance gap in stator blade and end-wall
C_D	Dissipation Coefficient
C_{pb}	Base Pressure Coefficient
h_{2s}	Isentropic expansion state enthalpy
l	Pitch
L_1	Stator outlet / rotor inlet length [m]
L_A	Nozzle exit cross-section length [m]
L_O	Throat width [m]
M	Mach number
P_t	Total Inlet Pressure
R	Radius of geometry
t	Trailing edge thickness
T_t	Total Inlet Temperature
Z	Compressibility factor

1

INTRODUCTION

This introductory chapter will first describe the context of the thesis, review relevant literature, showcase the motivation and finally frame the objective of this thesis. It will also highlight the contribution of this work to the scientific community.

1.1. WORLD ENERGY OUTLOOK

The most important driver for the modern economy is energy and its security. Nations go to far extents to secure energy such that they can reduce their reliance on others, especially during critical times such as sieges or wars. The source of this energy, for a long time has been fossil fuels, which are a byproduct of mother nature's recycling philosophy. These fossil fuels are energy rich from which energy can be extracted easily and be converted in the requisite usable form. Although the world has seen immense progress thanks to the abundant but fast diminishing supplies, these fossil fuels have their shortcomings too, which have rendered them undesirable today.

Energy extraction from fossil fuels is a combustion based process wherein the energy source is subjected to heat under high pressures to release stored up chemical energy. This chemical energy is in the form of hot gases, of which most are detrimental to the environment and pose greater challenges to the society. Efforts are being put in to introduce sustainable extraction of energy from unconventional resources or increase the efficiency of current systems. In lieu of these effects, studies have been performed to determine the energy growth and usage pattern of the world. The World Energy Outlook, 2018 by IEA lays down the future scenarios of energy usage until 2040 based on New policies by governments of the world. From the study carried out, it is estimated that Natural gas consumption is going to become the second-largest fuel in the energy market globally [6]. Also, the petrochemicals and heavy transportation industry (trucks, planes and ships), keep the overall demand for oil in the upwards trend [6]. These energy extraction procedures are based on combustion and thermal cycles, thus making energy extraction efficiency a major priority. The push for developing energy efficient systems can be seen in the European Energy Commission report which emphasizes that such systems will lead to significant drop in greenhouse gases along with an increase in jobs [7]. A step towards realizing this 30% increase in energy efficiency is by harnessing low grade waste heat from these thermal cycles. Investigations into this waste heat suggests that it accounts for more than 50% or more of the total heat generated in the power generation industry and due to lack of recovery methods, is discarded away, causing thermal pollution [8].

One of the answers to extracting this low grade waste heat is using Organic Rankine cycles (ORCs). They can be used to improve the efficiency of thermal cycles of renewable and non-renewable energy extraction. For perspective, industrial waste heat energy in the USA alone amounted to 5.4e5 MWh (2050 PJ) for low, medium and high temperature sources in the year 2008 [9]. This is equivalent to approximately 3% of the total primary energy produced in the same fiscal year in the USA.

1.2. ORGANIC RANKINE CYCLES AND POWER SYSTEMS

An Organic Rankine cycle (ORC) in principle, is like an ordinary Rankine cycle, with the working medium undergoing evaporation (heat addition) and condensation (in a condenser heat-exchanger) at constant pressure condition and expansion (work extraction in an expander) at constant entropy in an ideal cycle. The difference lies in the working medium which is an organic substance instead of water. The figure 1.1 showcases the process flow and the corresponding temperature-entropy diagram for an organic Rankine cycle.

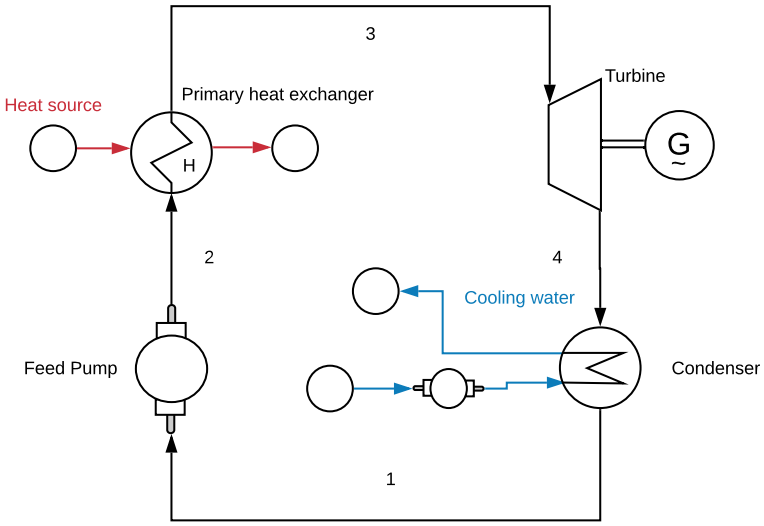

(a)

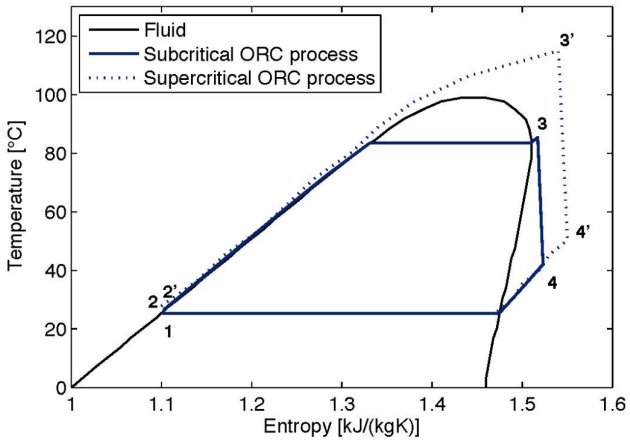

(b)

Figure 1.1: (a) Process flow diagram of an organic Rankine cycle system (b) Temperature-entropy diagram corresponding to the process flow diagram. 1,2 - Pumping fluid; 2,3 - Heat addition; 3,4 - Work extraction; 4,1 - Heat extraction

The use of an ORC in power systems is advantageous because of the following reasons:

- These systems can be used to extract energy from a thermal source with a low temperature head of $30-500°\ C$ [9].
- One of the most important advantage can be observed in the TS diagrams of the working medium. The value of $\frac{\partial S}{\partial T}$ at the mixture vapor boundary is negative for steam while it is positive or infinite for organic fluids (figure 1.1b). Hence, during expansion, these fluids remain in the superheated region which prevents formation of liquid particles that can cause potential erosion to the blades.

- The flexibility of choosing a suitable working fluid allows the designer to match the temperature profiles of the thermal energy source and sink with the corresponding heating and cooling cycles [9].
- Steam does not effectively lubricate the contact surfaces of the expander, due to which a lubricant is added. This lubricant could be prone to thermal decomposition under high temperature conditions. This is not the case for several ORC working fluids as they are suitable for lubricating the contact surfaces of the expander [9].
- As for the disc losses (proportional to surrounding vapor pressure), a suitable organic fluid can be chosen which has a sufficient low vapor pressure[10].

1.2.1. APPLICATIONS

ORC Power systems are versatile and can be adopted for the conversion of several types thermal renewable and non-renewable energy sources. They also have a relatively high conversion efficiency in the lower power range. The conversion efficiency of ORC bottoming cycles in thermal cycles is approximately 5%[9]. This gives access to almost 13,370 Mtoe (1.59e5 TWh)of energy (as waste heat accounts for 50% of the total heat energy produced) of which 5% (795 TWh) is equivalent to the total energy consumption of Russia in 2017 [11]. The energy market has other upcoming options for ORC systems to harness waste heat such as Geothermal Reservoirs, Waste Heat Recovery, Solar Radiation, Solid Biomass or biogas combustion and Flue gas from combustion cycles.

1.2.2. CHALLENGES TO OVERCOME

- Real gas effects- Organic liquids in ORC turbines operate in the vapor saturation limit. In this region, the organic fluids evolve through thermodynamics states which are heavily characterized by dense gas effects. The dynamics of this flow is given by a thermodynamic property - Fundamental Derivative [12] used in gas dynamics:

$$\Gamma = \frac{\tilde{v}^3}{2\tilde{a}^2}\frac{\partial^2 \tilde{p}}{\partial \tilde{v}^2}\bigg|_{\tilde{s}}, \tag{1.1}$$

  where $\tilde{s}$ are isentropes in the pressure ($\tilde{p}$) - specific volume ($\tilde{v}$) diagram and $\tilde{a} = \sqrt{-\tilde{v}^2(\partial \tilde{p}/\partial \tilde{v})_{\tilde{s}}}$, is the speed of sound. This equation or fundamental derivative is a measure of the rate of change for the local speed of sound. During isentropic compression, Γ is greater than 1 for perfect gases, which means the speed of sound increases. But for heavy or complex fluids, Γ is less than one, which means, with compression, speed of sound decreases[13].
  It has been observed that the real gas effects such as deviation from the idea gas law (quantified by the compressibility factor), is maximum in the stator vanes. This deviation is also observed in properties such as the specific capacity at constant pressure (C_p) by [-15%,5%] and thermal conductivity (λ) by [-25%,10%]. The above observations show that, the success of ORC turbines in various applications is dependent on how well the real gas effects are modeled into their design. It is important to correctly model the temperature dependencies of the transport properties [14].
- Organic Fluids are subject to thermal decomposition in high temperature applications. Work on working fluids which are stable under such conditions is ongoing.
- High expansion, low degree of reaction ORC turbines feature non-ideal compressible effects in the flow domain which are practically confined to the stator stage. Thus the challenge is formulating a design methodology for the stator stage taking into account these NICFD effects.
- The conversion efficiency of ORC systems below a few kW is too low for economic viability.

1.3. RESEARCH FRAMEWORK

This section, lays down the framework within which this thesis project was shaped and the objectives were achieved. It first states the problem statement, refers to relevant literature and knowledge acquired from them, lays down the objective and the research questions necessary for the objective, states the contribution to the scientific body of knowledge and showcases the outline of the report.

1.3.1. STATE OF ART LITERATURE REVIEW

In an ORC turbine, several design complications arise which have been listed in the section 1.2.2. To overcome the challenges in designing an efficient and commercial turbine for ORC applications, a knowledge gap into the design laws needs to be filled and a thorough study into the NICFD effects needs to be conducted. The literature review identifies this knowledge gap in the following sections.

MOTIVATION AND RESEARCH GOALS

The design of stator blades in ORC turbines are critical as these vanes account for more than 66% of the stage losses [14]. There persists a knowledge gap here since, in current literature, there are no design laws that can take into account non-ideal compressible fluid dynamic (NICFD) effects and propose a preliminary stator design corresponding to minimum losses based on the design variables of degree of divergence or nozzle exit Mach number. In the present design scenario, correlations between stage design parameters and performance are for subsonic or low-transonic gas turbines. The design of a nozzle and it's flow physics differs as the regime changes from subsonic to supersonic. Further complications arise due to the NICFD effects. Thus currently, correlations that were developed for gas turbine design are used and an optimal design of a stator blade is derived from expensive optimization algorithms that use high-fidelity CFD models. The only existing model that attempts to define the optimum degree of divergence (DoD) of a nozzle (ratio of nozzle outlet section length to throat section length) as a function of the nozzle exit mach number is formulated in the work of Deich et. al [15]. The model proposes this relation under the assumption of a perfect gas. In the work of N. Anand et. al [16], the accuracy of this empirical correlation is investigated by comparing the optimum value of DoD from it, with those obtained from analytical and numerical methods. Through this work, it has been established that an optimum vane geometry exists, which can be characterized by a unique value of the design variable- post-expansion ratio (β_{a1}). The value of β_{a1} corresponding to minimum total loss is $\beta_{opt,\,a1}$. In [16], it is showcased that the empirical method fails to predict the accurate value of the $\beta_{opt,a1}$ as obtained from analytical and computational methods. These methods predict a value for $\beta_{opt,a1}$ as greater than one, depending on the working medium. In the preliminary design stage of the stator itself, a designer with the knowledge of $\beta_{opt,a1}$ variation with respect to design variables, can generate a nozzle which expands the working fluid with minimum losses. A mathematical correlation would be the most effective way of capturing the trends. To propose a design correlation, more cases need to be analyzed by varying the stator design variables.

The following figure 1.2 showcases the existing design methodology for stator vanes and highlights the knowledge gap, this work intends to fill. The preliminary stage sizing is performed with the help of local dimensionless coefficients - λ, ϕ and r which are the load coefficient, flow coefficient and degree of reaction of the turbine stage. λ is used to set the working capacity of the stage, ϕ the flow capacity and r the expansion in the rotor and hence the stator. These coefficients help define the specific diameter and hence size the turbine stage. Using them, the stage efficiency can be extracted from Smith charts. The sizing step is followed by the preliminary stator stage design.

As mentioned previously, design correlations for this preliminary stage design that take into account NICFD effects have not been formulated. To formulate such correlations, a sensitivity analysis of the design variable of post-expansion ratio (β_{a1}) corresponding to the optimum vane design is carried out with respect to flow non-ideality. To analyze the NICFD effects, three cases with different inlet thermodynamic conditions are considered which exhibit varying degree of non-ideality. The trend for this analysis is obtained by constructing various vane geometries using pre-identified primary and secondary design variables for each inlet condition as shown in figure 1.2. β_{t1} is the expansion ratio across the blade, ϕ_{blade} the stator blade angle, γ the specific heat capacity ratio, σ the nozzle solidity and $[P_t, T_t]$ is the thermodynamic state at the inlet. Furthermore, variation of the flow deviation angle (ψ) with respect to these design variables is captured which helps generate the exact velocity triangles of the stator and rotor. The values of post-expansion ratio and flow deviation angle, corresponding to optimum vane design are assimilated for each inlet condition. Surrogate modeling using ML techniques is applied to obtain two sets of correlations for each inlet condition as can be seen in the figure. These correlations and related knowledge can be further used in the preliminary rotor

design and the detailed design phase. This motivation helps define the research objectives of this thesis in the following section.

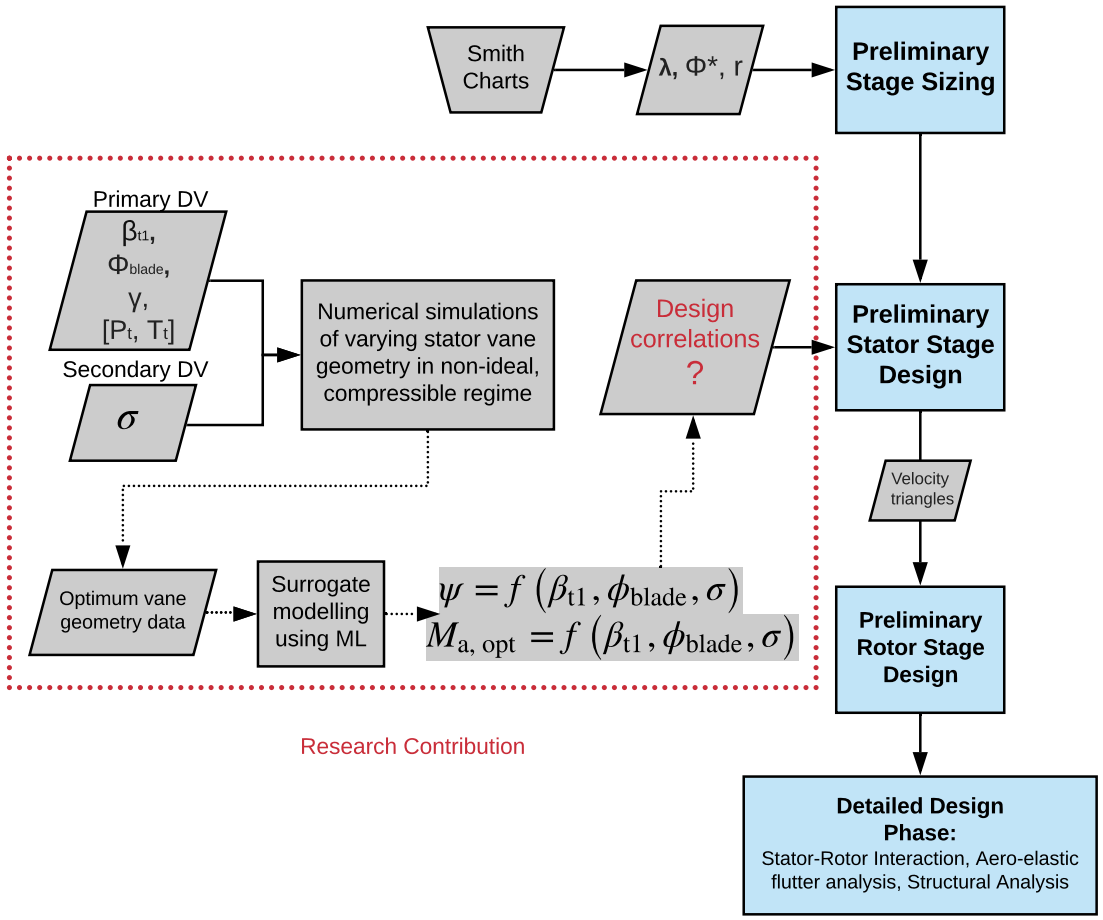

Figure 1.2: Research contribution to the preliminary stator design phase in the existing Design Chain.

1.3.2. RESEARCH OBJECTIVES

The objectives of this thesis are:

- To identify the relevant two-dimensional loss mechanisms in the stator blade.
- Perform a sensitivity analysis of the stator performance with respect to the $\beta_{a1}, \phi_{blade}, \sigma, \beta_{t1}$ and inlet conditions; and provide physical understanding for this behavior.
- Finally propose correlations between the optimum geometry of the stator vane and the identified design variables.

1.3.3. RESEARCH QUESTIONS

From the stated objectives, the main research question that can be posed is

I. *What is the sensitivity of the optimum value of post-expansion ratio with respect to the identified design variables for the proposal of design correlations?*

   which leads to the following sub-questions,

   i. Do these design correlations correspond to the hypothesis that an optimum value of post expansion ratio exists due to trade-off of loss mechanisms?

ii. How do individual loss mechanisms and their contribution qualitatively affect the trend of the optimum value of post-expansion ratio with respect to design variables?

iii. In the trend analysis, are geometrical and flow condition constraints met to isolate the effect of design variable post-expansion ratio on the stator performance?

iv. What is the accuracy (RSME values), between the proposed correlation and the actual design datapoints?

1.3.4. ORIGINAL CONTRIBUTION

The work performed in this thesis is among the first attempts to study unconventional turbines fundamentally and propose design correlations. This study, reviewed the present analytical methods of loss correlations based on which a design space was identified. To conduct this project, a semi-automatic framework was developed with open-source tools to build and simulate different blade configurations under varying conditions. Extensive computational resources helped analyze the defined design space and generate useful trends to propose design recommendations. Thus, the results presented from this work are a novel addition to the existing scientific literature. The main contribution of this thesis can be summed up as:

- The trend of the total, nozzle and post-expansion losses with respect to β_{a1} is established and a mathematical relation between optimum vane design and post-expansion ratio is formed.
- Behavioral trends of $\beta_{opt,a1}$ with respect to the design variables $\beta_{t1}, \phi_{blade}, \sigma$ and inlet conditions are analyzed. Corresponding to the $\beta_{opt,a1}$ values obtained, a correlation between $M_{a,opt}$ and the design variables is proposed. This correlation is available to a designer for calculating the optimum value of M_a ($\beta_{opt,\,a1}$ or degree of divergence interchangeably) for a stator blade.
- The sensitivity of the flow-deviation angle corresponding to optimum blade design, with respect to the design variables and the inlet conditions has been documented.
- The underlying physical phenomena for the trends have been studied, discussed and explained within this thesis.

1.4. REPORT OUTLINE

The report has a simple structure with all relevant information presented. Following the introduction, Chapter 2 will present the theoretical background to understand the fundamentals of Turbo-machinery and its loss mechanisms, discuss non-ideal effects of dense gases and finally formulate a hypothesis. Subsequently, Chapter 3 showcases a Parametric study conducted to identify relevant design parameters. The design space is defined and is followed by the design methodology adopted. Due to the presence of a large number of design and analysis tools, a validation setup is showcased. Once the entire approach to the objective of this thesis is presented, a thorough discussion on the results is presented in Chapter 4. Finally, the conclusions from this work is presented in Chapter 5 with a set of Design recommendations for the designers and another set for researchers who are interested in pursuing this line of work further. Post the set of references, the appendices follow which help understand various concepts in the report without breaking the flow of reading.

2

THEORETICAL BACKGROUND

Turbo-machines are mechanical devices which are primarily used to convert the Total Energy of a working fluid into mechanical energy and vice versa for various applications. They can be divided into two categories depending on their use, with the first category being Turbo-machines primarily used for production of power eg: Gas Turbines, Steam Turbines and Hydraulic Turbines. The second category of turbo-machines primarily use external power to increase the pressure (total quantity) of the working medium. The working principle of turbo-machines are exchange of momentum between the working fluid and the turbo-machine blades. The applications of Turbo-machines are immense for eg. In power generation (Rankine Cycle-Steam, Brayton Cycle-(Gas)) or as Pumps and Compressors. Depending on the hydraulic head and flow capacity, axial or radial turbines are used[17]. The focus of this thesis is solely on an Axial Turbine and the losses occurring in the Stator stage.

2.1. AXIAL-FLOW TURBINES

An axial-flow turbine comprises of a static row of blades called the stator, which is followed by a rotating row of blades called the rotor. This comprises of a single stage of the turbine. These blades are individually placed circumferentially around the rotating shaft at a fixed radius such that the flow is axial. Repeating stages forms a cascade which allows the turbine to extract more energy from the fluid. The role of the stator blades is to accelerate the incoming fluid, deflect it and add swirl such that it enters the rotor with the most optimum gauging angle, and provide the rotor with a uniform inlet flow. The function of the rotor is to extract the total energy of the fluid and convert it into rotating kinetic energy of the shaft. Since in a turbine the fluid flow is always accelerating, turbines can handle larger flow deflections (greater than 120°) as compared to compressors. With the figure 2.1, the terminology used in this report and the essential stage parameters are discussed.

The flow deflection angle of the stator, from the figure 2.1 is the difference of α_2 and α_1. The flow deviation angle is the difference of the α_2 and the metal blade angle. The flow deviation is a key parameter, a designer needs to monitor as it changes the velocity triangles and hence the performance of the stage. The essential stage parameters that help a designer size and compare turbo-machines are namely the Load Coefficient (λ), flow coefficient (ϕ) and the Degree of Reaction (r). All these stage parameters are dimensionless quantities. The λ measures the work capacity of the stage. With increase in its value, more is the specific work of the stage accompanied by greater aerodynamic loading. The second stage parameter, ϕ denotes the flow capacity of the stage. With increase in ϕ, the volumetric flow rate through the stage increases. Lastly, r denotes the expansion in the rotor and the stator. Higher the value of r, greater is the expansion in the rotor. All the three stage parameters affect the velocity triangles and thus the performance of the stage and the entire turbine.

In the figure 2.1, the symmetry of the rotor blades can be observed distinctly. This is because it represents the stage configuration of a zero-reaction turbine. These turbines are used largely in Organic Rankine Cycles, rocket engines or in supersonic turbines wherein a compact machine size and high work capacity is required. This is the very application of this thesis study. Hence, the turbo-machines for which the stator is being studied have a zero Degree of Reaction.

$$r = \frac{\Delta h_R}{\Delta h_{TS}}. \tag{2.1}$$

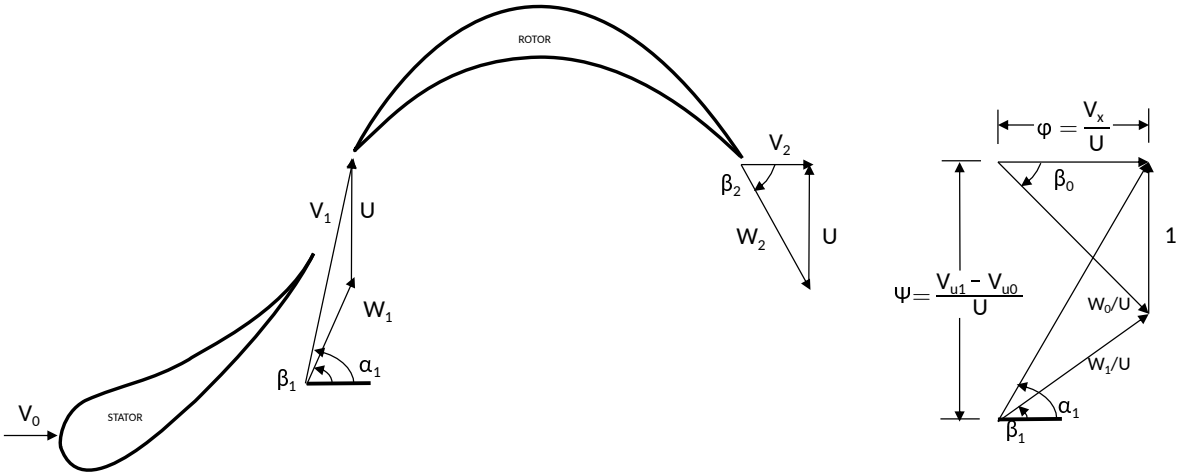

Figure 2.1: Velocity triangles for zero-reaction turbine stage [1]

From the equation 2.1, we know that a zero degree of reaction stage is wherein the static enthalpy drop across the rotor is zero. The entire enthalpy drop of the stage occurs across the stator. This is one reason, analysis of the flow across the stators becomes paramount. Also, in a supersonic turbines, the contribution of loss in the stator towards the total losses is higher than the rotor. This can be seen in the figure 2.2.

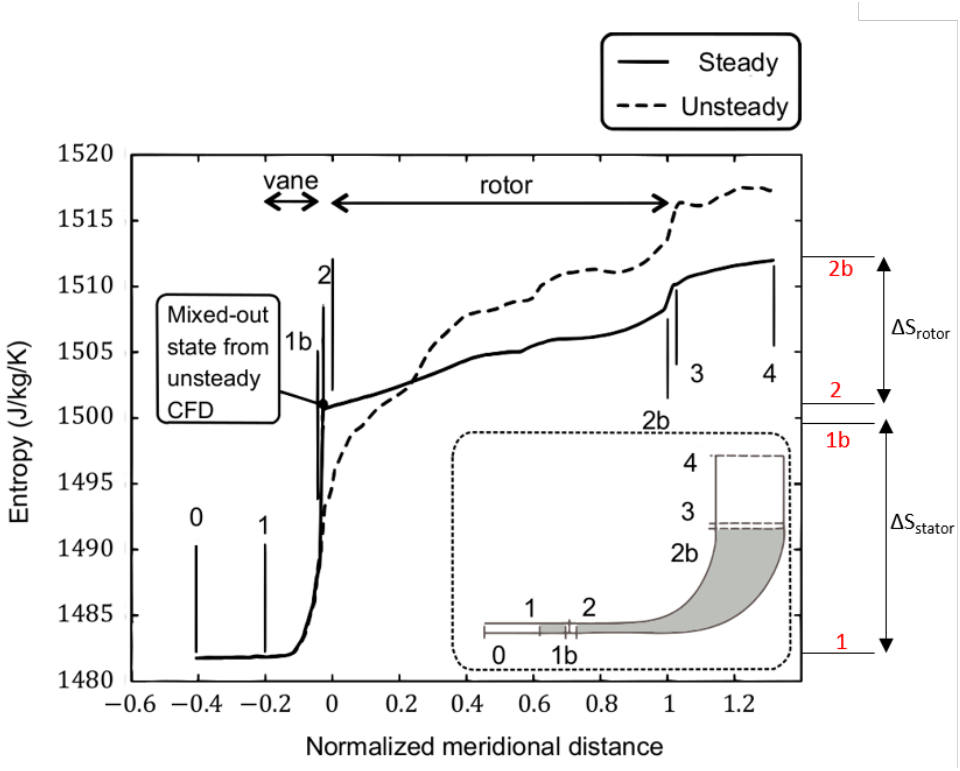

Figure 2.2: Loss Contribution of Stator and Rotor [1]

The variation of $\beta_{\text{opt, a1}}$ with respect to $\phi_{\text{blade}}, \beta_{01}, \sigma, [P_0, T_0]$ is studied by changing the stator and nozzle geometry along with the flow conditions. To maintain the similarity criteria within this design space, these local dimensionless coefficients are kept invariant throughout the study.

2.1.1. REVIEW OF NOZZLE SHAPES

The shape of a nozzle can be converging, diverging or converging-diverging depending upon the function and the application. Plane nozzle in the subsonic region are designed as converging while those for supersonic regimes (M_a>1), are designed as convergent-divergent nozzles. In the transonic regime for M_a<1.4, a purely converging bladed channel is used, as the flow becomes supersonic in the semi-bladed region due to after-expansion. For higher Mach numbers, a converging cascade leads to production of strong shocks and results in flow deviation which further is detrimental to the rotor efficiency[18]. A detailed comparison study was made for a converging cascade operating at the same Expansion ratio, at two different Nozzle Exit Mach numbers. It was depicted that at higher M_a (>1.4), both the flow deviation and the loss coefficient are found to be significantly higher [1]. Thus for M_a >1.4, converging -diverging nozzles are used. The converging portion accelerates the subsonic flow, Mach 1 is achieved at the throat and the diverging portion accelerates the supersonic flow. The area ratio of the diverging part of the nozzle can be given as:

$$\frac{A}{A*} = \frac{1}{M^2}\left[\frac{2}{\gamma+1}\left(1+\frac{\gamma-1}{2}M^2\right)\right]^{\frac{\gamma+1}{\gamma-1}}. \tag{2.2}$$

The asterisk represents properties of flow at sonic conditions. By analysis of this equation, it can be concluded that there exists one Mach number and hence one nozzle outlet and throat area ratio, for which the required total expansion ratio can be achieved if one of the back pressure or the inlet pressure is specified.
The figure 2.3, showcases different nozzle shapes and the regimes in which they operate most efficiently.

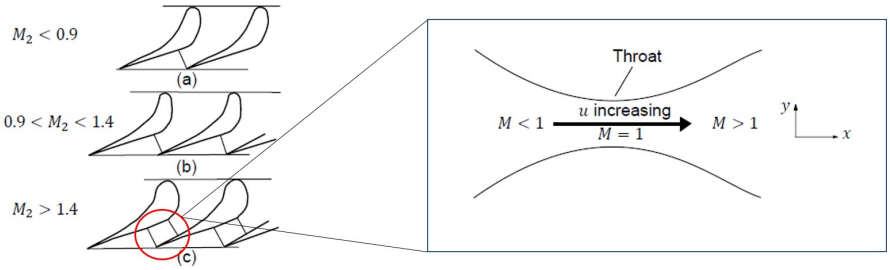

Figure 2.3: Visualization of different Nozzle Shapes adapted from [2]. (a) Convergent Nozzle for subsonic cascade (b) Convergent nozzle for transonic cascade (c) Convergent Divergent nozzle for supersonic regime.

2.2. PERFORMANCE ESTIMATION

2.2.1. LOSS COEFFICIENTS

The origins and estimation of loss in turbo-machinery is discussed in detail in this section. "*Loss is any flow feature that reduces the efficiency of a turbo-machine.*". This excludes those factors that reduce the cycle efficiency. The mechanisms of loss have been studied critically over the past quarter of the century, thanks to the advent of new instrumentation (laser anemometry and hot wire), along with powerful computers who use numerical models to analyze the flow and associated losses.These losses are broken down into components: **Profile Loss, Endwall Loss, Tip-Leakage Loss and miscellaneous loss**.

Profile loss is the irreversibility which occurs in the boundary layer of the stator/rotor vane, at a significant distance from the end wall. The Trailing Edge and Mixing loss is combined together with other profile losses as the basic cause of the loss is due to internally acting viscous forces.

End-wall losses are due to secondary flows that are generated when annulus boundary layers move across a blade row, separates in the adverse pressure gradient and forms a rolled up vortex also known as a Horse Shoe Vortex (HSV). The pressure side HSV (HSV-PS) is driven across in the pitch-wise direction and interacts with the suction side HSV (HSV-SS) of the adjacent blade. The two vortices are counter-rotating due to which high dissipation rates are seen in this region [19]. Secondary flows are caused by other factors which makes it difficult to distinguish from profile and leakage losses.

Tip leakage losses are caused due to leakage of the working medium over the tips of the clearance space over stator blades and over that of rotor blades. They are strongly dependent on whether the blades are shrouded or unshrouded. Also it depends upon the ratio of the clearance gap to the average vane height. The following equation gives the relation between the loss in specific work and is-entropic specific work in the

turbine stage[20].

$$\Delta h_c = \Delta h_0(c/b_m). \tag{2.3}$$

Results of the developments of several researchers and designers have been assimilated, and it can be seen that most of the practical performance prediction methods are based on co-relations. The issue with these co-relations are that they are outdated and cannot be used to explain new design features developed recently. The focus of this section will be to elaborate the flow physics and the loss mechanisms (particularly its origin), to enable the reader to understand and use their judgment to design any component of a turbine[21].

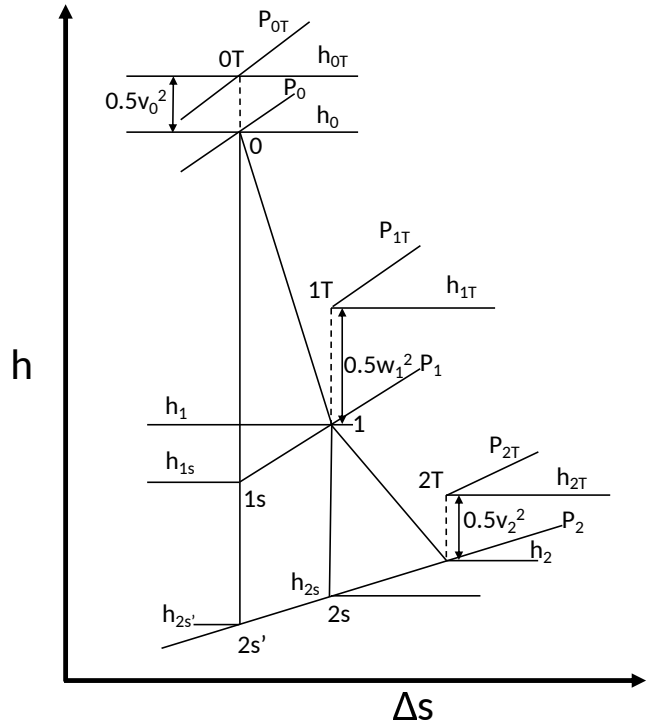

Figure 2.4: Enthalpy-entropy diagram for an expansion process in a turbine stage [3].

To begin with, estimation of loss is an important concept that should be clarified. Loss coefficients are the basic non-dimensional parameters used to quantify the loss. The most useful loss coefficient for design purposes was the enthalpy/energy loss coefficient given by:

$$\zeta = \frac{h_2 - h_{2s}}{h_{02} - h_2}. \tag{2.4}$$

This applies for a turbine blade. The above equation is not necessarily applicable to rotating blade rows wherein, the stagnation enthalpy or pressure is a function of the radius of the flow. This change in stagnation enthalpy does not contribute to the a change in is-entropic efficiency. Change in is-entropic efficiency is either due to heat transfer or any thermodynamic irreversibility. For adiabatic machines, irreversibilities are the sole reason for loss of efficiency. Hence, entropy is the best measure for calculating the loss coefficients. Also, the loss coefficient thus does not change based on the frame of reference. The entropy loss coefficient is defined as:

$$\zeta_s = \frac{T_2 \Delta S}{h_{02} - h_2}. \tag{2.5}$$

From the figure 2.4, a relation between the enthalpy and entropy loss coefficients can be made. This is given by the following equation:

$$\zeta_s - \zeta = 0.25(\gamma - 1) M^2 \zeta \zeta_s. \tag{2.6}$$

It can be observed that the relation between the two coefficients depends upon the Mach number. For the same liquid, if the flow becomes compressible ie. when M exceeds 0.3, the differences between the coefficients become significant. For Mach numbers less than 0.3, they can be treated interchangeably.

In the Supersonic Regime, the **Entropy Loss Coefficient** is decided to be the primary quantity for estimating loss in a flow domain.

2.2.2. LOSS BREAKDOWN

There are three significant fluid phenomena, as predicted by thermodynamics, which cause entropy production in turbines:

- Friction due to viscous forces acting in boundary layers or free shear layers (mixing streams).
- Non-equilibrium processes (shock waves or rapid expansions).
- Heat transfer across a temperature gradient ie. across a hot stream and a coolant gas flow.

These mechanisms help classify the broad categories of losses further which are shown as in the figure 2.5.

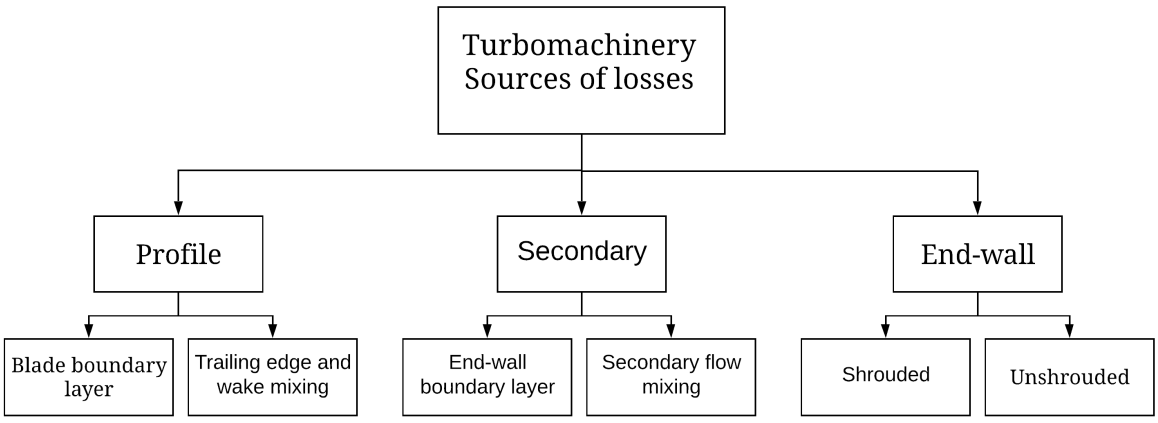

Figure 2.5: Classification of loss mechanisms in a turbine. Adapted and regenerated from [2].

The scope of this thesis is studying 2 dimensional losses in a supersonic vane. Hence, the focus will be largely on the **Profile Losses** which consist of Blade Boundary Layer Loss, the Trailing Edge Loss, the Wake Mixing Loss along with Shock losses. To pinpoint which design variables affect these loss mechanisms, relations for the loss coefficients were studied.

BLADE BOUNDARY LAYER LOSS

Viscous dissipation occurs in the boundary layer region near the walls of the stator. An expression for the rate of change of entropy flux can be derived assuming turbulent conditions for a 2D flow and is expressed as:

$$s_{irr} = \frac{d}{dx}\int_0^{\delta} \rho u(s - s_{\delta})dy. \tag{2.7}$$

This expression derived from [21] calculates the loss generated in the control volume as defined by the integral. Here δ is the thickness of the boundary layer which is at the point where the local fluid velocity is found to be 0.99 times that of the free-stream velocity. This rate of entropy generation is rewritten as a dimensionless coefficient called the dissipation coefficient, which is given in [21] as:

$$C_d = \frac{T\dot{s}_{irr}}{\rho v_{ref}^3}. \tag{2.8}$$

The state of the boundary layer defines the value of this coefficient. Experimental work has led to a widely used recommended value of 0.002 for this dissipation coefficient in case of turbulent boundary layers [22]. A boundary layer loss coefficient is used to quantify these losses which is given by:

$$\zeta_{BL} = \frac{\bar{h_2} - \bar{h_{2s}}}{\bar{u}_{2s}^2}. \tag{2.9}$$

This equation can be further written as,

$$\zeta_{BL} = \frac{\dot{m}\delta h}{0.5\dot{m}u_{ref}^2} = \frac{\int \dot{m}Tds}{0.5\dot{m}u_{ref}^2} = \frac{T\dot{s_{irr}}}{0.5\dot{m}u_{ref}^2} = \frac{\int C_d \rho u_\delta^3}{0.5\dot{m}u_{ref}^2}. \tag{2.10}$$

The estimation of the blade boundary layer state is essential to determine the velocity profile in the boundary layer. An idealized velocity distribution is considered based on the assumption of incompressible flow as shown in the figure 2.6. Based on this, the numerator in equation 2.10 can be written as:

$$\int C_d \rho v_\delta^3 = C_d \sum_{PS+SS} \int_0^1 \rho u_\delta^3 d\frac{x}{c} = C_D \rho C(2\bar{u^3} + 6\bar{u}\delta\bar{u^2}). \tag{2.11}$$

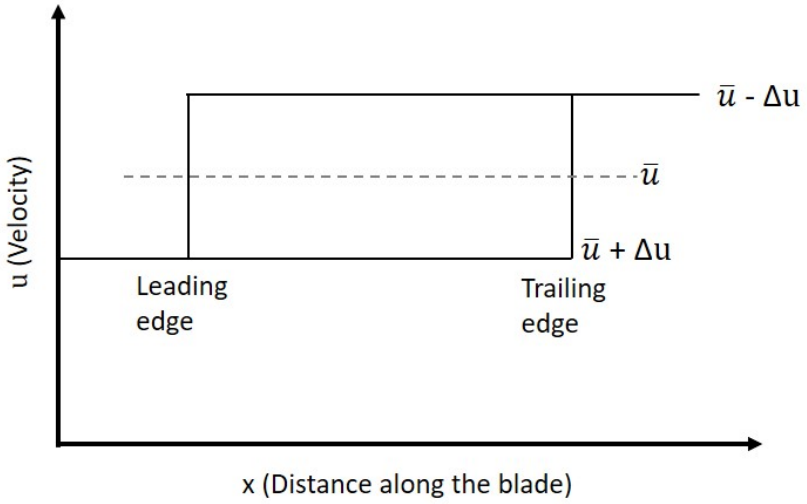

Figure 2.6: Boundary Layer Velocity Profile. Adapted from [4]

Hence, the equation for the boundary layer coefficient is of the form:

$$\zeta_{BL} = = \frac{C_D\ \rho\ C\ (2\bar{u}^3 + 6\bar{u}\delta\bar{u}^2)}{0.5\dot{m}\bar{u}^2} = \frac{C_D\ \rho\ (2\bar{u}^3 + 6\bar{u}\delta\bar{u}^2)}{0.5\dot{m}\bar{u}^2}\frac{C}{L}. \tag{2.12}$$

where C_D - Dissipation coefficient = $0.173Re_o^{-1}$ [Laminar]
= $0.0056Re_o^{-1/6}$ [Turbulent]
where, Re_o is a function of the nozzle outlet mach number M_a

The Reynolds number at the throat plays an important role in defining the flow characteristics and hence the boundary layer. This Reynolds number at the throat is inherently dependant on the Mach number at the Nozzle exit.

Hence, the **Boundary layer loss** depends on

M_a, Solidity, [Mach Distribution along the walls]

BLADE TRAILING EDGE AND MIXING LOSSES

The flow pattern at the trailing edge of the stator consists of interaction of supersonic flow from the suction surface and the pressure surface. This interaction is influenced by a triangular region at the trailing edge of the blade called the **Base Pressure Region**. This can be seen in the figure 2.8. The magnitude of this base pressure is difficult to predict and has been estimated using empirical correlations obtained from [5] which predicts the base pressure as a function of pressure at stator outlet, trailing edge wedge angle and suction surface curvature of the throat. There is formation of shear layers due to the velocity difference between the base pressure region (low velocity-high uniform pressure region) and the upstream flow streams from the PS and SS. These shear layers lead to formation of expansion waves and weak shocks. When the two flows from the suction and pressure side meet, they do so in different flow angles (due to the trailing edge thickness), and hence the flow is forced to turn into a resultant direction. This generates shock waves which propagate into the flow, one in the direction of the suction surface and the other downstream. These shock waves affect the pressure distribution of the blades. Using the aforementioned correlations, this base pressure can be defined with which the inviscid flow pattern can be created using MoC. The entropy loss in the bladed and semi-bladed region can be obtained by a continuity,momentum and energy conservation between the trailing edge and uniform flow downstream ie. the rotor inlet region[23]. The conservation equations have been presented as follows which lead to the formulation of the mixing loss coefficient.

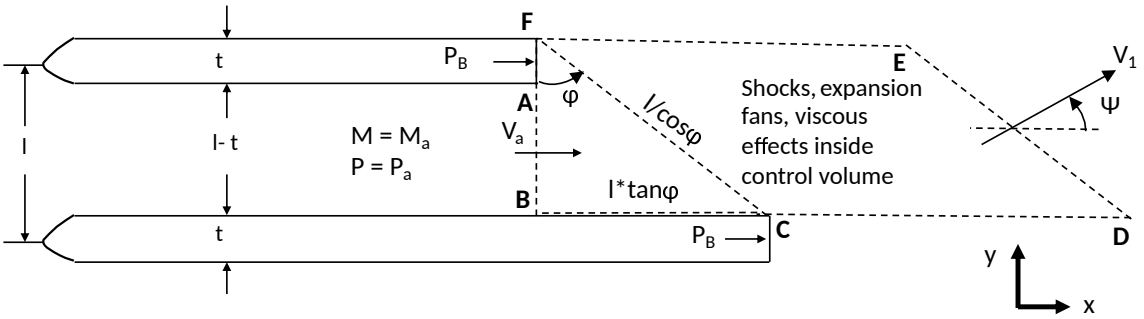

Figure 2.7: Control volume outline for mixing loss coefficient calculation.

The figure 2.7 presents the control volume considered for wake mixing and shock losses in staggered blades. The stagger angle is represented by the variable ϕ, axial pitch by l, trailing edge thickness by t and flow deviation by ψ. This configuration might be different than that of actual stator blade rows, but they do provide a fundamental understanding of the flow phenomena. In this analysis, incompressible flow theory is valid and the trailing edge is assumed blunt. The station 1 in the figure is assumed to be in a fully mixed-out condition. Station a represents the nozzle exit location. The dashed area demarcated by ABCDEF represents the control volume under analysis. This helps formulate the mass and momentum balance equations between station a and 1. At station a, the mass is given by $\dot{m} = \rho V_a (l - t - \delta^*)$, where δ^* is the displacement thickness. Hence the continuity equation is written as equation 2.13.

$$\dot{m} = \rho_a V_a (l - t - \delta^*) = \rho_1 V_1 l (1 + \psi t an \phi). \tag{2.13}$$

The momentum balance in the x-direction follows which is written as:

$$(l - t) P_a + \dot{m} V_a + t P_B - \rho_a V_a^2 \theta = \dot{m} V_1 \cos(\delta) + l P_1. \tag{2.14}$$

Here θ represents the momentum thickness due to the formation of the boundary layer. Using the continuity equation 2.13 and rearranging equation 2.14, the following equation is obtained.

$$(P_a - P_1) = -\rho V_a^2 \left(1 - \frac{t}{l} - \frac{\delta^*}{l} - \frac{\theta}{l}\right) + \rho V_1^2 (1 + \psi \tan\phi) + (P_a - P_b) \frac{t}{l} \tag{2.15}$$

Rearranging to convert static pressure quantity to total quantity, we get,

$$(P_{0a} - P_{01}) = 0.5 \rho V_1^2 (2\psi \tan\phi + 1) - 0.5 \rho V_a^2 \left(1 + 2\left(\frac{t + \delta^* + \theta}{l}\right)\right) + (P_a - P_b) \frac{t}{l} \tag{2.16}$$

To simplify the equation, a base pressure coefficient is introduced which is given by the following equation:

$$C_{\text{pb}} = \frac{P_B - P_a}{0.5\rho_a V_a^2}, \tag{2.17}$$

where, P_B is a function of - (t/l, β_2^*, δ_w, P_1, ϵ) [5].

Using the equations 2.13, 2.14 and 2.17 and normalizing them with $0.5\rho V_a^2$, the following equation is obtained:

$$\frac{P_{0a} - P_{01}}{0.5\rho V_a^2} = \frac{V_1^2}{V_a^2}(2\psi \tan\phi + 1) - 1 + 2\left(\frac{t + \delta^* + \theta}{l}\right) - C_{pb}\frac{t}{l} \tag{2.18}$$

The terms of V_a and V_1 are eliminated by assuming deviation angle is zero. It is justified in Denton [21] that the entropy generation behind a blunt trailing edge is invariant with the stagger angle denoted by ϕ here. Hence the term $(2\delta tan(\phi) + 1)$ is eliminated and the following dimensionless mixing loss coefficient is obtained in equation 2.19.

$$\zeta_{mix} = -C_{\text{pb}}\frac{t}{l} + 2\frac{\theta}{l} + \left[\frac{\delta^* + t}{l}\right]^2. \tag{2.19}$$

Hence, the **Trailing edge and mixing loss** depend on,

$$M_a, \frac{\delta^*}{l}, \frac{t}{l}, \beta_2^*, \frac{\theta}{l}, \frac{A_a}{A_1}.$$

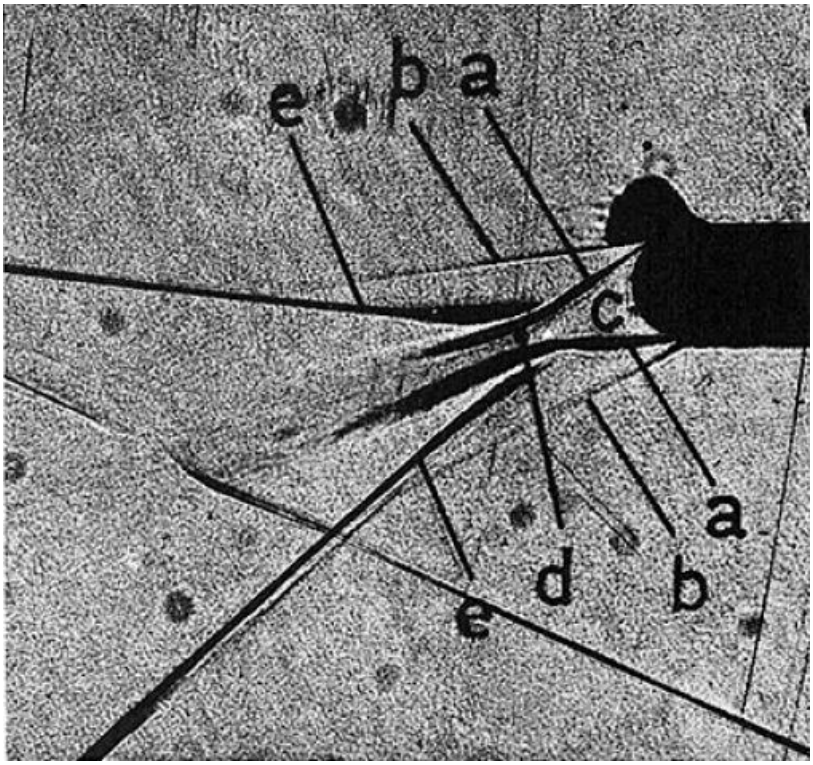

Figure 2.8: Schlieren photograph of trailing edge at limit condition, adapted from [5]
a. Free shear layers b. separation shocks c. dead water region d. reattachment region e. wake shocks.

2.3. FORMULATION OF RESEARCH HYPOTHESIS

The previous sections provide a brief overview into the working and performance of an axial flow turbine. The design parameters that affect the loss mechanisms in the stator stage are laid down and thus pave way for further analysis. The reason for analysis of the stator stage performance with 2D loss mechanisms is also established. This helps to narrow down the focus and formulate a hypothesis based on which this research is carried out. The approach to formulate the hypothesis is adapted from [2]. Figure 2.9 shows the control volume on which the hypothesis is formulated. Station t, o, a and 1 are the stator inlet, nozzle throat, nozzle outlet and stator outlet respectively. Bladed expansion occurs in the region of o-a and the post-expansion in region between stations a-1.

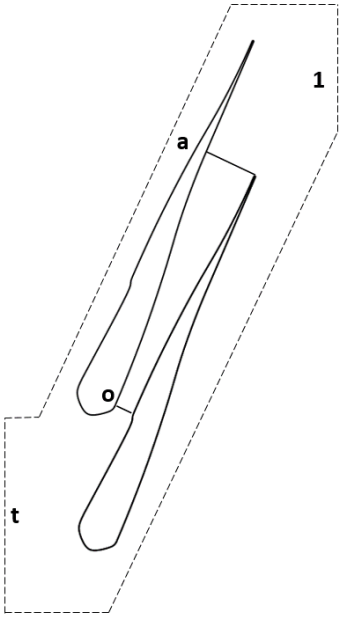

Figure 2.9: Stator stage control volume and associated stations. t-stator stage inlet, o-nozzle throat, a-nozzle exit and 1 is stator stage outlet.

The 2D losses in the stator stage are primarily from the nozzle and post-expansion region. This is given by the following expression:

$$\zeta_{\text{stator}} = \zeta_{\text{2D}} = \zeta_{\text{PE}} + \zeta_{\text{nozzle}} \tag{2.20}$$

From the insight from section 2.2.1, an expression for $\zeta_{\text{PE}} = \tau_{\text{mix}}$ and ζ_{nozzle} can be derived.

$$\zeta_{\text{PE}} = f\left(M_{\text{a}}, \frac{t}{l}, \frac{A_a}{A_1}\right) \tag{2.21}$$

Similarly, the expression for the nozzle losses can be written down as:

$$\zeta_{\text{nozzle}} = f\left(M_{\text{a}}, \frac{C}{l}, Re_{\text{o}}\right) \tag{2.22}$$

Equations 2.21 and 2.22 when inserted in the equation 2.20 give a general expression for 2D losses and it's contributing parameters. It is as follows:

$$\zeta_{\text{2D}} = f\left(M_{\text{a}}, \frac{t}{l}, \frac{A_a}{A_1}\right) + f\left(M_{\text{a}}, \frac{C}{l}, Re_{\text{o}}\right) \tag{2.23}$$

For a single stator, where fixed a fixed blade geometry and constant throat conditions exist, the expression boils down to the following expression 2.23.

$$\zeta_{2D} = \zeta_{nozzle}(M_a) + \zeta_{PE}(M_a) \tag{2.24}$$

From equation 2.24, it can be established that M_a is the design parameter that affects the relevant stator losses provided the bade geometry is fixed. Fluid dynamics tells us that with increasing velocity in the nozzle, hence increasing Mach, the viscous losses in the nozzle region should decrease. Secondly, with increase in Mach, the strength of the shocks in the post expansion region should increase. Due to the contradicting nature of the behavior of the two contributing losses, a trade-off is anticipated between them and stator performance. This means that an optimum value of M_a exists for which the losses in a stator are minimum. The value of M_a directly relates to the post-expansion ratio β_{a1} as if the nozzle exit mach number increases, the value of P_a decreases, due to which the ratio of $P_a : P_1$ decreases. Based on this relation, it can be said that there exists an optimum value of β_{a1}, for which the stator losses are minimum. The trend of loss variation with respect to post-expansion ratio is the opposite. With increase in value of β_{a1}, M_a decreases, hence magnitude of viscous losses increase while PE losses. This hypothesis is visualized in the figure 2.10.

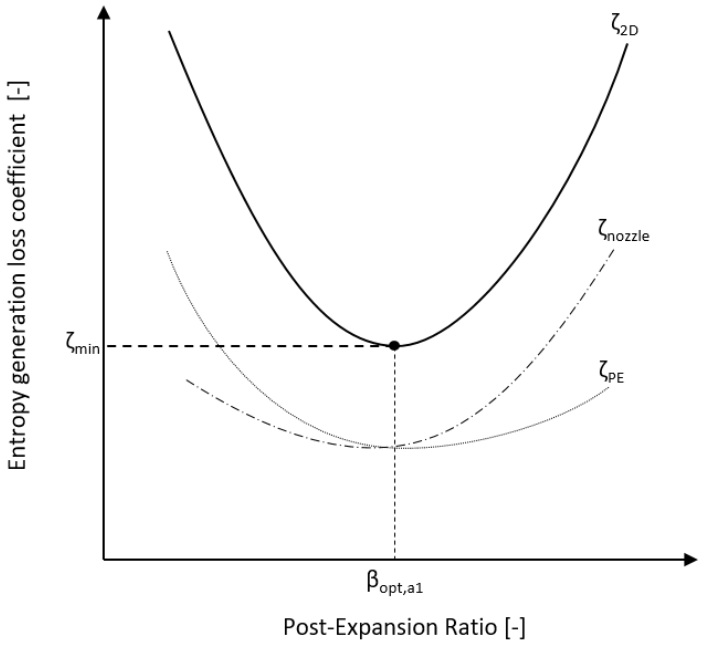

Figure 2.10: An approximate plot of entropy generation loss coefficient vs post-expansion ratio illustrating the existence of a hypothesized $\beta_{opt,a1}$ value.

3

METHODOLOGY

The approach to reach the stated objective in section 1.3.2 while answering the aforementioned research questions is described in this chapter. The investigation is carried out by identifying the geometric and flow variables that affect the two dimensional loss in the stator blade. Once these variables are identified, the design space is constrained. The existing algorithm of designing the nozzle and stator blade, and performing CFD in the flow domain is extended so as to post-process the results and visualize the flow. A module is also added to identify the optimum points and capture the trends of these optimum points. Meanwhile, the algorithm is enhanced with an additional module that validates the various design steps involved. The validation procedure is elaborated in the section 3.5. The extended algorithm is divided in stages so as to separate the function of each stage and bring modularity to the entire design chain. Figure 3.1 shows the various stages in design chain in their successive order.

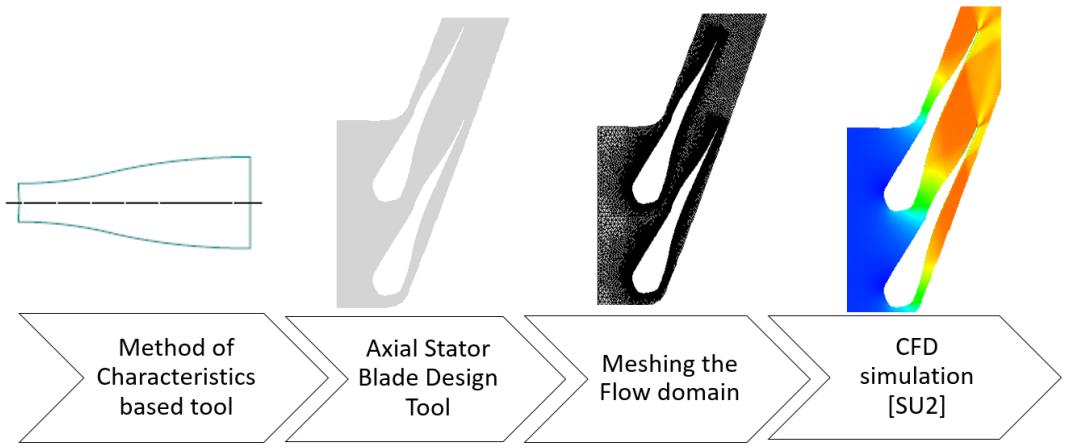

Figure 3.1: Schematic diagram of the design chain of a stator blade used in this project.

3.1. PARAMETRIC STUDY

The objective of this thesis is to investigate the trends of the stator loss for different geometry and flow conditions. From the hypothesis elaborated in section 2.3, a study of the trend of the optimum value of the post-expansion ratio [β_{a1}] with respect to flow and geometric variables is carried out, and finally loss correlations with respect to the identified variables are stated. To identify the variables and to isolate the effect of the post-expansion ratio on the stator losses, a parametric study is carried out.
In the section 2.2.2, mechanisms of 2D loss and their breakdown is described and the contributing flow and geometry variables are highlighted. To reiterate, the boundary layer losses are dependent on nozzle exit

Mach number, solidity and boundary layer Mach distribution while the trailing edge and mixing losses are dependent on nozzle exit Mach number, T.E.thickness/axial pitch, T.E wedge angle, base pressure and post-expansion ratio. To isolate the effect of the post-expansion ratio on the 2D losses, constraints are placed on some of the aforementioned variables for each design case. Hence these variables become design constraints for a single case.

Figure 3.2 visualizes the location of the discussed design variables/constraints and classifies them based on the 2D loss mechanism they effect. Each tool uses a configuration file for specifying the input parameters. The outputs are either stored for post-processing or are used in the subsequent tools. The post-processing module ensures design constraints are met and identifies the values of β_{a1} corresponding to the optimum vane design. Further, it uses a machine learning algorithm to formulate design correlations. As mentioned

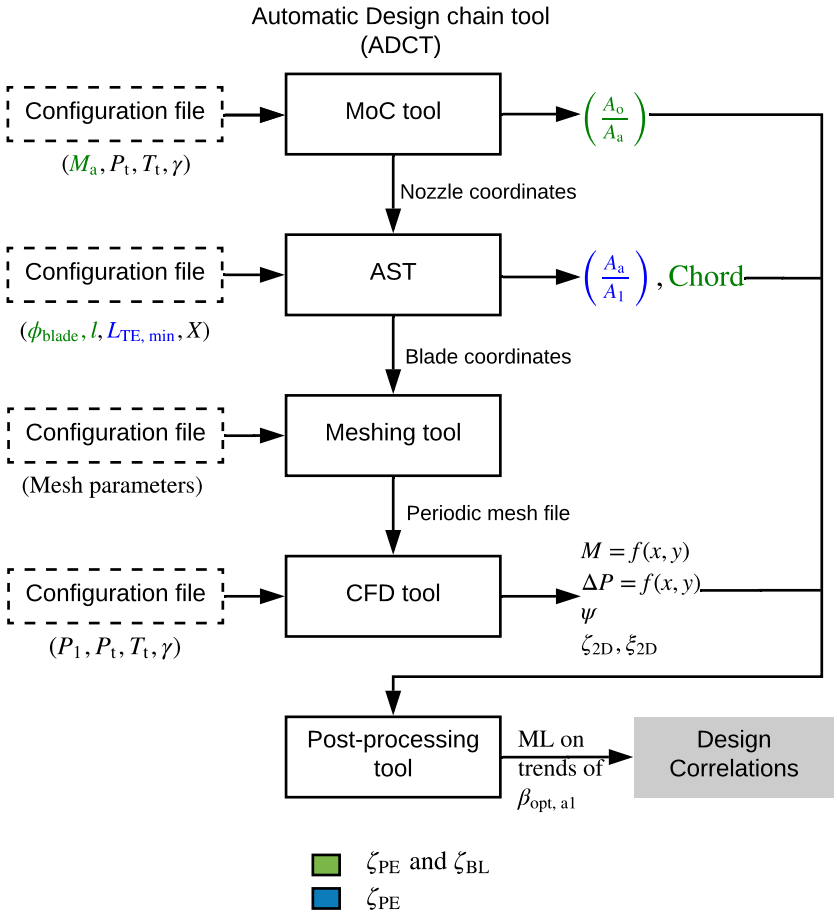

Figure 3.2: Automatic design chain tool with input and output design parameters and variables for each individual sub-tool. Highlighted parameters/variables in green account for boundary-layer and post-expansion (PE) loss; those in blue account for only PE loss. Design correlations are the final output of ADCT.

above, the study of variation of the optimum value of β_{a1} with the 2D loss in the axial stator is carried out by constraining the values of some of the design variables. The search for the optimum point is carried out by varying the post-expansion ratio and calculating the total loss in the stator in terms of the entropy generation loss coefficient. The value of this β_{a1} is varied in the range 0.6- 1.4 as it was previously established that the optimum point of β_{a1} would lie close to the value of 1 [16]. This variation of β_{a1} is carried out by changing the area ratio of the nozzle also called the Degree of Divergence as shown in equation 3.1.

$$\beta_{a1} = f(M_a) \; or \; f(\text{DoD}), \tag{3.1}$$

for constant (ϕ_{blade}, β_{t1}, σ, [P_{t}, T_{t}]). With increase in Degree of Divergence (DoD), the value of nozzle exit Mach number (M_{a}) increases, the nozzle exit pressure (P_a) decreases and consequently the value of β_{a1} decreases. Since $\boldsymbol{M_{\text{a}}}$ is an input to the MoC tool, it is described as a **Primary Design variable**. Meanwhile the rest of the variables are kept constant. Once, for a single case, the optimum value of the post-expansion ratio is identified, the variation of this optimum point with the other design variables becomes of interest. The parameters which affect the performance of a stator blade are the stator blade angle (ϕ_{blade}), nozzle solidity (σ) and total-static expansion ratio across the blade β_{t1}. The expansion ratio could be total to static or a total to total quantity. The former is selected as the variable of interest, as in a cascade, the kinetic energy of the working medium is extracted by the rotor, downstream of the stator. Hence, the parameter of choice becomes the total to static expansion ratio (β_{t1}). Along with these design variables, the choice of inlet conditions also affect the cascade performance. Thus the inlet pressure and temperature are also design variables for the working fluid Toluene as shown in equation 3.2.

$$\beta_{\text{opt,a1}} = f(\phi_{\text{blade}}, \beta_{t1}, \sigma, [P_{\text{t}}, T_{\text{t}}]). \tag{3.2}$$

These design variables that is $\boldsymbol{\phi}_{\text{blade}}$, $\boldsymbol{\beta}_{\text{t1}}$ and the **total inlet conditions** are termed as **Primary Design variables**. Since the nozzle solidity is a derived variable from the ratio of axial pitch and nozzle chord length, σ is the secondary design variable. The behavior of the optimum point with respect to the primary and secondary design variables is carried out by defining a range for them and carrying out corresponding simulations.

3.2. DESIGN SPACE DEFINITION

Once, the design variables are identified and the procedure of investigation is established, the design space is constrained to an exact range. The working medium is an important decision point for defining the design space. An ideal working medium for an ORC expander would satisfy the following criteria: a. have a low Global warming potential (GWP), b. a low ozone depletion potential (ODP), c. a high safety rating (based on flammability, toxicity and corrosive properties), d. be environmentally sustainable, e. high thermal stability and lastly f. a positive slope in the saturated vapor curve. Toluene as a working medium satisfied most of these categories. Although, it has been classified as a hazardous fluid, it is much less toxic than benzene [24]. In comparison to siloxanes, toluene has a much higher decomposition temperature (above 1125°) [25]. Experimental studies based on the thermal stability of siloxanes suggest that they are subject to decomposition in the operating temperature conditions of an ORC cycle. Toluene is a dry working fluid within a large range of thermodynamic conditions. Thus, the decision to base the study on Toluene as the working medium was made.

The first step hence, was to determine the range of M_{a} so as to investigate the optimum value of β_{a1}. The value of M_{a} can be either obtained by using is-entropic equations (does not mimic the real fluids) or by trial and error through various nozzle shapes and CFD simulations. For constraining the range of M_{a}, the is-entropic relation shown in the equation 3.3 is used.

$$\frac{P_{\text{a}}}{P_{\text{o}}} = \left[1 + \frac{\gamma - 1}{2} M_a^2\right]^{\left(\frac{-\gamma}{\gamma - 1}\right)}. \tag{3.3}$$

$$\frac{P_{\text{o}}}{P_1} = \left[1 + \frac{\gamma - 1}{2} M_o^2\right]^{\left(\frac{-\gamma}{\gamma - 1}\right)}. \tag{3.4}$$

In equation 3.4, the value of M_{o} is 1. From the set of equations 3.3 and 3.4, the value of P_a can be extracted and hence the is-entropic post-expansion ratio can be determined. Thus for a range of β_{a1} in [0.6, 1.4], a corresponding range of is-entropic values of M_{a} are calculated. This range of M_{a} is for a single case where [ϕ_{blade}, β_{t1}, σ and [P_0, T_0]] are constant hence are design parameters. This analysis of entropy loss coefficient with respect to the M_{a} and implicitly the β_{a1} will be referred to as the $\boldsymbol{\alpha}$ **case**. According to the hypothesis, the α case yields the value of $\beta_{\text{opt,a1}}$ for one set of design parameters and thermodynamic state at the inlet.

The second step involves the analysis of $\beta_{\text{opt,a1}}$ with respect to [ϕ_{blade}, β_{t1}, σ and [P_0, T_0]]. The cases involved in this step will be referred to as $\boldsymbol{\omega}$ **cases**. ω cases not only involve variation with β_{a1} but also with the other DVs mentioned. For the range of ϕ_{blade}, from literature it is established that metal blade angles for stator blades in supersonic turbines are generally varying in between 65-80° from the horizontal axis [16]. Thus the range of ϕ_{blade} is constrained in the range **[66, 81]** °. The step size is taken as 5 for ϕ_{blade}. The Zweifel relation as shown in 3.5 equation is used to determine the nozzle solidity range. From [1], it is known that

the Zweifel coefficient ranges from 0.8-1.1, with 1.1 being for low-pressure turbines and 0.8 for high-pressure turbines. With the Zweifel value of 0.8, the optimum solidity values for the ϕ_{blade} range lies between 1 and 2. Thus the range of nozzle solidity is determined in between **[1.5, 2]** with a step size of 0.25.

$$\psi_t = \sigma * \left[\frac{\tan(\alpha_2) - \tan(\alpha_1)}{\sec^2(\alpha_2)} \right]. \tag{3.5}$$

For β_{t1}, the range is decided to be between **[6, 8]**. The values of β_{t1} are restrained to two values - 6 and 8. To explore the effect of non-ideality on the trends of the optimal value, the inlet conditions are chosen such that Toluene operates in a relatively wide range of compressibility factor. Also, P_t is kept below 36 bar as above this value, the expansion line can present wet vapor. To enable analytical and effective comparison, three such inlet conditions are chosen. The Inlet Total Pressures are **[30e5, 20e5 and 10e5] bar** and Total Inlet Temperatures are **[580, 550, 540] K**. The inlet densities corresponded to these temperatures and pressure values and are computed using Span and Lemmon EoS [26] from the CoolProp module in Python. The three thermodynamic states studied are represented in the figure 3.3. They vary in terms of the range of compressibility factor and defines the non-ideality of the flow. The range of Z in the first case is [0.87-0.97] and is termed as the ideal Case. The Z range for the second case is [0.74, 0.94] and is termed as the semi-ideal case. The Z ranges in between [0.57, 0.92] in the third case and it is termed as the non-ideal case.

Table 3.1: Summary of design space.

Variable	Range	Step-size	Fixed Parameter	No. of simulations
M_a [-]	1.6-2	0.1	ϕ_{blade}, β_{t1}, σ, $[P_t, T_t]$	41
ϕ_{blade} [°]	66-81	5	β_{t1}, σ, $[P_t, T_t]$	164
β_{t1} [-]	6-8	2	σ, $[P_t, T_t]$	328
σ [-]	1.5-2	0.25	$[P_t, T_t]$	984
P_t [Pa]	[10e5,20e5,32e5]	arbitrary	–	2952
T_t [K]	[540, 550, 580]			
			Total Jobs	**2952**

Table 3.1 shows all pairings of the design variables and the total number of simulations performed. The cases in the first row, fall under the category of α case. The cases in the following rows fall under the category of ω cases. For every variation in an ω case, all α cases are performed. Thus the number of jobs are basically a multiplication of the number of variations in an α case with that in an ω case.

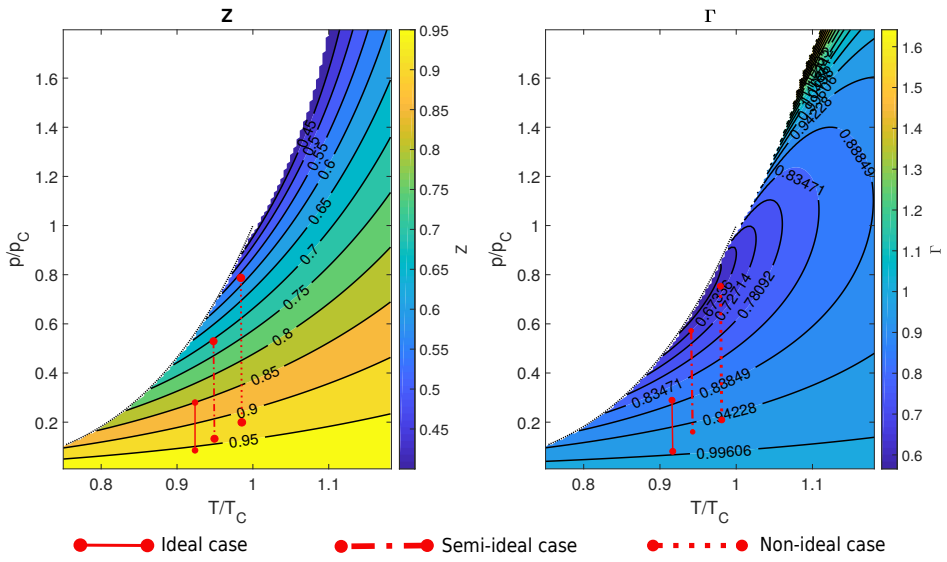

Figure 3.3: Thermodynamic state of inlet and the expansion regime for the three cases.

3.3. DESIGN METHODOLOGY

This section describes the methodology adopted to design an optimum nozzle corresponding to the required Nozzle Exit mach number and make it into a axial blade subject to design constraints.

3.3.1. MOC BASED NOZZLE DESIGN

The design space includes exploration of highly disturbed flow fields. These flow fields are to be analyzed using methods that can obtain solutions to the concerned non-linear PDEs. These PDE's are derived using the Euler form of the Continuity and Momentum equations. In these equations, the density term is substituted by the pressure and sound velocity. The relation of the pressure, density and sound velocity in the total derivative form, and the continuity-momentum equations are then solved together to give the Gas dynamic equations. After application of the irrationality assumption, the gas dynamic equation can be written in the form of the partial differential equation of potential functions. The above method has been described in detail in the thesis work of N. Anand [27]. From the generalized second order partial differential equation, steady supersonic flows are mathematically shown to be hyperbolic in nature. This allows the marching numerical method of Method of Characteristics to be used to compute the flow field [28]. For the flow field computation, the physical and thermodynamic properties of the working medium are computed using Span-Lemmon EoS in CoolProp. The nozzle shape is sensitive to the gas model used to compute fluid properties [27]. It has been shown in the work of [29], that the usage of these multi-parameter EoS, give the most accurate nozzle geometry and thus can be used for industrial applications.

The supersonic stator blade consists of a converging and a diverging section. The diverging section is crucial in design as it accelerates the fluid flow from sonic velocity into the supersonic regime. It is designed using method of characteristics. This method helps to design a nozzle with parallel flow and constant properties at the exit. It is one of the most accurate and robust ways to design a stator nozzle. The nozzle shape, especially the diverging section is heavily influenced by the molecular properties of the working medium. Figure 3.4b shows the regions and the final nozzle shape, obtained from the MOC algorithm. The red and green lines in figure 3.4b represent the positive and negative characteristic lines respectively while the dotted black line represents the nozzle wall.

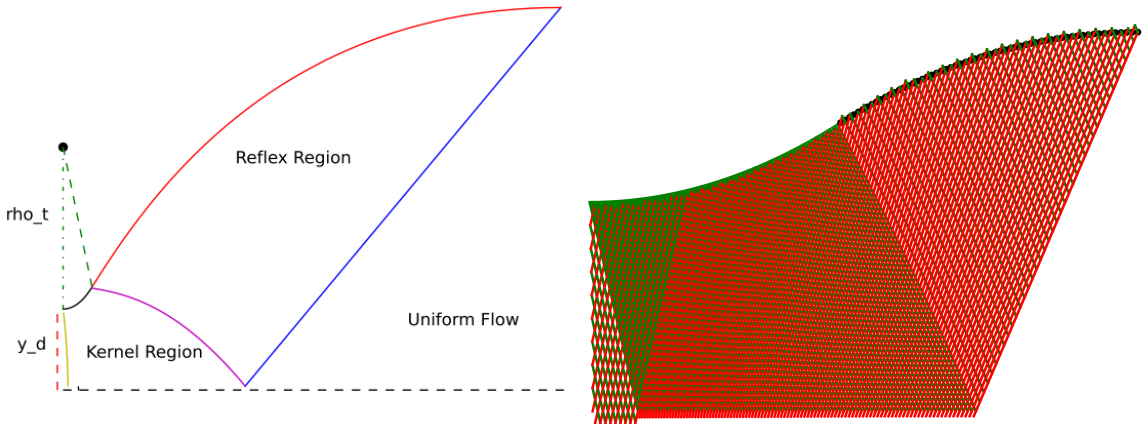

(a) Nozzle parameterization; courtesy [16].

(b) Nozzle design from Method of Characteristics.

Figure 3.4: (a)Nozzle Design parameters for the MoC tool. (b) Obtained characteristic lines and nozzle shape from MoC.

In the Appendix B.1, the nozzle solidity has been derived from the blade geometry. From the equation B.1, it can be concluded that the nozzle solidity is a function of the DoD value of the nozzle. The nozzle parameterization that is shown in figure 3.4a depicts the dependence of the nozzle throat curve on the parameter ρ_t. The variance of this parameter changes the expansion of the working medium between gradual and sudden. This also affects the value of the DoD. The value of DoD also depends on the value of M_a. With increase in M_a, DoD also increases linearly as can be seen in the figure 3.5a. In the design space as previously discussed, the author needs to explore the effect of β_{a1} (hence DoD and M_a) on the value of ζ_{2D} while keeping the nozzle solidity constant. To achieve this, the author generated data for the variation of ρ_t vs Solidity while changing the DoD. The ρ_t values corresponding to the Design solidity were captured for all DoD in the design range. It

was found that ρ_t varies as a non-linear function of DoD for a constant solidity. The author decided to use a second order curve fitted expression to keep intact ease of use and flexibility. This can be seen in the figure 3.5b.

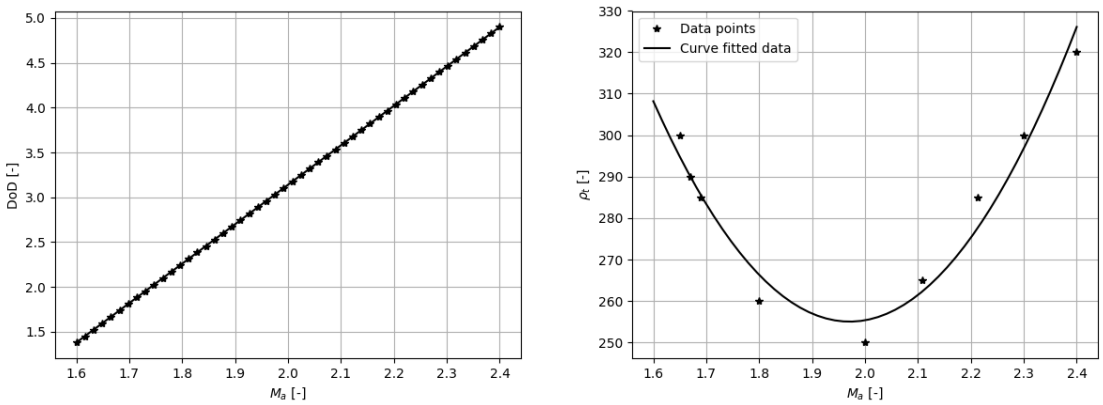

(a) DoD variation with M_a.

(b) ρ_t variation with M_a

Figure 3.5: Nozzle shape Sensitivity to Geometric Parameters of M_a and ρ_t.

3.3.2. AXIAL STATOR BLADE DESIGN

Once the nozzle is designed and validated, the design of the entire axial stator blade is commenced. This procedure is carried out as described in the following six steps and a visualization is provided in the figure 3.6:

- The nozzle with the required DoD ($A_{a,o}$) is obtained from the MoC tool.
- This straight nozzle is then rotated to a specified blade angle ϕ_{blade}.
- The lower section of the nozzle is rotated by pitch angle θ with the origin as shown in figure 3.6. It is moved by the axial pitch distance and placed close to the upper section to form the converging part of the pressure side of the blade.
- This rotated nozzle is scaled by a factor F, so as to position the stator blade outlet on the specified outlet radius.
- The entire converging section of the stator blade is then built with the help of a Non-uniform rational $B\acute{e}zier$-spline.
- The trailing edge is then filleted based on the specified thickness value.

In step 4 of figure 3.6, the rotated nozzle is scaled by a factor F and its ends are placed at Radius R_{out}. While scaling the nozzle it is paramount to keep the ratio of O/A constant for the given ϕ_{blade} and trailing edge thickness. The method to do so is described in detail in the work of Jozef[2]. The convergent section contour needs to smoothly guide the incoming fluid into the throat. It has no other geometric requirement than a gradual reduction in its cross-sectional area. From figure 3.6, the upper and lower sections of the blade are placed in their respective positions in step 4. In step 5, a spline obtained from NURBS, is used to connect the aforementioned nozzle contours thereby closing the entire stator blade. The theory behind NURBS curves will not be discussed here but if needed, [30] will be a recommended reading.

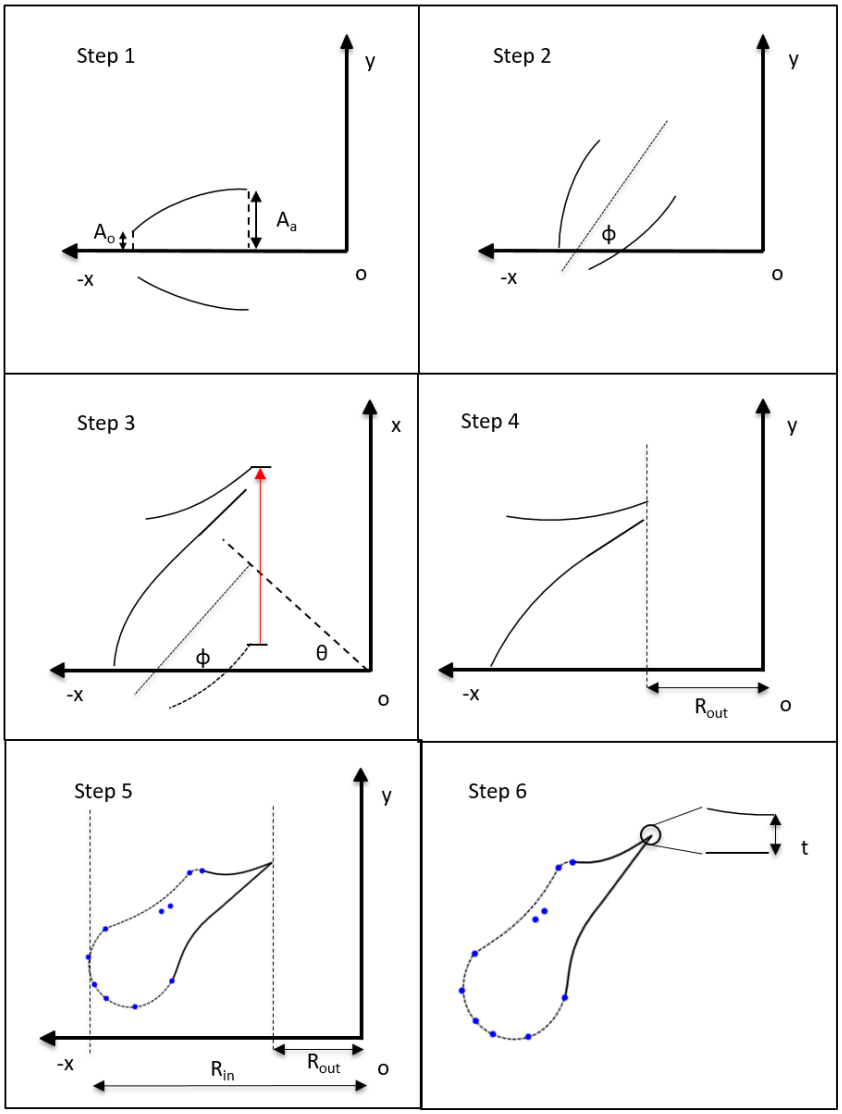

Figure 3.6: Stator blade design procedure in the AST tool.

3.4. COMPUTATIONAL SET-UP

3.4.1. DISCRETIZATION OF COMPUTATIONAL DOMAIN

A flow domain is created around the blade geometry. The meshing for the flow domain is carried out using the in-house open source software Unstructured Mesh Grid 2 (UMG2). The mesh boundaries are illustrated in figure 3.7 while the elements and the refined regions are illustrated in figure 3.8. The elements of the mesh are both triangular and quadrilaterals.

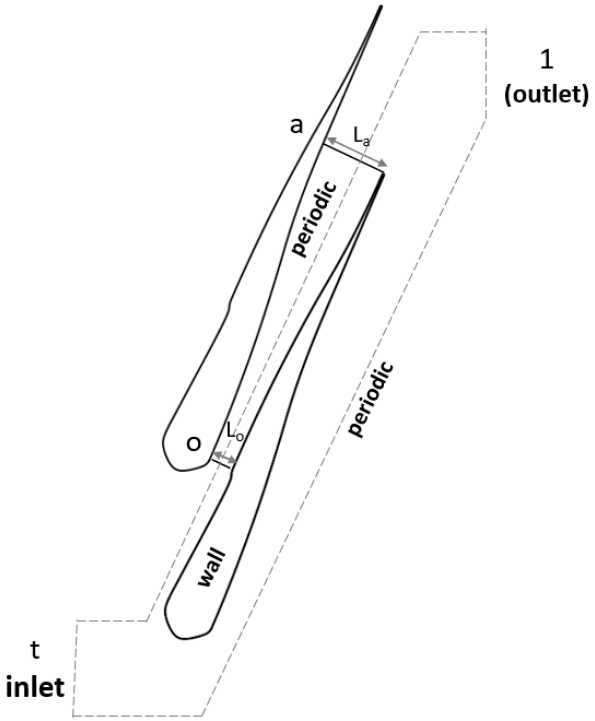

Figure 3.7: Schematic diagram of flow domain with specified boundary condition.

The inlet region up-to the throat (region 0-o) is in the subsonic regime. Thus the region has a comparatively larger element size. This is done to optimize processing power as in such regions the relevant flow phenomena is captured even with a coarser grid. Throughout the domain the elements are triangular while at the boundary layer they are rectangular in shape so as to resemble the boundary layer structure. The boundary layer elements are clustered and enlarged perpendicular to the blade boundary using a growth function [2]. This is done to increase the accuracy of the results and take into account the effects of viscosity. The trailing edge region is crucial in determining flow behavior and the mesh element density should be high so as to resolve flow phenomena in that region sufficiently. Thus the elements within the region enclosed by radius times the trailing edge thickness is refined. The elements in the post expansion region also have smaller dimensions but are not as refined as the boundary layer or the trailing edge region to maintain processing power.
The generation of mesh for all the geometries were automated using a python code and required mesh density and trailing edge refinements were maintained.

(a) Hybrid mesh of entire flow domain.

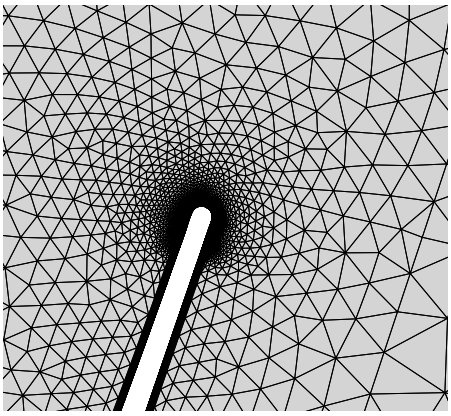

(b) Trailing edge meshing.

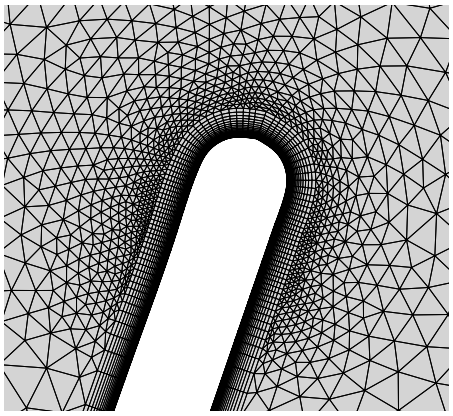

(c) Structured meshing for boundary layer at trailing edge.

Figure 3.8: Discretization of the computational domain.

3.4.2. NUMERICAL SOLVERS

The solver used to perform flow simulations is an open source software suite - SU2 [31]. The solutions are obtained by solving the compressible form of the Navier Stokes governing equations. This was because the compressibility effects become prominent when the Mach number in the regime exceeds 0.3. This is the case in ORC turbines which operate in the highly supersonic regime. The compressible Navier stokes equation is given as:

$$\frac{\partial}{\partial t}\mathbf{U}(\mathbf{x},t) + \nabla \cdot [\mathbf{F}_{\varepsilon}(\mathbf{U}(\mathbf{x},t)) - \mathbf{F}_{v}(\mathbf{U}(\mathbf{x},t))] = \mathbf{Q}(\mathbf{U}(\mathbf{x},t)). \tag{3.6}$$

In the equation 3.6, U represents the conserved variable in the vector form (ρ: Density, ρv: Momentum and ρE_t: Total Energy), Q is the source term, F_v is the diffusion term and F_c is the convective flux term. To solve this convection-diffusion equation, the conserved variable should be continuous in the entire domain. Due to the supersonic nature of the flow, discontinuities are bound to arise. Thus an integral form of the governing equation is taken into consideration. The volume integrals bounding the convective terms are converted into a surface integral using Gauss Divergence Theorem. These surface integrals are then approximated as summation of surface across each face of the control volume. Finally the modified convective-diffusion equation is discretized explicitly in time domain for numerical simulations.

In this study, the non ideal effects of a compressible fluids could play a significant role hence the question that arises is whether the SU2 suite is capable of handling NICFD effects. It has been demonstrated and established with certain cases that SU2 is well suited to be used to analyze flow solutions in these operating conditions [32]. The simulations require the thermodynamic and physical properties of the working medium. These properties are obtained using the Peng-Robinson's equation of state (modified form of SWK CEoS) [33]. A constant viscosity and constant Prandtl conductivity model is used for calculating transport properties of the fluid. A one equation Spalart-Allmaras (SA) turbulent model is used to close the turbulence equations. This eddy-viscosity model has been chosen as it is robust and computationally very efficient as it uses only a single transport equation [34]. Also compared to the other turbulent models (SST), the obtained convergence was of a higher order. The numerical scheme used for calculation of the convective fluxes is the Roe's approximate Riemann solver. For integration of the time discretization, an Euler implicit scheme is used while for spatial integration, a second order scheme has been used.

In the computational set-up, input parameters are specified for the CFD solver to initialize. These parameters are given at the boundaries of the computational domain. An axial stator stage comprises of stator blades arranged axially, which allows the author to simulate a single stator blade and extend it to the entire stage. From the computational domain shown in figure 3.8, it can be seen that it consists of four boundaries namely: Inlet, Outlet and two surfaces arranged laterally. The two lateral surfaces are duplicated at a linear distance equal to the axial pitch of the stator stage. They are periodic in nature. Total Pressure, Total Temperature and free stream density of the working medium are imposed at the inlet boundary while the static pressure is imposed at the outlet boundary to attain the design expansion ratio across the stator blade. Also, Reflecting boundary conditions have been imposed on the inlet and outlet boundaries as with NRBCs, sufficient order of convergence was not being attained. These are the important configuration settings required for the computational setup. The rest of them are described in detail in the appendix C.

3.5. VERIFICATION

This section describes the method of verification adopted to ensure the input specifications are met from respective tools used in the ADCT. From the sections 3.2 and 3.3, it has been established that a nozzle shape is defined by the MoC Tool with the nozzle outlet mach number as an input variable. Once the nozzle is designed, the entire stator blade is constructed with the trailing edge thickness and axial pitch as an input. Post meshing, the total inlet conditions and the static value of the back pressure are used to carry out the CFD simulation. The nozzle outlet Mach number and static pressure from the MoC tool have to match or be within an acceptable range of that obtained from the CFD tool to ensure that the nozzle expansion taking place is as expected, and the results from the CFD simulation can be analyzed to draw conclusions. The following subsections describe the procedure to validate the tools in the design chain in figure 3.2.

3.5.1. MOC TOOL VERIFICATION

The MoC tool designs a nozzle shape based on the degree of expansion, subject to minimal losses. The degree of expansion is given by the area ratio of the nozzle exit width to the throat width. The first validation performed hence is between the input value of M_a and the output value obtained from the output file (*.out) of MoC. The figure 3.9a showcases the error plot between the Design and Obtained value of M_a for the entire range of M_a. The error is observed to be less than 0.5%.

The value of P_a obtained from the MoC output file is compared to that of the isentropic pressure values, and its plot is shown in figure 3.9b. It is observed that the isentropic and real gas values of P_a do not correspond. P_a obtained for a real gas is less than that for an isentropic gas. This is because the value of P_a computed for ideal gas is by using the isentropic equation while that from MoC uses the Peng-Robinson's equation of state.

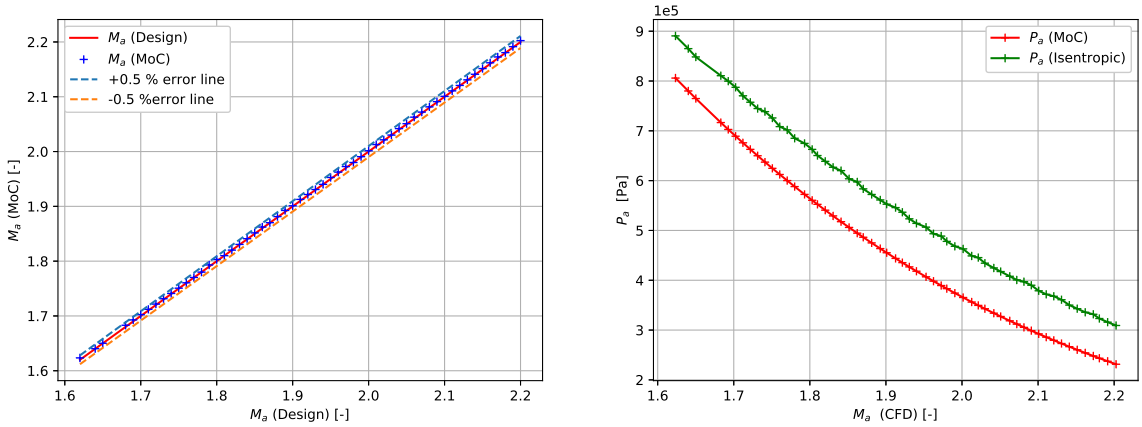

(a) **(b)**

Figure 3.9: (a) Error Plot between design M_a and value obtained from MoC tool. (b) Difference between design P_a and its isentropic value for the same M_a.

3.5.2. AST VERIFICATION

In the design chain, the next validation carried out is for the axial stator blade. To control the variables affecting the losses for analysis with the PDVs and SDV, there are certain constraints imposed. The values of nozzle solidity and ratio of trailing edge thickness to blade pitch with variation of M_a are monitored as they directly affect the blade boundary layer and trailing edge losses. As seen in figure 3.2, ϕ_{blade} is an input variable to the AST tool, thus once verified, does not need to be continuously monitored. The same applies for inlet conditions. The figure 3.10a shows the comparison between the nozzle solidity calculated from the obtained blade and the design solidity. Again, the margin of error lies within 5% for the entire range of M_a (shown on the right y-axis in the same figure). From the figure 3.10b, it can be seen that the ratio of trailing edge thickness to axial pitch is constant and hence has no effect on the trends of losses with variation in M_a.

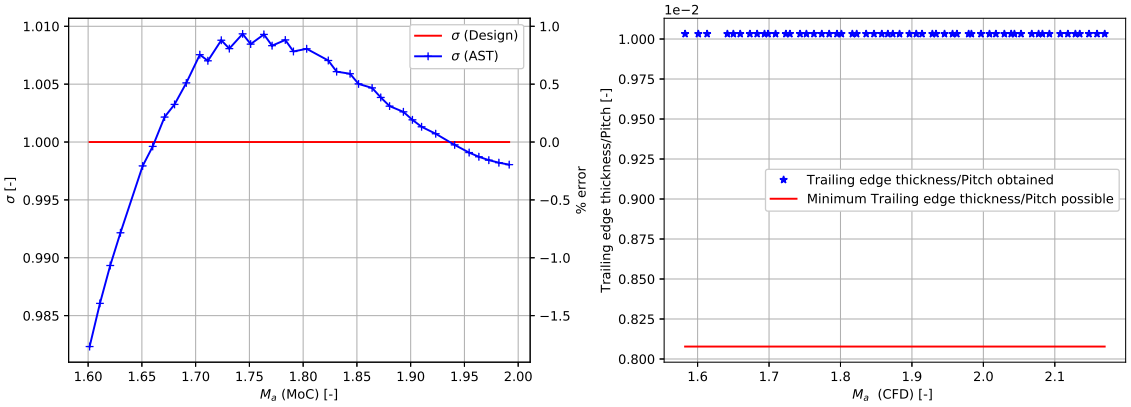

(a) **(b)**

Figure 3.10: Validation plot for constraints imposed on σ and L_{TE}/axial pitch (a)Error plot between design and obtained nozzle solidity for design range of M_a. (b)Trailing edge thickness to axial pitch consistency for design range of M_a.

3.5.3. MESH QUALITY CHECK

The mesh quality was checked by an inbuilt evaluation tool which tabulated the quality of the mesh as shown in figure 3.11a. In figure 3.12, the y_+ values are plotted along the surface of the stator blade geometry and confirmed to be close to the value of one, at points where large gradients in the solution are expected to arise [35]. A low value of y_+ means that viscosity is the dominant factor on shear stress. The value of y_+ is defined by the following equation:

$$y_+ = \frac{y u_T}{\mu} \tag{3.7}$$

where y is the absolute distance from the wall, u_T is the friction velocity and μ is the kinematic viscosity. Thus if the value of y is reduced such that the viscous sub-layer is captured well, the mesh is said to capture the boundary layer phenomena well. The value of y is taken as 1e-6 for this case.

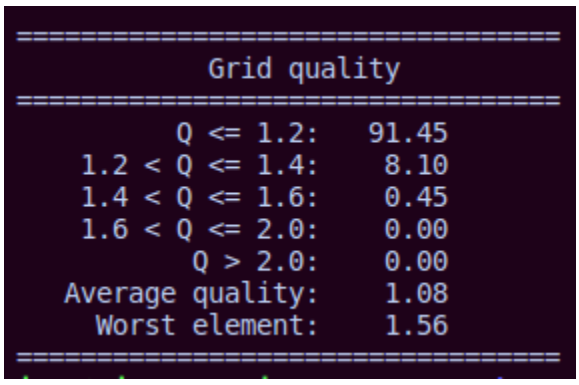

(a) Mesh quality evaluation parameters from UMG2d tool.

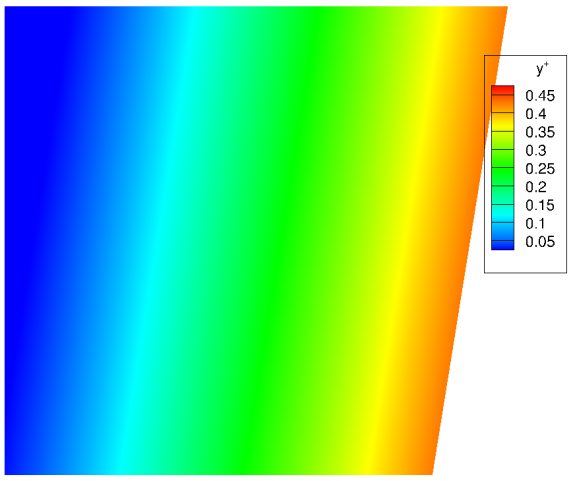

(b) y_+ value obtained close to nozzle throat wall.

Figure 3.11: Validation of mesh using grid quality parameters and y_+.

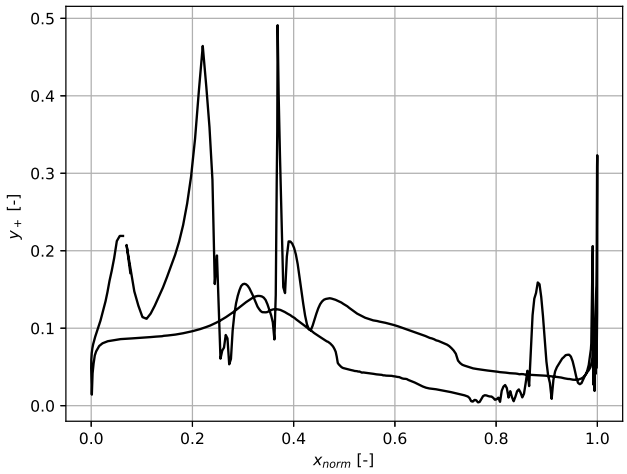

Figure 3.12: y_+ value obtained along the stator blade profile represented by x_{norm}.

3.5.4. CFD TOOL VERIFICATION

The CFD tool had inputs such as the inlet conditions, outlet conditions, periodic mesh along with the numerical solvers used to model the fluid flow. The validation of this tool was the most crucial as the author had to check if the nozzle was performing as simulated by the MoC tool. For the validation of the nozzle, the values of M_{a} and P_{a} obtained from the CFD results were checked against those obtained from MoC. From figure 3.13a and 3.13b, it can be seen that the value of M_{a} obtained from MoC is within 2% of the design mach number. Also the value of P_{a} obtained from the CFD results lie within 5% of that obtained from MoC. This validates the nozzle performance.

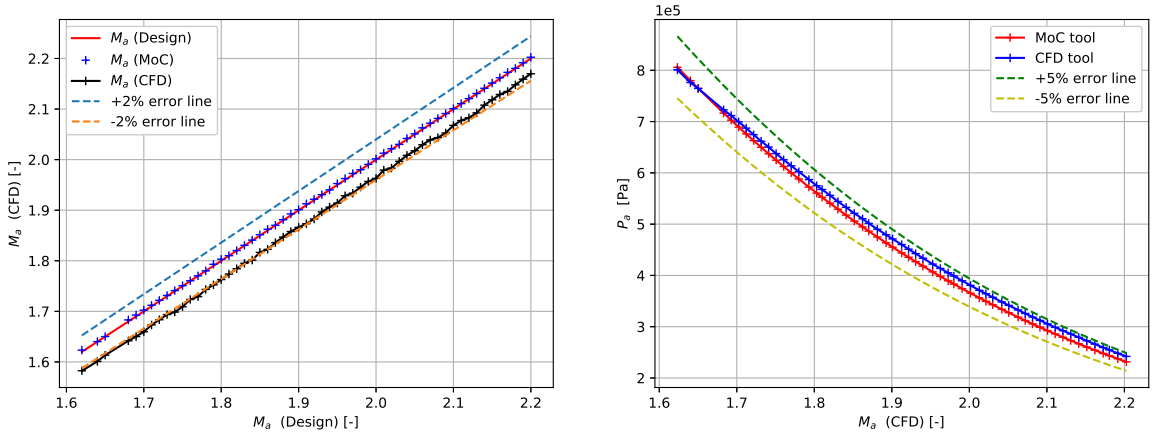

(a) **(b)**

Figure 3.13: (a) Error between design value of M_{a} from MoC and CFD tool vs M_{a}. (b) Error between value of P_{a} obtained from MoC and CFD tool vs M_{a}.

The static pressure at the outlet achieved had to be validated with the input value of the outlet pressure. Correspondingly, the validation had to be carried out for the value of β_{t1} obtained from CFD results as it had to be checked against the design value. In figure 3.14a, the red plot denotes the design back pressure while the blue plot denotes the value of back pressure obtained. From the right y-axis, it can be seen that the error margin lies below 5%. From figure 3.14b, the same can be observed. The design and obtained β_{t1} values lie within 5% of each other. Thus the outlet conditions of the computation is validated.

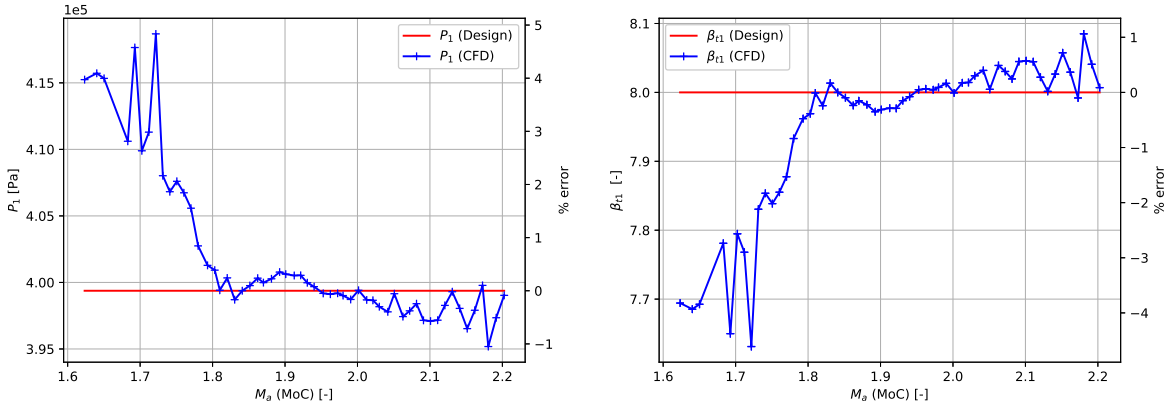

(a) **(b)**

Figure 3.14: (a) Error between design value of P_1 and value obtained from CFD tool. (b) Error between design value of β_{t1} and value obtained from CFD tool.

Further, it had to be confirmed if the value of the outlet axial mach number was less than one. Cases with axial M_1 greater than one tend to have numerical inaccuracies as the the properties are calculated axially in the computational grid at the speed of sound while the actual fluid flow is supersonic. From figure 3.15a, it can be seen that the values of the axial M_1 lie below one for the entire design space. The last validation check was for the convergence of the entire computation. The minimum convergence limit for a simulation was kept to four orders of magnitude of the total energy variable. The figure 3.15b represents the orders of magnitude of convergence achieved for the computations performed.

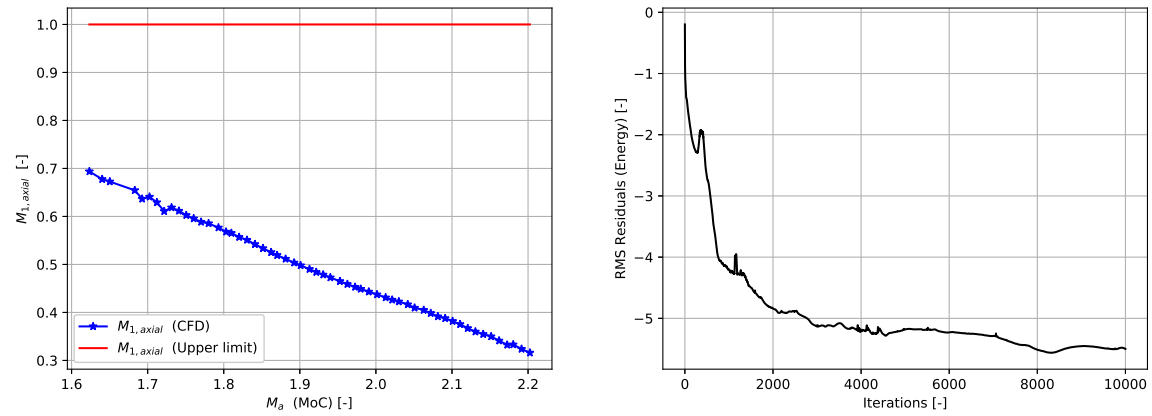

(a) **(b)**

Figure 3.15: (a) Stator outlet axial mach number vs M_a. (b) History of convergence of RMS values of energy residuals with number of iterations.

The flow angle obtained at station 1 and corresponding flow deviation angle ψ obtained, was plotted with varying M_a for ϕ_{blade}= 66 and 81° respectively in figure 3.16. The discrete points represent the actual values and the line represents their interpolation. It is observed that with higher ϕ_{blade}, the range of ψ decreases for the same range of M_a. Additionally, the flow deviation angle behavior from the CFD tool with respect to the Post-expansion ratio was validated with respect to the analytical equation 3.8 adapted from [1].

$$\tan\psi = \frac{\frac{\gamma}{\gamma-1}\frac{P_1}{P_a}\tan\phi_{blade} - \left[\left(1-\frac{P_1}{P_a}\right)\left(2\frac{\gamma}{\gamma-1}M_a^2 - 1 - \frac{\gamma+1}{\gamma-1}\frac{P_1}{P_a}\right) + \left(\frac{\gamma}{\gamma-1}\frac{P_1}{P_a}\tan\phi_{blade}\right)^2\right]^{1/2}}{1+\gamma M_a^2 - \frac{P_1}{P_a}} \tag{3.8}$$

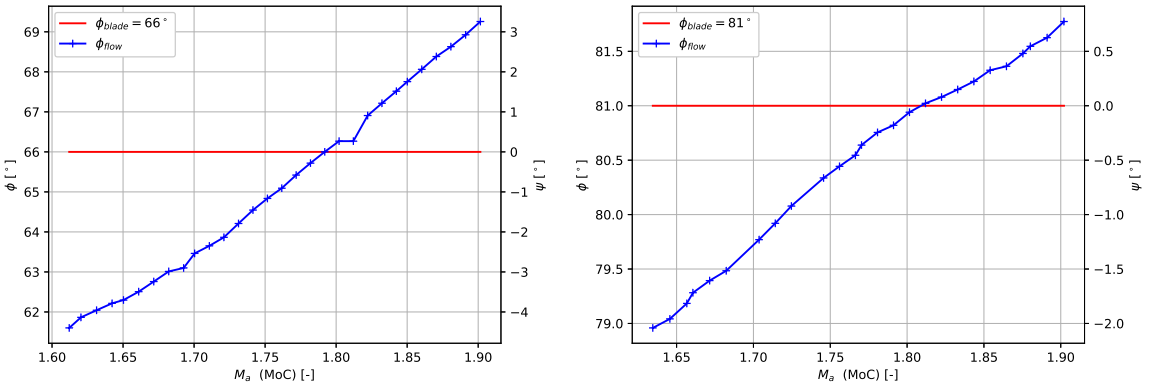

(a) $\phi_{\text{blade}} = 66°$. **(b)** $\phi_{\text{blade}} = 81°$.

Figure 3.16: Comparison of outlet flow angle variation and flow deviation with M_a for two ϕ_{blade}.

In this equation, the ratio of P_1 to P_a is the reciprocal of the post expansion ratio (β_{a1}). When this value is one, the flow deviation angle becomes zero. When this value is greater than one, the flow deviation angle from the equation becomes negative and when the value of the post-expansion ratio becomes less than one, the flow deviation angle becomes positive. As explained previously in the section 3.2, the value of post-expansion ratio directly relates with the nozzle exit mach number and can be controlled by the geometric parameter of degree of divergence. In the figure 3.16a, the stator outlet flow angle and the gauge angle (metal blade angle) has been plotted with respect to M_a. It can be seen here that with increase in M_a (decrease in β_{a1}), the flow deviation angle increases and at the value of M_a corresponding to that of β_{a1} equal to 1, the value of flow deviation angle is found to be zero. Another observation that can be made is that the flow deviation angle for higher gauge angle decreases as is also stated in [1]. The deviation angle obtained from the analytical correlation in equation 3.8 was plotted for the same range of M_a for both stator blade angles. From the figure 3.17, it is observed that the values for ψ corresponding to both values of ϕ_{blade} obtained from the analytical correlations match those obtained from numerical simulations.

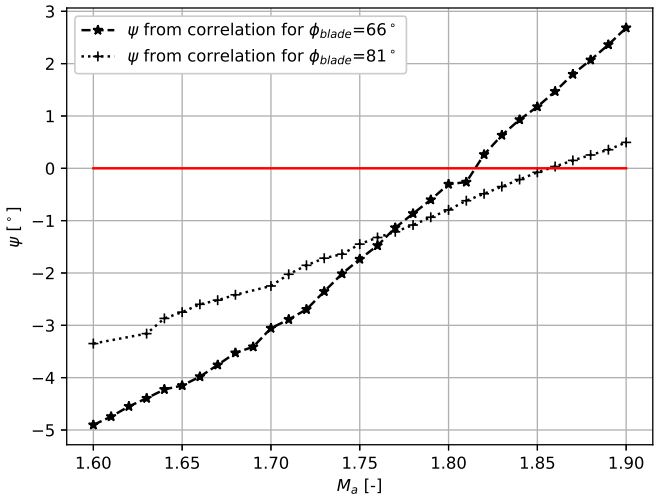

Figure 3.17: Plot of ψ obtained from analytical correlation (3.8) vs M_a for ϕ_{blade}=66 and 81°. The star and plus markers represent discrete points for which ψ is obtained while the line represents the interpolated curve.

3.5.5. VERIFICATION OF FLOW VARIABLE AVERAGING PROCEDURE

The computational domain consists of a single stator blade. This means the the nozzle and stator exit boundary is split on both ends of the blade. This makes extracting the nozzle and stator exit data points more complex, thus making the mass-flow averaging of the required variables more involved. A Python script was written to extract these domain points and carry out the mass-flow averaging. To validate the values from the Python script, the domain points were extracted from Tec360 using the macro suite available and carrying out the line integration procedure manually. The calculations were done for the flow variables of nozzle exit pressure and nozzle exit entropy for three different blade configurations obtained by varying the Degree of divergence, but under the same operating conditions (Total Inlet Conditions and Expansion Ratio). The validation results have been presented in the table 3.2.

Table 3.2: Comparison of Line integration values of mass averaged flow variables obtained from Python script and commercial package Tec360.

DoD	$\mathbf{P}_a$ $[Pa]$			$\mathbf{s_a}$ $[kJ\ kg^{-1}\ K^{-1}]$		
	Script	Tec360	%error	Script	Tec360	%error
1.38	8.279e5	8.425e5	1.73	9987.14	9995.65	0.08
1.81	5.630e5	5.789e5	2.74	10005.22	10004.80	~0
2.5	3.653e5	3.807e5	4.04	10012.09	10014.73	~0

3.6. POST-PROCESSING

The completion of the validation step allows the author to move forward with the Post-processing of the simulation data. Considering the large amount of simulations and the massive cache of data, an automated algorithm is built to analyze it. Post-processing of the data is carried out in the following steps:

- The entropy generation coefficient is extracted from the flow field and plotted with varying post-expansion ratio, while keeping the secondary design parameters constant. For calculation of the value of β_{a1}, the static pressure values at the nozzle exit are extracted and a mass-flow averaging operation is carried out. The **mass-flow averaged value** of P_a is used to calculate the value of β_{a1}. The mass-flow averaging operation is described in the equation 3.9 where i corresponds to each cell at the nozzle exit.

$$P_{a,\,avg} = \frac{\sum_{i=0}^{n} P_i \times (\rho_i v_i dy)}{\sum_{i=0}^{n} \rho_i v_i dy} \tag{3.9}$$

  Due to the sheer types of nozzles, the location of the nozzle exit is not fixed. For every nozzle the location of the nozzle exit has to be determined. This is done by finding the line perpendicular from the trailing edge of the lower blade to the upper blade. This line represents the nozzle exit. With the help of tecplot, the values of P_a are extracted and the mass flow averaged value of P_a are calculated. This can be also seen in figure 3.18.

- The flow deviation at the stator outlet is also an interesting variable that is investigated. This variable is computed by finding the difference between the Blade metal angle and the mass-averaged value of the stator outlet flow angle at each discretized element. The value of the flow angle is found by taking the inverse tangent of the ratio of the y-momentum to the x-momentum at each element.

- To visualize the flow phenomena, the contour plots of the local mach number and static pressure are plotted. This helps the author to study the flow phenomena in the fluid domain.

- The relevant flow variables such as M_a, P_a, δs, β_{a1}, DoD and flow deviation are assimilated in a data file for recurrent use.

- All the above steps are performed for varying secondary design parameters throughout the design space.

- For certain analysis presented in the following chapters, thermodynamic variables have to be extracted from a streamline in the flow domain. The selection of a streamline is of importance as it has to be free from wall effects. Thus the mean streamline of the nozzle is selected. For all nozzles at different metal blade angles, automating this procedure was important. Thus the streamline distance was calculated with the following formula:

$$\text{streamline distance} = 0.5 \times \text{Axial Pitch} \times \cos(\phi_{\text{blade}}) \tag{3.10}$$

  The figure 3.18 showcases the streamline from which the thermodynamic values are extracted. Streamline distance is the length of the line drawn perpendicular from the nozzle trailing edge to the mean streamline.

Figure 3.18: Extraction of variables of interest from mean-streamline.

An object orient programming approach was adopted so as to maintain modularity and ease of modification of algorithms. This allowed the author to use functions for the different cases repeatedly, thereby reducing redundancy.

4

RESULTS AND DISCUSSIONS

This chapter showcases results obtained from the study performed on trends of $\beta_{\text{opt,a1}}$ and ψ with respect to the design variables. The following points describe the layout of this chapter.

I. 4.1 presents evaluation of hypothesis proposed in section 2.3. It describes the method of evaluation and lists the conclusions drawn from it.

II. 4.2 shows geometric sensitivity of the stator blade with each of the design variables and subsequently, discusses the trends of the optimum value of post-expansion ratio with respect to design variables as following:

   i. β_{a1} trend with respect to ϕ_{blade}.

   ii. β_{a1} trend with respect to β_{t1}.

   iii. β_{a1} trend with respect to σ.

   iv. β_{a1} trend with respect to non-ideality $[P_{\text{t}},\ T_{\text{t}}]$.

III. 4.3 presents trend of ψ with respect to ϕ_{blade} and non-ideality.

IV. 4.4 elaborates the surrogate modeling performed for the obtained optimum points and presents a design correlation for $M_{\text{a, opt}}$ and ψ. A demonstration with assumed input values for the ideal case is then presented in section 4.5.

V. 4.6 compares the kinetic energy loss and entropy generation coefficients from the proposed design and that from empirical correlations. It also re-assesses the hypothesis for an interpolated optimum design vane for β_{t1}=7, ϕ_{blade}=73° and σ=2.

4.1. HYPOTHESIS VERIFICATION

The proposed hypothesis was evaluated to understand the sensitivity of the loss mechanisms to the post-expansion ratio. To do so, stator geometries with increasing DoD were analyzed for a constant ϕ_{blade}, σ, β_{t1} and inlet conditions. The geometric sensitivity with increasing DoD is shown in figure 4.1. From left to right in the figure, value of L_o (refer to figure 3.7) decreases while the axial pitch length remains constant. This leads to an increase in DoD.

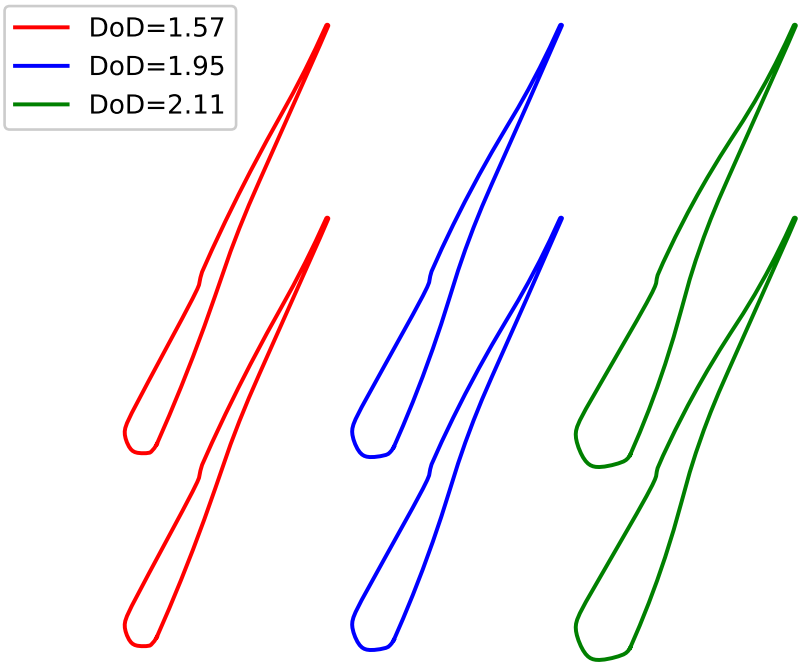

Figure 4.1: Geometric sensitivity of stator blade to DoD (M_a). From left to right, L_o decreases, thereby increasing DoD and consequently M_a.

An increasing value of DoD corresponds to higher M_a which means a lower β_{a1}. By varying DoD, the value of β_{a1} was varied between 0.7-1.4, corresponding to which flow across these stator vanes were analyzed using a CFD model. The entropy generation (Δs) obtained from each of the stator geometry was plotted for the range of β_{a1}. The obtained plot confirmed one aspect of the hypothesis ie. there exists an optimum value of β_{a1} for which the 2D losses are minimum. The loss breakdown was done henceforth to see the behavior of the nozzle and post-expansion (PE) losses.

Figure 4.2 shows variation of the change in 2D, nozzle and PE loss as a function of β_{a1}. The diamond marker on the 2D loss curve represents the optimum value of β_{a1} for the total loss and hence the recommended design value. The diamond marker on the PE region loss curve represents the optimum value of β_{a1} for minimum PE losses. From figure 4.2, the following observations can be made:

i. Δs in the flow domain and the PE region varies as a second order polynomial with respect to β_{a1}.

ii. Δs in the nozzle region linearly decreases with increase in β_{a1}.

iii. Optimum β_{a1} value is found to be greater than one.

iv. Δs in the PE region is greater than that in the nozzle region.

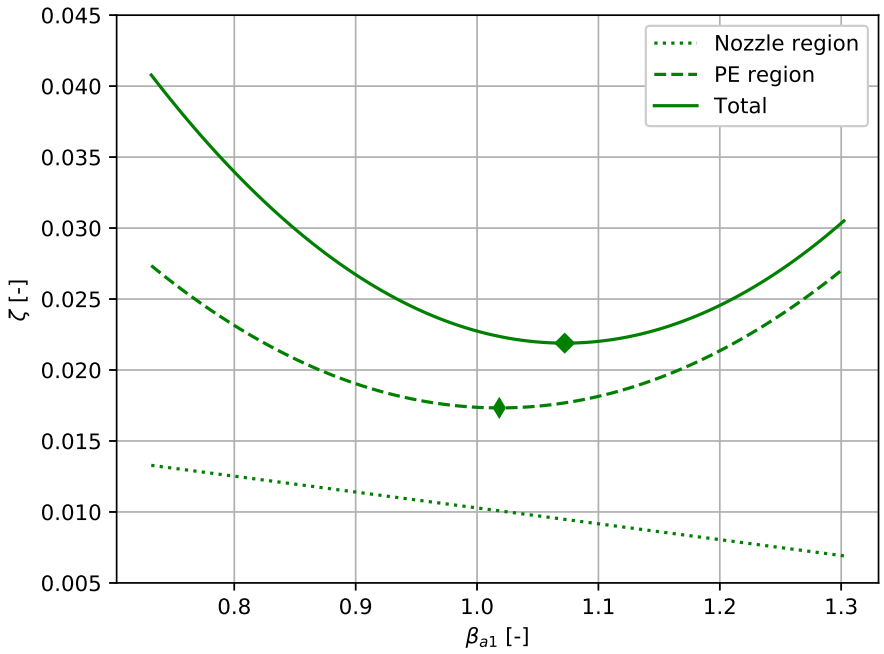

Figure 4.2: Δs trend for total, nozzle and PE regions with respect to β_{a1}. The lines are fitted curves of actual data points. Diamond markers represent optimum values of β_{a1} for total and post-expansion region.

To explain the aforementioned observations, the Mach and Pressure contours of the flow domain were plotted and analyzed.

From the figure 4.3, it can be seen that for β_{a1} lower than 1, a strong shock wave on the pressure side and an expansion fan on the suction side are formed. This shock wave interacts with the suction side of the adjacent blade leading to the formation of a separation bubble. The flow exiting the stator blade is deviated towards the suction side of the adjacent blade. Higher flow deviation signifies higher mixing losses.

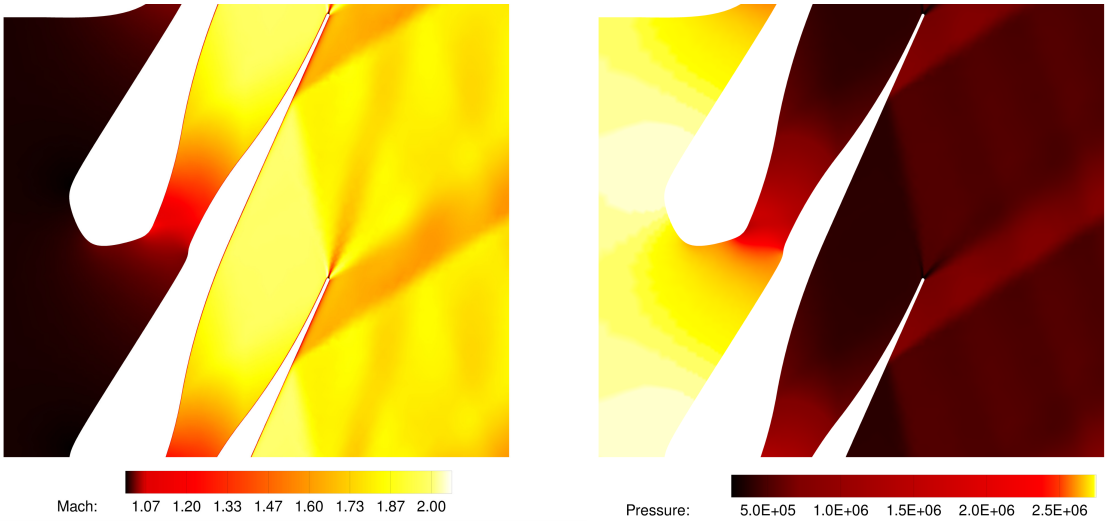

(a) Mach number along the stator chord.

(b) Pressure along the stator chord.

Figure 4.3: Flow contours for compression in the PE region where β_{a1}=0.87 (post-compression case).

In figure 4.4, the observed phenomenon as above reverses. Here β_{a1} is greater than one, which means the flow exiting the nozzle is undergoing expansion. An expansion fan is formed on the pressure side. However, a shock wave is formed on the suction side since the static pressure here is lower than P_1. The flow exiting the stator blade deviates away towards the pressure side of the adjacent blade which also suggests higher mixing losses.

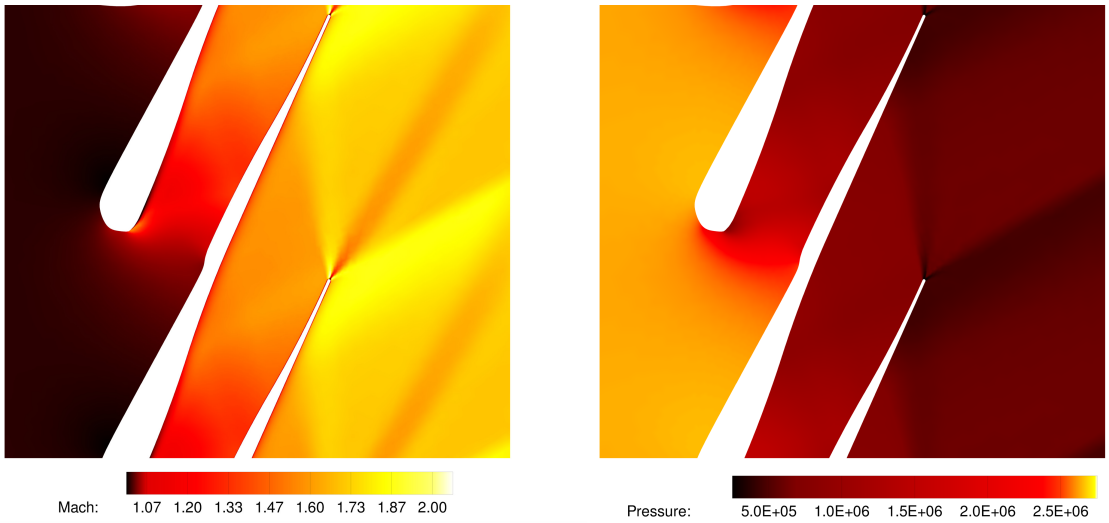

(a) Mach number along the stator chord. **(b)** Pressure along the stator chord.

Figure 4.4: Flow contours for expansion in the PE region where β_{a1}=1.39 (post-expansion case).

In figure 4.5 where β_{a1} is close to one, the flow is characterized by two weak trailing edge shocks.

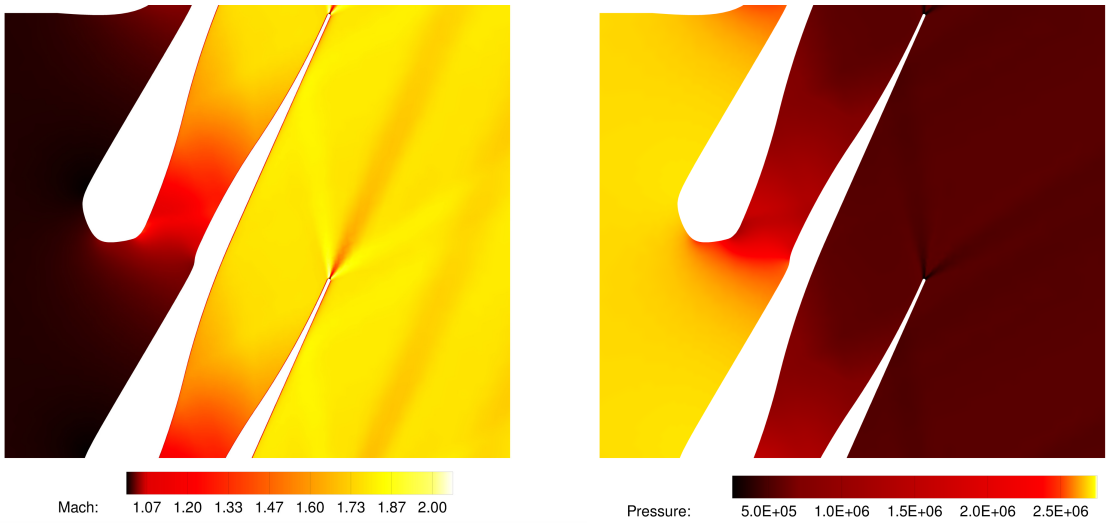

(a) Mach number along the stator chord. **(b)** Pressure along the stator chord.

Figure 4.5: Flow contours for expansion in the PE region where optimum β_{a1}=1.05 (optimum case).

The formation of strong shock waves and expansion fans contribute towards loss in the post-expansion region. When two trailing edge shocks waves are formed and the flow deflection is minimal, the optimum point is found. This is the reason for the variation of Δs with respect to β_{a1} as a second order polynomial as stated in observation (i).

Observation (ii) is that the Δs in the nozzle decreases with β_{a1} which means it increases with DoD. This is because with increase in DoD, the value of L_o decreases. The boundary layer thickness as a percentage of the mean thickness increases which relates to the increase in boundary layer loss. Nozzle loss occurs due to viscous dissipation due to the formation of the boundary layer, hence the increase in the nozzle loss.

Observation (iv) states that Δs in the PE region is greater than that in the nozzle region. This is because the loss mechanisms contributing to the total loss are all in the highly supersonic region. The loss mechanisms in the PE region are mixing, TE loss, shock loss and the viscous dissipation due to the PE region of the stator blade. Also, the shock wave boundary layer interaction is a source of loss.

Figure 4.6 shows the absolute entropy values in the flow domain along with the trailing edge. In figure 4.6a, the two encircled regions are the TE region and the shock wave boundary layer interaction region. These are two contributors to the loss in the post-expansion region. The magnitudes of entropy generation in the nozzle is lower than at these two regions. These two regions have a higher value of entropy due to re-circulation zones being formed. These re-circulation zones are turbulent eddies which lead to loss of kinetic energy. A re-circulation region converts the kinetic energy of the flow to internal energy. This rise in internal energy is identified by the increase in local temperature.

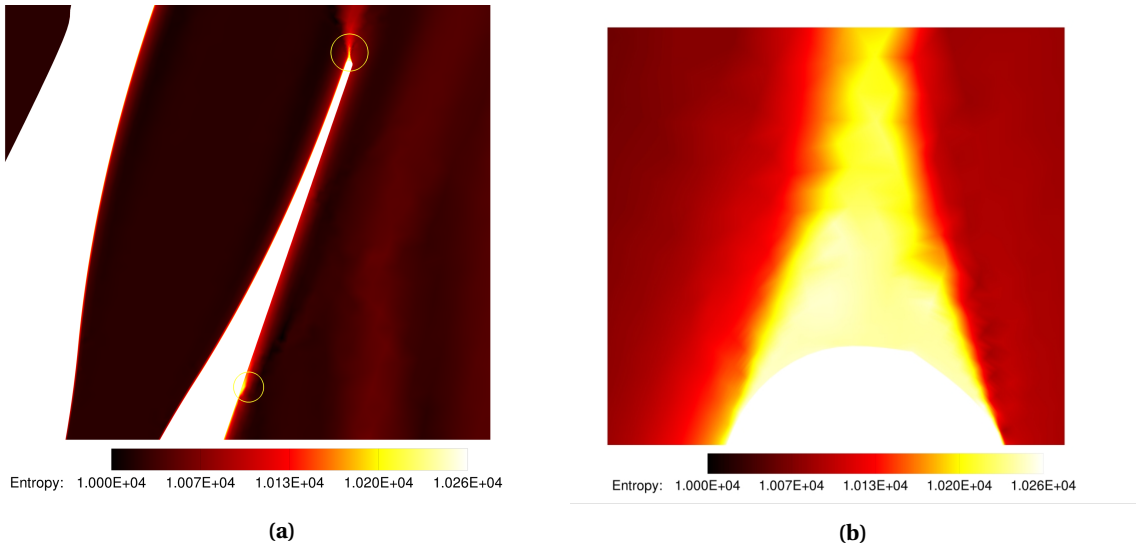

(a) **(b)**

Figure 4.6: Entropy rise due to re-circulation regions formed in PE region (a) Encircled separation bubble and TE region (b) Magnified contour of TE region.

4.2. DISCUSSION OF $\beta_{OPT,A1}$ TRENDS

The hypothesis in section 2.3 establishes that for a converging-diverging nozzle, there exists a value of the β_{a1} which corresponds to best performance ($\beta_{opt,\,a1}$). Variation of this $\beta_{opt,\,a1}$ with respect to design variables is discussed in this section. Its variation with metal blade angle (ϕ_{blade}) is discussed first. This is followed by its variation with the total-static expansion ratio (β_{t1}). Subsequently, its variation with nozzle solidity and non-ideality follows. The flow deviation angle corresponding to optimum design and its trend is also explored with ϕ_{blade} and inlet conditions. The first results will be shown for the ideal case followed by a comparison with the non-ideal case.

4.2.1. $\beta_{OPT,\,A1}$ VARIATION WITH ϕ_{BLADE}

In order to study the variation of $\beta_{opt,a1}$ with ϕ_{blade}, design vanes with constant σ, M_a and total inlet conditions were selected. Their variation with varying ϕ_{blade} is illustrated in in figure 4.7.

- The length of the straight section of the supersonic region of the blade, increases as seen in fig 4.7.
- L_o and L_a (refer to figure 3.7) decreases while axial pitch remains constant.

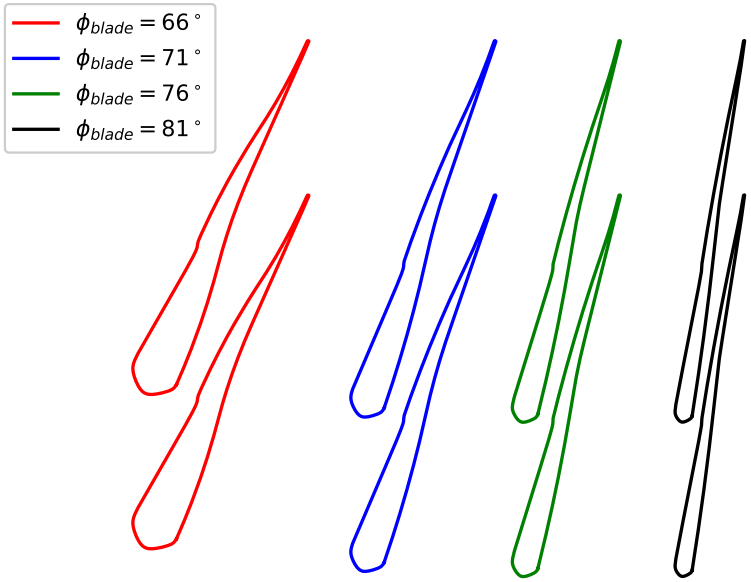

Figure 4.7: Variation of vane geometry with ϕ_{blade}. From left to right, ϕ_{blade} increases while the blade thickness decreases. L_o and L_a decrease proportionately thereby maintaining a constant DoD.

These variations affect the trend of β_{a1} which is illustrated in figure 4.8. It shows the variation of ζ_{2D} with respect to β_{a1} for four ϕ_{blade} values. The trend lines are a curve fit of the original data points. The diamond marker on each trend line denotes the optimum value of β_{a1} corresponding to the metal blade angle. A twin x-axis with M_a has been plotted in the same figure. From the figure 4.8, two major observations can be made:

i. The entropy generation loss coefficient increases with increase in ϕ_{blade}.

ii. The value of $\beta_{opt,\,a1}$ increases with increase in ϕ_{blade}.

Observation (i) is due to the increasing length of the straight section of the supersonic part of the blade due to which viscous losses increase in magnitude. Also, with decreasing throat width, the boundary layer

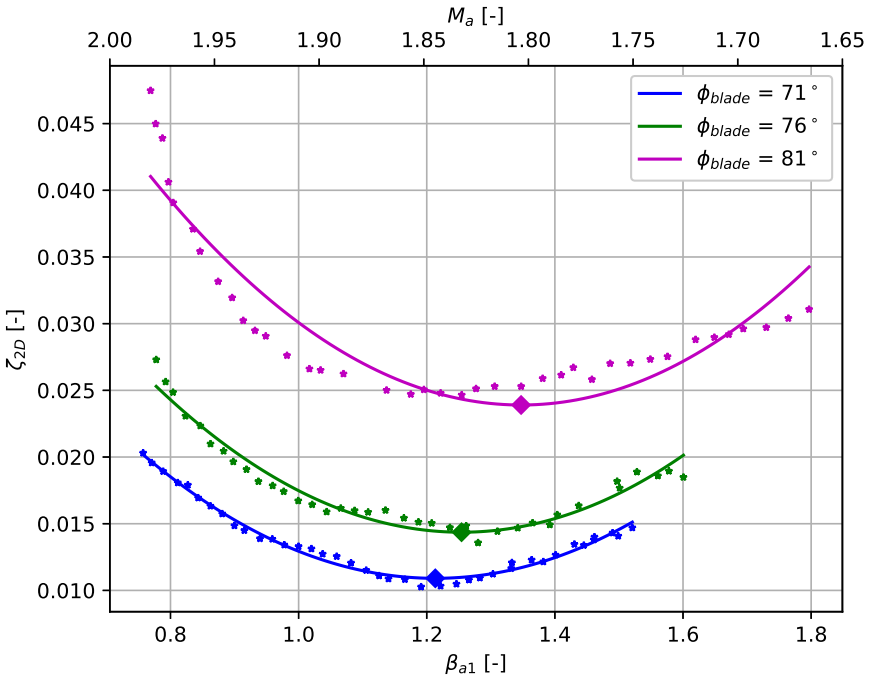

Figure 4.8: Plot of entropy generation loss coefficient with post-expansion ratio for ideal case for $\sigma = 2$, β_{t1}=8. The star markers are data points corresponding to each ϕ_{blade}. The solid lines represent 2nd order curve fitting of the data-points. The diamond markers represent $\beta_{\text{opt, a1}}$. Here, variation of $\beta_{\text{opt, a1}}$ with ϕ_{blade} is illustrated.

thickness as a % of the mean flow thickness, increases. This means an increase of the Boundary layer contribution to the total losses. With an increase in flow deflection, the pressure difference across the stator blade increases, thereby increasing mixing losses.

To explain observation (ii), a loss breakdown into nozzle losses(primarily viscous loss) and post-expansion losses (mixing, TE and shock losses) was carried out. The method adopted was to find the absolute entropy values at the domain stations of *o*, *a* and *1*. At these stations, points were extracted from the lines and mass flow-averaged. The difference in mass-flow averaged entropy at station *o* and *a* was accounted as nozzle loss, while between station *a* and *1* was accounted as the post-expansion region loss.

Figure 4.9 plots regional Δs with M_a. The upper graph plots Δs in the PE region and the lower graph plots Δs in the nozzle region. The discrete points are the actual data points while the lines are the fitted curves. The loss breakdown is showcased for three $\phi_{\text{blade}} \in [71, 76, 81]$. From figure 4.9, it is observed that the PE losses increase with ϕ_{blade} but the optimum points of the PE losses for all ϕ_{blade} is found at the same M_a. The nozzle losses show an interesting pattern. They increase in magnitude with both M_a and ϕ_{blade}. The slope of these nozzle losses also increase with ϕ_{blade}. Higher slope for higher ϕ_{blade} is the reason for the shift observed in the optimum values of β_{a1}. The effect of the slope of the nozzle losses on the optimum point can be seen in the figure 4.9.

Figure 4.10 shows the variation of ϕ_{blade} with ζ_{2D} for three values of M_a. The three values of M_a have correspond to post-expansion, optimum point and post-compression cases for constant ϕ_{blade}, σ and β_{t1}. The star markers are discrete data points while the solid lines are curve-fitted to these data-points. The loss coefficient can be seen as an increasing logarithmic function of ϕ_{blade}. The logarithmic fit was preferred over a second-order polynomial fit since the nozzle losses largely comprise of the boundary layer losses which scale with ϕ_{blade} but only reduce as the flow deflection decreases. When further investigated, it was found that with increase in ϕ_{blade}, for the same M_a, the throat cross-section decreases. The mass flow rate through the throat remains constant as the throat is choked. The decrease in the cross-sectional area of flow is accompanied by an increase in the local density of the fluid, thereby keeping the mass-flow rate constant. With increase in ϕ_{blade}, increasing flow deflection is accompanied by a higher % of the flow thickness being occupied by the boundary layer thickness. The contribution of the viscous dissipation and hence nozzle loss to the 2D losses

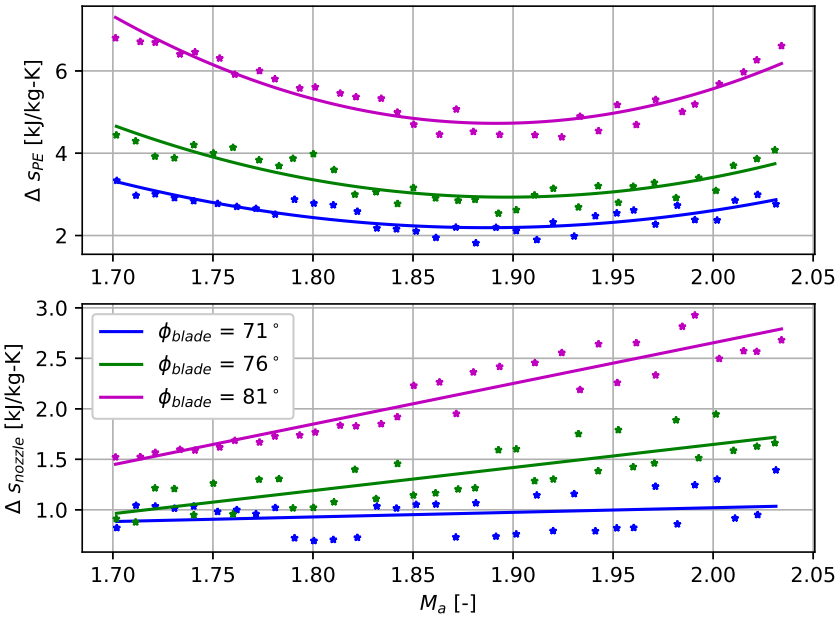

Figure 4.9: Breakdown of entropy generation for nozzle and post-expansion region for different ϕ_{blade}. Bottom graph plots the Δs for nozzle with respect to nozzle exit Mach number and the top graph plots Δs for post-expansion region with the same.

hence increases.

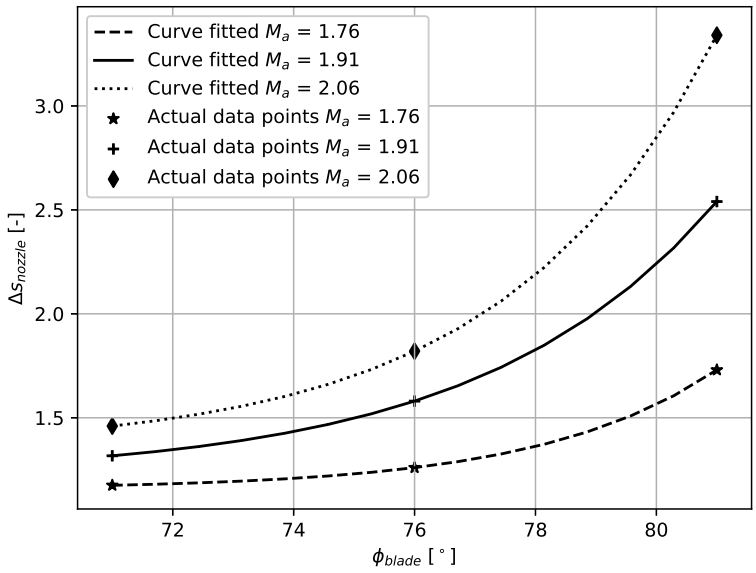

Figure 4.10: Entropy generation in nozzle vs ϕ_{blade} for three values of M_{a}.

From the numerical simulations carried out, the relation between the nozzle losses with respect to ϕ_{blade} is given by the equation 4.1. The equation can be seen as a logarithmic growth function.

$$\Delta s_{\text{noz}} = \text{c} - \frac{\text{a}}{\text{b}}(1 - e^{-\text{b}|\phi_{\text{blade}}|}), \tag{4.1}$$

where a, b and c are dependent on the value of M_{a} and are dimensionless quantities, while ϕ_{blade} is the

metal blade angle in radians. They are listed in table 4.1.

Table 4.1: Logarithmic curve fit coefficients for ϕ_{blade} vs M_a relation.

M_a	a	b	c
1.76	-5.22e-12	-9.79	1.156
1.91	-7.62e-09	-8.25	1.21
2.06	-1.20e-09	-7.42	1.34

4.2.2. $\beta_{OPT,\,A1}$ VARIATION WITH β_{T1}

The next study carried out was with primary design parameter β_{t1}. The simulations were carried out for the design range of ϕ_{blade} for two values of β_{t1}: [6, 8]. This was done by keeping the total inlet conditions constant while changing the stator outlet pressure (P_1). There is no geometric change with β_{t1} because nozzle shape depends on M_a. Results from this study is showcased in the figure 4.11a where, ζ_{2D} is plotted with β_{a1} for β_{t1} equal to 6 and 8, $\phi_{blade} = 81°$ and $\sigma = 2$. The star and circle markers represent the actual data-points for their corresponding β_{t1}, while the lines represent their curve fitted value. The diamonds represent $\beta_{opt,\,a1}$ for each of the β_{t1}.

The entropy generation coefficient was computed using equation 4.2. In order to compare the coefficient values for vanes operating at different β_{t1} values, ζ_{2D} for $\beta_{t1} = 8$ is normalized using a constant spouting velocity corresponding to v_{spout} of $\beta_{t1} = 6$.

$$\zeta_{2D} = \frac{\Delta s}{v_{spout}} \; ; \; v_{spout} = \frac{2 * (H_0 - H_{1,is})}{T_t}, \tag{4.2}$$

where H_t is the total enthalpy at inlet and $H_{1,is}$ is the isentropic enthalpy at the outlet of the stator blade. T_t is the total temperature at the inlet of the flow domain.

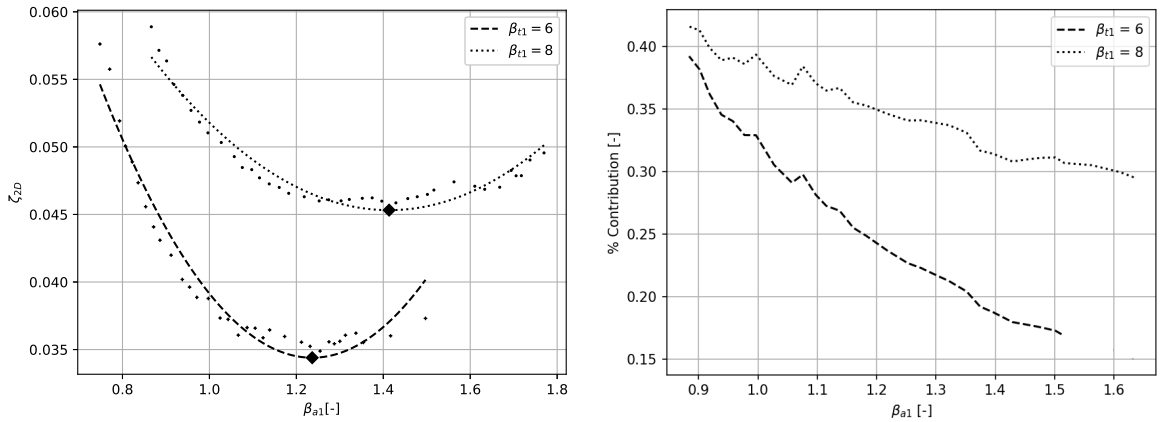

(a) **(b)**

Figure 4.11: (a) Plot of ζ_{2D} with design range of β_{a1} for $\beta_{t1} \in$ [6,8]. (b) Plot of nozzle loss contribution with design range of β_{a1} for $\beta_{t1} \in$ [6,8].

From figure 4.11a, two observations are made:

i. For the same value of β_{a1}, 2D loss increases with β_{t1}.

ii. $\beta_{opt,a1}$ increases with β_{t1}.

The reason for observation (i) is that for the same range of β_{a1} values, the design range of M_a, for a greater β_{t1} is higher. Therefore, for $\beta_{t1} = 6$, $M_a \in$ [1.6,2] while for $\beta_{t1} = 8$, $M_a \in$ [1.8, 2.2]. Boundary layer losses scale with the cube of mach number. Thus for the same value β_{a1}, but different β_{t1}, boundary layer losses in the nozzle and PE region are higher for higher β_{t1}.

An investigation into observation (ii) was carried out. A loss breakdown into the nozzle and PE loss was performed to view the nozzle and PE loss behavior. PE loss comprises of the mixing loss, shock loss and TE loss. A comparison of the trailing-edge loss for two nozzle shapes undergoing the same nozzle expansion but different post-expansion was performed. This was calculated using the base pressure at the TE, P_{ref}, ρ_{ref} and u_{ref} as shown in equation 4.3.

$$C_{\text{pb}} = \frac{P_{\text{b}} - P_{\text{ref}}}{0.5\rho_{\text{ref}} u_{\text{ref}}^2}. \tag{4.3}$$

The reference values were taken at station a as advised in [21]. Table 4.2 shows the value of C_{pb} obtained for the same nozzle undergoing two different expansion states.

Table 4.2: Base pressure coefficient calculation for $\beta_{t1}\ \epsilon$ [6,8].

	$\beta_{\mathbf{t1}}$ **= 6**	$\beta_{\mathbf{t1}}$ **= 8**
$\mathbf{P_b}$ [Pa]	0.74e5	0.637e5
$\boldsymbol{\rho}_{\mathbf{ref}}$ [kg/m^3]	4.411	3.413
$\mathbf{P_{ref}}$ [Pa]	1.867e5	1.76e5
$\mathbf{u_{ref}}$ [m/s]	389.16	414.76
$\mathbf{C_{pb}}$ [-]	-0.337	-0.383

The value of C_{pb} for β_{t1}=6 is lower than that for 8. Referring to equation 4.4,

$$\zeta_{\text{mix}} = -C_{\text{pb}}\frac{t}{l} + \underbrace{2\frac{\theta}{l}}_{=c_1} + \underbrace{\left[\frac{\delta^* + t}{l}\right]^2}_{=c_2}. \tag{4.4}$$

c1 and c2 are constants for both the cases since it is a comparison of a single stator blade with Toluene undergoing two different expansions. Thus ζ_{mix} becomes a function of only the base pressure coefficient. The mixing loss coefficient for the two cases is presented in table 4.3. The value of ζ_{mix} for both the cases are comparable while ζ_{2D} for 8 is higher than 6. This means that the nozzle loss contribution is increasing with increase in β_{t1}.

Table 4.3: Mixing loss coefficient calculation for ideal and non-ideal thermodynamic states.

	$\beta_{\mathbf{t1}}$**=6**	$\beta_{\mathbf{t1}}$**=8**
$\boldsymbol{\zeta}_{\text{mix}}$ [-]	1.93e-2	2.167e-2

Since TE loss is a contributing mechanism to the PE losses, the contribution of the PE loss decreases with increase in β_{t1} while the nozzle loss contribution increases.

Figure 4.11b, illustrates the % contribution of nozzle loss to 2D loss for β_{t1} 6 and 8 for a range of β_{a1}. It is observed that the contribution of nozzle loss is lower for a lower value of β_{t1}.

The two observations and the following study leads to the conclusion that with increasing β_{t1}, nozzle contribution to 2D loss decreases, due to which the value of $\beta_{\text{opt, a1}}$ increases

4.2.3. $\beta_{OPT,\,A1}$ VARIATION WITH σ

The next design parameter with which the behavior of ζ_{2D} and $\beta_{opt,\,a1}$ was investigated was the nozzle solidity. σ was varied from 1.5-2 with a step size of 0.25.

The effect on the geometry can be seen in figure 4.12. In this figure, the nozzle solidity has been varied from 1 to 2. With increasing nozzle solidity, the stator chord length increases while the axial pitch remains constant. Also, L_o remains constant.

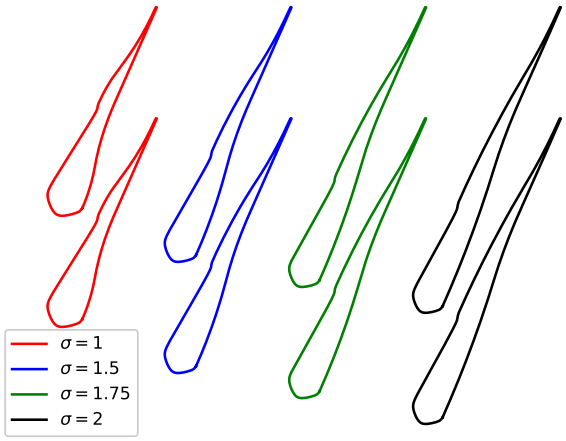

Figure 4.12: Variation of vane geometry with σ. From left to right, the axial pitch remains constant while the blade chord increases, thereby increasing nozzle solidity.

An increase in solidity, indicates higher boundary layer losses in the nozzle and constant mixing losses for the same post expansion ratio. An increase in the contribution of the nozzle losses predicts that the $\beta_{opt,\,a1}$ should increase (ie. move further away from 1 along the positive axis). Figure 4.13 shows the variation of ζ_{2D} with β_{a1} for ϕ_{blade}=66 and 76 °. For each ϕ_{blade}, ζ_{2D} is plotted with three values of σ. The 2D loss shows marginal increase with a higher σ. The lines are curve fitted as a second order polynomial while the diamond markers represent the corresponding $\beta_{opt,\,a1}$. From figure 4.13a and 4.13b, it is observed that the $\beta_{opt,a1}$ trend with σ shows opposing trends.

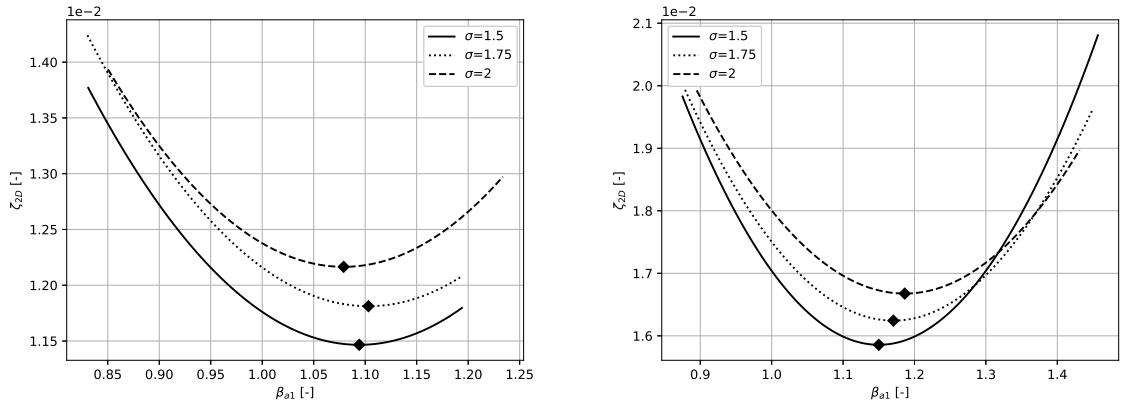

(a) ϕ_{blade} = 66°.

(b) ϕ_{blade} = 76°.

Figure 4.13: Plot of ζ_{2D} with β_{a1} for $\sigma \in [1.5, 1.75, 2]$. The diamonds represent $\beta_{opt,\,a1}$ and the continuous lines represent curve-fitted data points.

To further investigate the effect of solidity, the flow contours for each value in the design range of σ are plotted. In figure 4.14, Mach contours are plotted for the three values of $\sigma \in [1.5, 1.75, 2]$. From these contour plots, flow features such as flow deviation at stator exit, location of boundary layer-shock wave interaction and strength of trailing edge shocks remain indistinguishable. The only difference is that the expansion is more gradual for a higher σ as compared to a lower value of σ. The combined observations from the Mach contours and the β_{a1} vs σ plots leads to the conclusion that the effect of nozzle solidity on $\beta_{opt,\,a1}$ is insignificant. However, for the formulation of design correlations presented in section 4.4, the effect of solidity has been captured mathematically.

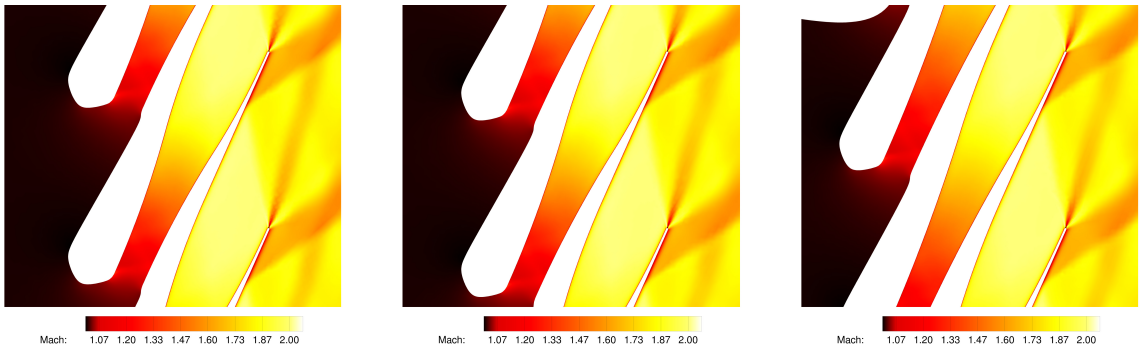

(a) **(b)** **(c)**

Figure 4.14: Mach contour plots for varying σ. (a)$\sigma = 1.5$ (b)$\sigma = 1.75$ (c)$\sigma = 2$.

4.2.4. $\beta_{OPT,\,A1}$ VARIATION WITH INLET CONDITIONS

The last set of design parameters investigated for β_{a1} were with the total inlet conditions - $[P_t, T_t]$. The inlet conditions of total pressure and total temperature were varied to observe the effect of flow non-ideality. Their variation led to a deviation in the value of compressibility factor from 1, which was used as an indicator to describe the extent of non-ideality in the flow. Lower the value of z, more is the non-ideality. Table 4.4 showcases specifically three cases that have been analyzed for effect of non-ideality on β_{a1}. The compressibility factor, specific heat capacity ratio (γ_{PV}) and the fundamental derivative (Γ) have been calculated at the stator inlet. γ_{PV} and Γ have been calculated using the E.W. Lemmon and R. Span equation of state [36] from CoolProp.

Table 4.4: Total inlet conditions, corresponding compressibility factor, Γ and γ_{PV} for three test cases.

	P_t [Pa]	T_t [K]	Z [-]	Γ	γ_{PV}
Ideal Case	10e5	540	0.87	0.905	1.0450
Semi-ideal Case	20e5	550	0.74	0.732	1.0389
Non-ideal Case	32e5	580	0.57	0.640	1.0291

For all the inlet conditions, the investigations were carried out with ϕ_{blade}, β_{t1} and σ using the same ADCT and post-processing algorithm.

Figure 4.15 shows the effect of non-ideality on the geometry of the stator blades. In the figure, with non-ideality, chord length of the stator blade for the same M_a increases while L_o decreases. This means that with non-ideality, to achieve the same mach number, the DoD is higher. To investigate this, the Mach number along the nozzle chord was plotted for a nozzle undergoing expansion in the ideal and non-ideal case.

Figure 4.16 shows a stator blade undergoing expansion for the ideal and non-ideal case for $M_{a,\,design} = 2$. It is observed that with the same DoD, the stator does not achieve the same value of M_a, hence the same amount of expansion in the non-ideal case. The reason for this observation lies in the change in the value of γ_{PV} which depends on the flow non-ideality, that in turn depends on the inlet conditions. γ_{PV} at the inlet for the non-ideal case is equal to 1.291 while for the ideal case is equal to 1.450. Equation 4.5 is the isentropic relation between the area ratio of nozzle exit and the throat with the specific heat capacity ratio (adjusted as per inlet conditions) of the working medium and Mach number at the nozzle exit.

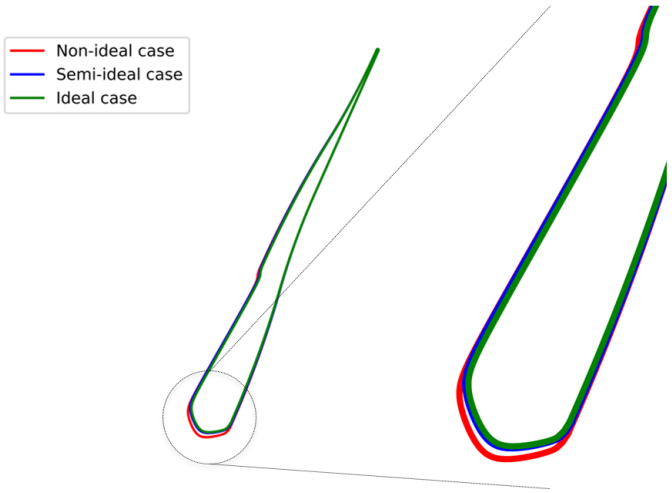

Figure 4.15: Variation of vane geometry with respect to non-ideality. The right image is a magnified image of the left which shows an increase in DoD with non-ideality.

$$\frac{A_a}{A_o} = \left(\frac{\gamma_{PV}+1}{2}\right)^{-\frac{\gamma_{PV}+1}{2(y-1)}} \frac{\left(1+\frac{\gamma_{PV}-1}{2}M^2\right)^{\frac{\gamma_{PV}+1}{2(\gamma_{PV}-1)}}}{M} \tag{4.5}$$

For the comparison made in figure 4.16 where design M_a=2, area ratio for the ideal case (γ_{PV}=1.45) is equal to 2.13 while for the non-ideal case (γ_{PV}=1.291), it is equal to 2.17. This indicates that for the same nozzle exit Mach number, an expansion in a more non-ideal flow requires a higher DoD as compared to a more ideal flow.

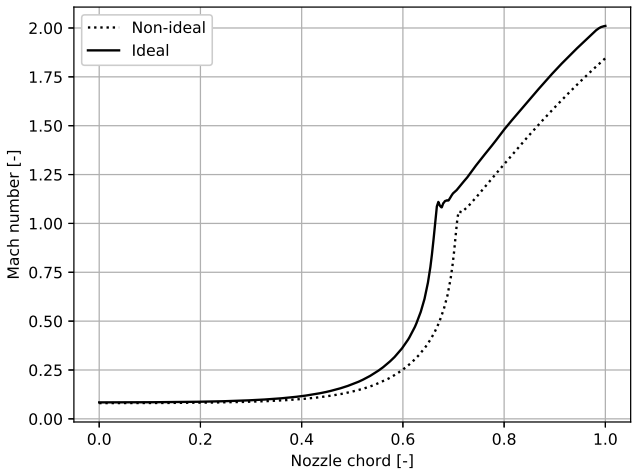

Figure 4.16: Plot of Mach number along a streamline vs the nozzle chord for the ideal and non-ideal case.

After establishing the effect of non-ideality on the stator nozzle and vane geometry, the analysis of $\beta_{opt,a1}$ with respect to the inlet conditions was carried out in the following steps:

- Variation of β_{a1} with respect to ζ_{2D} for the three inlet conditions for $\phi_{blade} \in [66, 71, 76, 81]^\circ$ was plotted.
- To investigate the behavior of $\beta_{opt,\,a1}$ with respect to inlet conditions, loss breakdown into nozzle and post-expansion region loss was carried out for the ideal and non-ideal case.

- To explain the loss breakdown behavior, the contour plots of variable-entropy were created and the flow phenomena was analyzed.

Figure 4.17 presents $\beta_{\text{opt, a1}}$ with respect to the inlet conditions for different ϕ_{blade}. Figure 4.17a and 4.17b represent the ideal and non-ideal case. In both the figures, the trend of ζ_{2D} with respect to $\phi_{\text{blade}} \in [66, 71, 76, 81]°$ is shown. The lines are curve-fitted values of the actual data as a second order polynomial. For both inlet conditions, $\beta_{\text{opt, a1}}$ increases with ϕ_{blade}. This as already established is because of the increasing nozzle contribution to the total loss. Another observation made is that with non-ideality, the value of $\beta_{\text{opt, a1}}$ for the same ϕ_{blade} increases (moving away from one). This means higher expansion in the PE region than in the nozzle region leads to better performance in case of non-ideality. To investigate this a loss breakdown is performed.

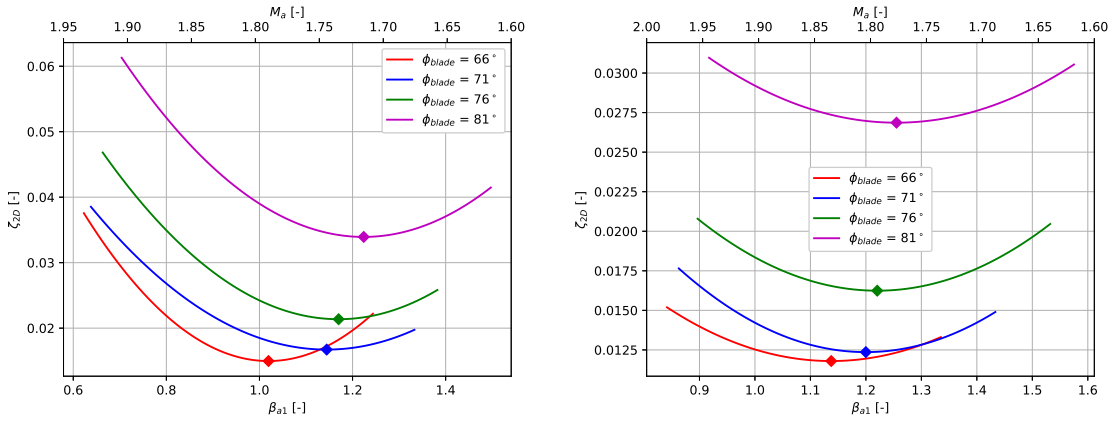

(a) Ideal case (Z ∈ [0.87, 0.97]).

(b) Non-ideal case (Z ∈ [0.57, 0.92]).

Figure 4.17: Variation of ζ_{2D} with β_{a1} for ϕ_{blade} for σ=2, β_{t1}=6. Solid lines represent the quadratic fit of discrete points obtained from CFD. Diamond markers represent $\beta_{\text{opt,a1}}$ for corresponding ϕ_{blade}.

The loss breakdown was carried out for four ϕ_{blade} for each of the ideal and non-ideal cases, from which the case for σ=2, ϕ_{blade}=76° has been presented in figure 4.18 and 4.19. From these figures, the following observations are made:

i. The total specific entropy generated for the ideal case is greater than that of the non-ideal ideal case.

ii. The $\beta_{\text{opt, a1}}$ for the ideal case is lower than that of the non-ideal case.

iii. The minimum PE loss for both cases occur at a value slightly greater than one.

iv. The contribution of nozzle losses is lower in the ideal case as compared to that of the non-ideal case.

To explain the aforementioned observations, the ideal and non-ideal flow domain was observed. Observation (iv) states that with non-ideality, the nozzle contribution to the total losses increase, hence, more expansion should be performed in the PE region than in the nozzle. To investigate the reason for this three studies were performed:

i. The entropy contours for two stator blades with the same post-expansion ratio for the two inlet conditions are presented in figure 4.20 and 4.21. In both figures, a separation bubble is observed which is formed due to the boundary layer-trailing edge shock interaction on the suction side of the blade. The streamlines in this zone are also showcased. It is observed for the ideal case, the entropy generation in the re-circulation zone is higher than as compared to the non-ideal case. The re-circulation zone is formed in the PE region.

ii. The second study performed was at the trailing edge of both cases to estimate the trailing edge and mixing loss. The base pressure and density values were probed at the re-circulation region behind the trailing edge while the reference values of pressure and velocity were extracted at station a as advised in [21]. For each of the cases, these values have been presented in the table 4.5. The value of C_{pb} for the

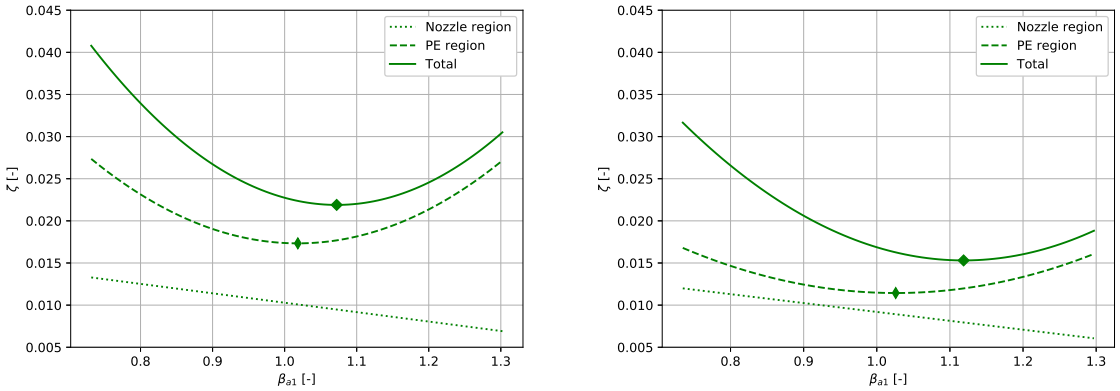

(a) Ideal case

(b) Non-ideal case

Figure 4.18: Variation of ζ_s with respect to β_{a1} for total, nozzle and PE region. The small and larger diamond represent β_{a1} corresponding to minimum PE and total entropy generation coefficient respectively.

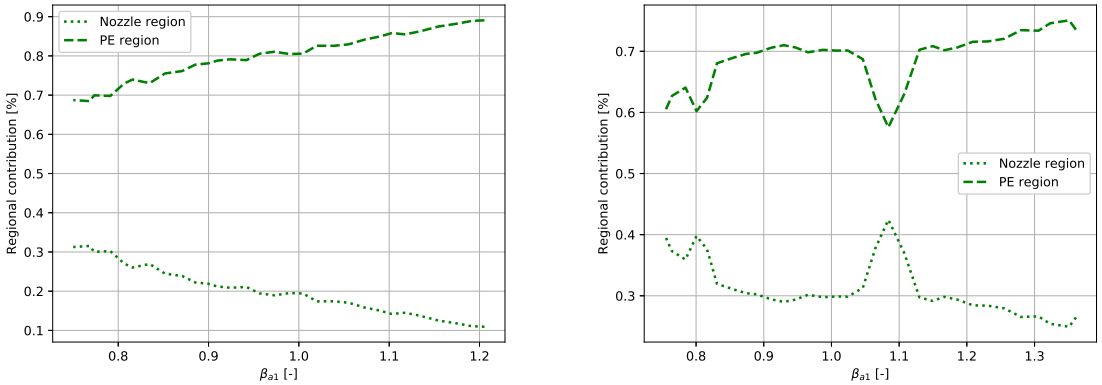

(a) Ideal case.

(b) Non-ideal case.

Figure 4.19: Variation of % contribution of nozzle and PE region to total losses with respect to β_{a1}.

	Ideal case	**Non-ideal case**
$\mathbf{P_b}$ [Pa]	0.611e5	2.315e5
$\boldsymbol{\rho}$ [kg/m^3]	1.39	4.88
$\mathbf{P_{ref}}$ [Pa]	1.0597e5	3.3486e5
$\mathbf{u_{ref}}$ [m/s]	443.69	430.745
$\mathbf{C_{pb}}$ [-]	-0.3279	-0.228

Table 4.5: Base pressure coefficient calculation for ideal and non-ideal case.

ideal case is lower than that of the non-ideal case. Referring to equation 4.6,

$$\zeta_{mix} = -C_{pb}\frac{t}{l} + \underbrace{2\frac{\theta}{l}}_{=c_1} + \underbrace{\left[\frac{\delta^* + t}{l}\right]^2}_{=c_2}. \tag{4.6}$$

The values are equal to c1 and c2 since they are essentially the same stator blades wherein the fluid is undergoing expansion at two different thermodynamic states. Thus due to geometric similarity, the mixing loss coefficient depends on the negative of the base pressure coefficient. From table 4.5, the negative of C_{pb} for the ideal case is higher than the non-ideal case. The mixing loss coefficient from

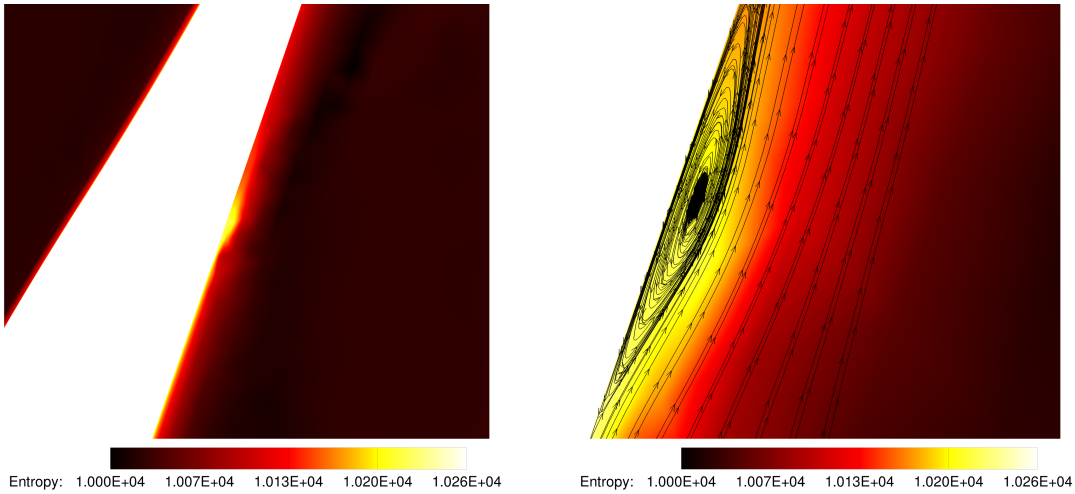

(a) **(b)**

Figure 4.20: Entropy contours for separation bubble formation for ideal case. (a) Zoomed out entropy contour, (b) Streamlines in the re-circulation zone.

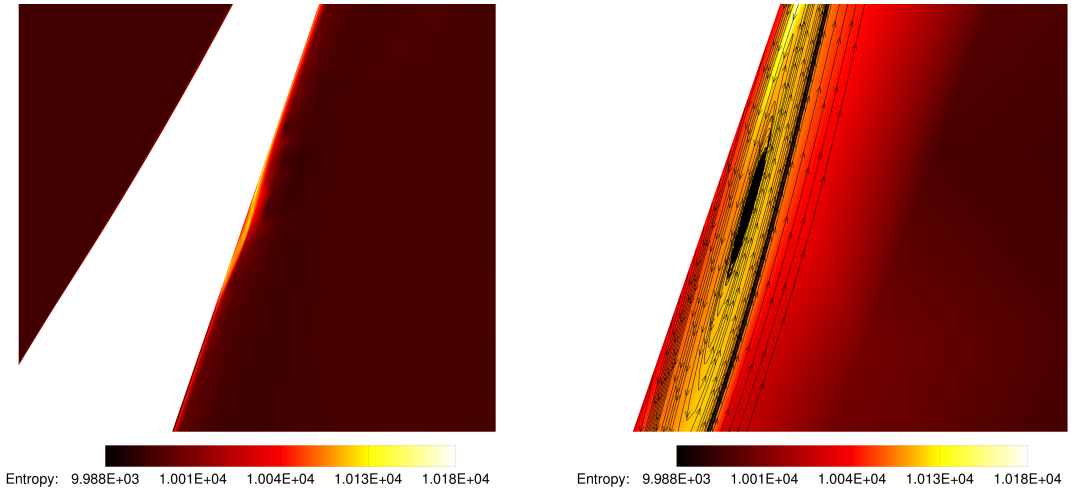

(a) **(b)**

Figure 4.21: Entropy contours for separation bubble formation for non-ideal case. (a) Zoomed out entropy contour, (b) Streamlines in the re-circulation zone.

equation 2.19 for both the cases are:

Table 4.6: Mixing loss coefficient calculation for ideal and non-ideal thermodynamic states.

	Ideal case	**Non-ideal case**
ζ_{mix} [-]	1.889e-2	1.391e-2

iii. The third study performed on the Mach number distribution along the center streamline for the ideal and non-ideal case. In figure 4.22, this distribution has been plotted and it is observed that in the supersonic region of the nozzle (Mach > 1), the Mach number for the ideal case is comparatively higher than the non-ideal case.

Studies (i) and (ii) indicate that entropy generated from shock wave-boundary layer interaction and the trailing edge shocks in the PE region for a nozzle geometry increases with ideality. This observation is justified

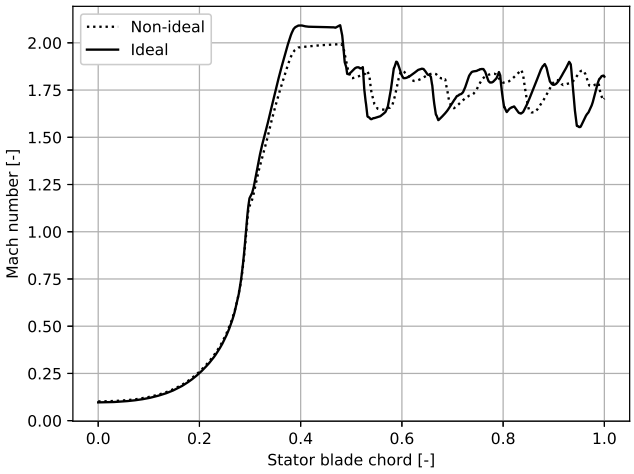

Figure 4.22: Plot of Mach number along a streamline vs the stator chord for the ideal and non-ideal case.

by the Δs_{shock} equation in Denton, 1993[21], which relates entropy generated across a shock wave with the specific heat capacity ratio and Mach number. With increase in the value of γ, the Δs_{shock} increases. γ_{PV} corresponding to the ideal case is equal to 1.045 while for the non-ideal case is equal to 1.0291 which verifies the observation from studies (i) and (ii). On the other hand, study (iii) shows that the Mach number during expansion in the nozzle is higher for the ideal case. Since it is established, that Δs_{noz} increases with increase in M_{a}, the third study states entropy generation in a nozzle geometry increases with ideality. It is important to note in figure 4.19 even though both nozzle and PE losses increase with ideality, the nozzle loss contribution to 2D losses decreases with ideality. Thus, the decreasing nozzle loss contribution with ideality leads to a lower value of optimum post expansion for the ideal case as compared to that of the non-ideal case.

4.3. ψ VARIATION WITH INLET CONDITIONS

A study was carried out to find the trend of variation of the flow deviation angle with respect to design parameters and the optimum β_{a1} values. Figure 4.23 illustrates mach contour in the flow domain for three different cases, (a) β_{a1}>1, (b) β_{a1}=1 and (c) β_{a1}<1. Streamlines are drawn in the domain which represent the velocity vectors of fluid particles. In figure 4.23a and 4.23c, the flow at the blade exit undergoes negative and positive deviation respectively. This is because for a $\beta_{\text{a1}} > 1$, an expansion fan is seen on the pressure side of the blade. This expansion fan deflects the mean flow to a lower angle (with respect to the horizontal) as compared to the blade angle. On the other hand, when the β_{a1} value < 1, there is a strong shock wave at the pressure side and an expansion fan at the suction side. This combined effect deflects the mean flow to a greater angle as compared to the blade angle. For β_{a1} value = 1, there is no flow deviation observed. From the study, it can be concluded that with increasing post-expansion ratio, the mean flow loses angle, thus leading to a negative flow deviation.

After establishing this idea, the flow deviation angles corresponding to the optimum points were plotted with respect to ϕ_{blade} for all three inlet conditions.

Figure 4.24 illustrates flow deviation values corresponding to optimum design plotted with ϕ_{blade} for ideal, semi and non-ideal cases. The discrete points represent ψ while the lines showcase the trend. In the lower graph, the variation of $\beta_{\text{opt, a1}}$ is shown with ϕ_{blade}. It can be seen from this figure, that with the inlet thermodynamic state changing from ideal to non-ideal, the optimum post-expansion ratios increase in value. This corresponds to the the flow deviation angle becoming more negative. The results correspond with the idea stated above that higher post-expansion leads to loss of flow angle. The performance of a stage is dependent on how efficiently both the stator and rotor stage operate. It is known that the stator directs the working medium such that the design velocity triangles are achieved and uniform flow enters the rotor stage. Thus the calculation of the flow deviation angle in any design procedure becomes paramount.

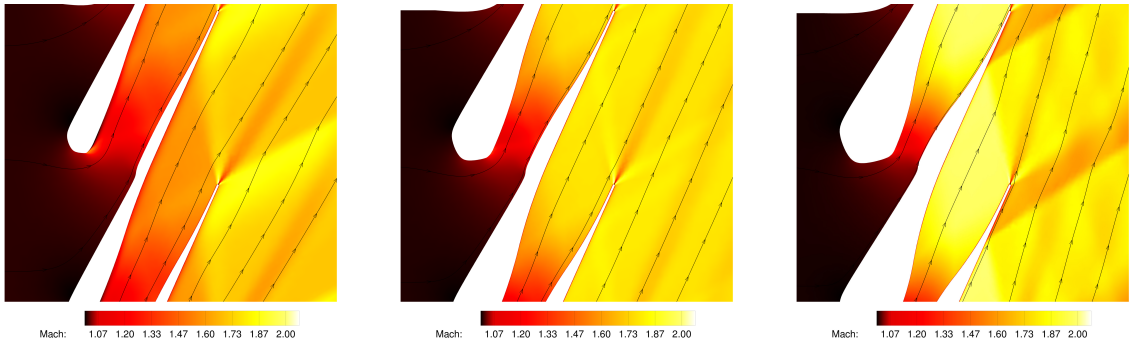

(a) Expansion in PE region. **(b)** β_{a1}=1. **(c)** Compression in PE region.

Figure 4.23: Streamline plots depicting flow deviation at stator outlet with varying β_{a1}.

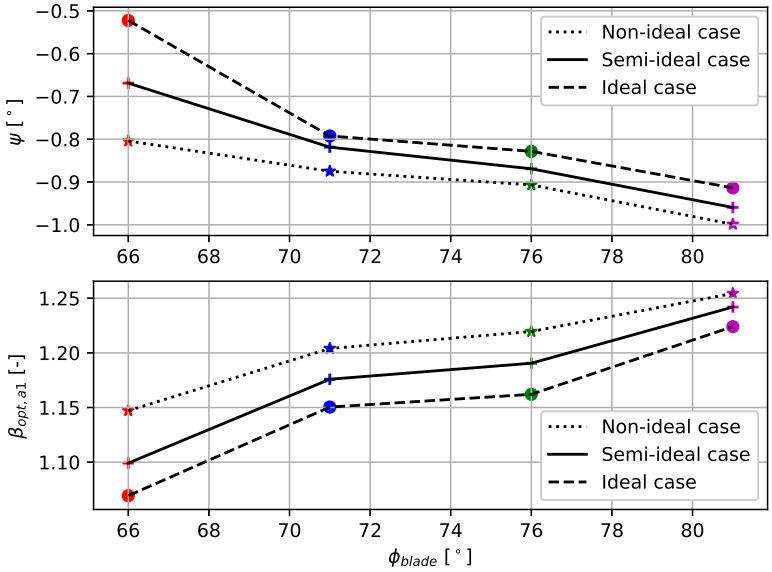

Figure 4.24: Plot of flow deviation angle ψ with respect to ϕ_{blade} for three inlet thermodynamic states. Discrete points represent value of ψ while the lines represent the trend.

4.4. FORMULATION OF DESIGN CORRELATIONS FOR IDEAL CASE

The previous sections held discussions and observations based on the trends of the values of β_{a1} and ψ corresponding to the optimum vane geometry, with respect to the design parameters and inlet conditions. For a single inlet condition, twenty-one optimum design points were obtained corresponding to the range of ϕ_{blade}, β_{t1} and σ. Thus two design correlations were formed using interpolation methods to encapsulate all the results and visualize them in one single frame:

$$\psi = f(\sigma,\ \beta_{\text{t1}},\ \phi_{\text{blade}}), \tag{4.7}$$

$$M_{\text{a,opt}} = f(\phi_{\text{blade}},\ \beta_{\text{t1}},\ \sigma). \tag{4.8}$$

There are several interpolation methods with different algorithms supporting their implementation and logic. The interpolation method used is based on least-squares method which is extended by constructing polynomial features using coefficients. For example in a simple linear regression, the model might look like the following,

$$\hat{y}(w,x) = w_0 + w_1\sigma + w_2\beta_{\text{t1}} + w_3\phi_{\text{blade}}. \tag{4.9}$$

Now when a dataset of a parabolic nature needs to be fitted, a more involved equation is used by extending this linear equation. The modified equation is of the form,

$$\hat{y}(w,x) = w_0 + w_1\sigma + w_2\beta_{t1} + w_3\sigma\beta_{t1} + w_4\sigma^2 + w_5\beta_{t1}^2. \tag{4.10}$$

These basis functions allow for the model to have more flexibility to fit the data. This is observed in the regression values too. Higher order polynomials, through Taylor expansion series suggest a more accurate approximation. However, as the number of terms increase, the model becomes more flexible and thus there is a danger of over-fitting the noise. This leads to the possibility of fogging the underlying response and leading to a poor generalization. This is why it was decided to limit the fitting model to a 2nd order polynomial fit as it showed the capability to co-relate the data sufficiently.

From the open-source models available, the sci-kit learn module in python was identified. It has a sub-module which is used to perform the polynomial fitting. This polynomial function is then used to interpolate in-between the data points. The input dataset can be divided into a training set and a testing set. The training set excludes a part of the data and finds the polynomial coefficients of the pre-defined second order function. The interpolated data from this polynomial is validated against the testing set and an output parameter - regression is generated. The closer the value of regression is to one, more accurate is the interpolation and the model prediction. To divide the input dataset into training and testing data, the split function of the sklearn module is used. The mathematics of the training and testing is given in detail on the sklearn tutorial website [37]. The regression score of the training and testing data is given in the table 4.7.

Table 4.7: Regression score for surrogate modeling.

Quantity	Training	Testing
R^2 **1st order**	0.9514	0.8706
R^2 **2nd order**	0.9968	0.9625

In figure 4.25, the training and testing set data is shown. The discrete points are the design points corresponding to the $\beta_{\text{opt,a1}}$ values and the lines are a set of points obtained after polynomial fitting. The plus markers denote the discrete points for σ=1.75 which is used as the testing set. All the remaining discrete points are used as a training set to find the polynomials. The regression score is then calculated and averaged for the entire data-set.

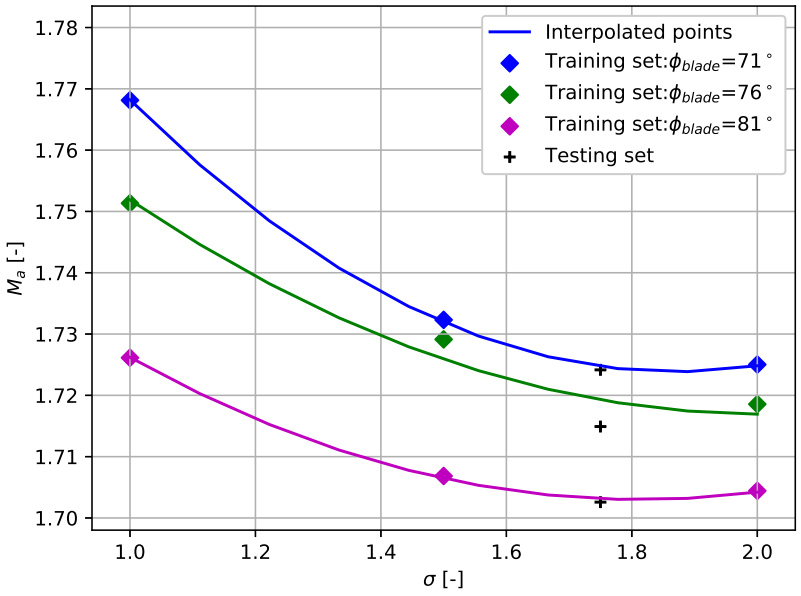

Figure 4.25: Verification of polynomial fitting by extracting slice and plotting with actual data points.

This regression score is a correlation coefficient which is calculated by equation 4.11 where *cov* is the covariance of y(original data-set) and $\hat{y}$(obtained data-set) while *var* is the variance of the two data-sets.

$$r^2 = \left(\frac{\text{cov}(y, \hat{y})}{\sqrt{\text{var}(y)\text{var}(\hat{y})}} \right)^2, \tag{4.11}$$

which is computed from the following equation,

$$r^2 = \left(\frac{n_t \sum_{i=0}^{n_t} y_i \hat{y}_i - \sum_{i=0}^{n_t} y_i \sum_{i=0}^{n_t} \hat{y}_i}{\sqrt{\left[n_t \sum_{i=0}^{n_t} y_i^2 - n_t \left(\sum_{i=0}^{n_t} y_i \right)^2 \right] \left[n_t \sum_{i=0}^{n_t} \hat{y}_i^2 - n_t \left(\sum_{i=0}^{n_t} \hat{y}_i \right)^2 \right]}} \right)^2. \tag{4.12}$$

From this table, it can be concluded that a second order polynomial relation between the design parameters is a more accurate method of fitting and interpolating than a linear polynomial. The second order polynomial for ϕ_{blade} and $M_{\text{a,opt}}$ are of the form:

$$\psi = a_0 + p(\sigma) + q(\beta_{\text{t1}}) + r(\phi_{\text{blade}}) + s(\sigma^2) + v(\beta_{\text{t1}}^2) + x(\phi_{\text{blade}}^2) + t(\sigma\beta_{\text{t1}}) + u(\sigma\phi_{\text{blade}}) + w(\beta_{\text{t1}}\phi_{\text{blade}}). \tag{4.13}$$

The coefficients for equation 4.13 are listed in the table 4.8. Value of a_0 is equal to +1.8048.

Table 4.8: Polynomial fit coefficients for flow and blade angle relation.

Coeff.	Value	Coeff.	Value	Coeff.	Value
p	1.43e-1	**q**	-5.79e-4	**r**	-4.863
s	-2.294e-2	**t**	-5.663e-3	**u**	2.477e-2
v	-8.108e-3	**w**	+1.124e-1	**x**	2.606

$$M_{\text{a,opt}} = a + b(\sigma) + c(\beta_{\text{t1}}) + d(\phi_{\text{blade}}) + e(\sigma^2) + h(\beta_{\text{t1}}^2) + j(\phi_{\text{blade}}^2) + f(\sigma\beta_{\text{t1}}) + g(\sigma\phi_{\text{blade}}) + i(\beta_{\text{t1}}\phi_{\text{blade}}). \tag{4.14}$$

The constants of the equation 4.14 are showcased in the table 4.9. Once this step was completed, the 3D contour plot was created using the interpolated values and is visualized in the figure 4.26.

Table 4.9: Polynomial fit coefficients for optimum M_{a} correlation with respect to ϕ_{blade}, σ, β_{t1}.

Coeff.	Value	Coeff.	Value	Coeff.	Value
b	9.748e-5	**c**	4.077e-2	**d**	-7.587e-2
e	4.343e-5	**f**	3.663e-3	**g**	-2.477e-3
h	1.364e-3	**i**	6.141e-4	**j**	4.523e-4

a is the intercept. It's value is equal to 4.612. From the table 4.9, it can be seen that the optimum M_a varies strongly with β_{t1} and ϕ_{blade}, while the variation with σ is diminished. This is also observed in the 3D contour plot 4.26. If the axis of ϕ_{blade} is observed, with increasing ϕ_{blade}, the optimum M_a decreases, signaling an increase in the optimum β_{a1}. With increasing β_{t1}, the optimum M_a increases but the trend of β_{a1} cannot be concluded from this as the stator outlet pressure and hence the M_1 is different. With σ, the change in M_a is almost negligible.

This plot 4.26 is generated for the most ideal inlet conditions. The design space includes two additional inlet conditions (semi and non-ideal) which are represented by two similar figures in the Appendix.

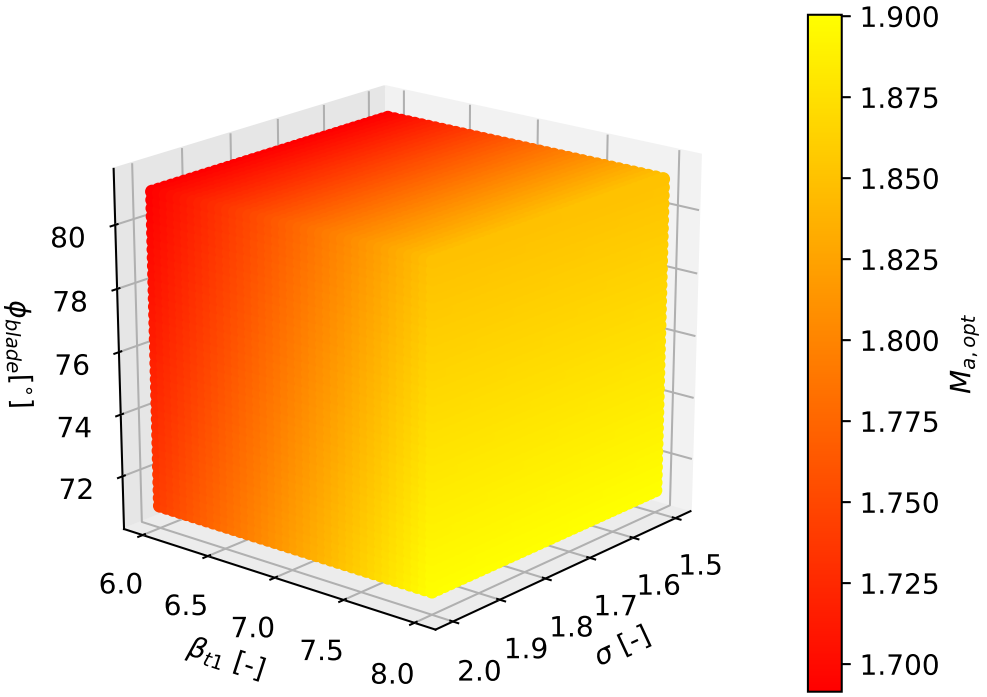

Figure 4.26: Optimum M_a with σ, ϕ_{blade}, β_{t1}.

4.5. VERIFICATION OF MACHINE-LEARNT MODELS

Two cases with different ϕ_{blade} as inputs are showcased and a comparison is made.

CASE 1

The first step in the design procedure is to fix the design variable inputs for ϕ_{corr}, σ, β_{t1}: [76°, 2, 6]. Once this is done, the next steps for the designer are as follows:

- Using the flow angle equation 4.13 and values of its coefficients from the table 4.9, the value of flow deviation angle corresponding to the optimum vane geometry is calculated. Hence for $\phi_{\text{blade}} = 76°$,

$$\psi = 1.8163 + (+0.143 \times 2) + (-5.79e-4 \times 6) + (-5.863 \times 76) + (-2.94e-3 \times 2^2) + (-8.108e-3 \times 6^2) + (+2.523 \times 76^2) + (-5.663e-3 \times 2 \times 6) + (+2.477e-3 \times 2 \times 76) + (+0.1114 \times 6 \times 76) \tag{4.15}$$

  From which the obtained ψ = **-1.06**°

- With the value of the blade angle and other design variables, equation 4.14 is used to calculate the optimum nozzle exit mach number. M_a is controlled by the degree of divergence of the nozzle.

$$M_{\text{a, opt}} = 4.612 + (9.748e-5 \times 2) + (4.077e-2 \times 6) + (-7.587e-2 \times 76) + (4.343e-5 \times 2^2) + (1.364e-3 \times 6^2) + (4.523e-4 \times 76^2) + (3.663e-3 \times 2 \times 6) + (-2.477e-3 \times 2 \times 76) + (6.141e-4 \times 6 \times 76) \tag{4.16}$$

  From which the obtained $M_{\text{a, opt}}$= **1.72**.

- With the obtained value of ϕ_{blade} and $M_{\text{a, opt}}$, the designer can use the MoC and AST tool to directly obtain the optimum nozzle and stator blade geometry. Hence in this case, the optimum geometry is showcased in the figure 4.27.

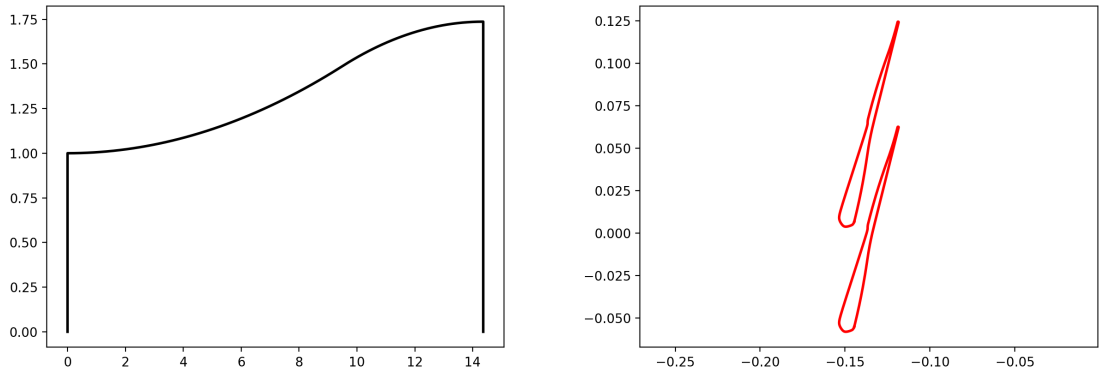

(a) Optimum nozzle geometry.

(b) Optimum stator blade geometry.

Figure 4.27: Optimum design of nozzle and stator blade for $\phi_{\text{blade}} = 76°$ obtained from design correlations.

CASE 2

The design variable inputs for this case for ϕ_{corr}, σ, β_{t1}: [66°, 2, 6]. Following the steps mentioned in the previous case:

- ψ = **-0.177**°
- $M_{a,\,opt}$= **1.77**

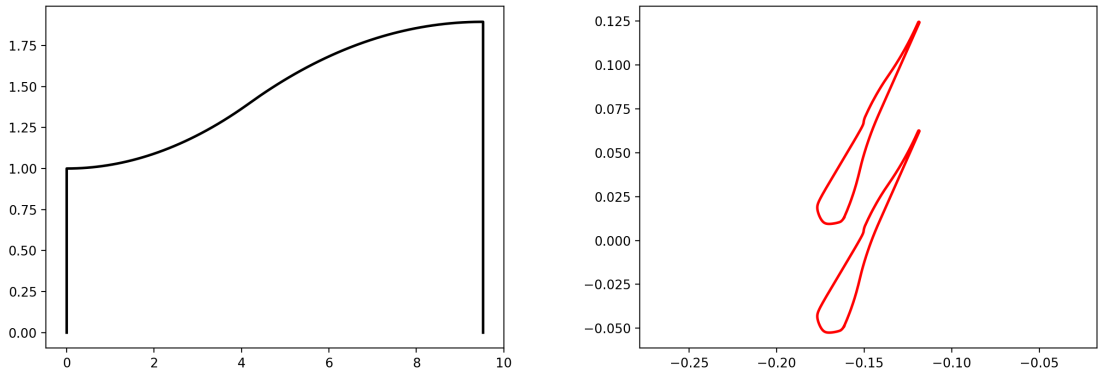

(a) Optimum nozzle geometry.

(b) Optimum stator blade geometry.

Figure 4.28: Optimum design of nozzle and stator blade for $\phi_{blade} = 66°$ obtained from design correlations.

From the two cases presented above, it is seen that with increase in ϕ_{blade}, the optimum point is found at a lower M_a. This means a lower DoD. The DoD for case 1 is equal to 1.73 while for case 2 is 1.76. A lower expansion in case 1 means that the post-expansion ratio is higher for higher ϕ_{blade}. Also, with increase in ϕ_{blade}, value of ψ decreases. Thus the correlations correspond with the optimum design points obtained and can be used by a designer.

4.6. PERFORMANCE COMPARISON

From the design correlation, M_a corresponding to the optimum blade design is found. A performance comparison of the design obtained from the proposed correlation has been made in the two following cases:

I. Performance comparison of optimum stator blade design obtained from proposed design correlation and empirical relation.

II. Performance comparison of interpolated $M_{a,\,opt}$ for β_{t1}=7, ϕ_{blade}=71° and σ=2 with ±10% and ±20% M_a.

4.6.1. CASE (I)

The empirical correlation between DoD and M_1, proposed by [15] is equation 4.17.

$$\text{DoD}_{empirical} = \frac{A_a}{A_o} = \begin{cases} 1, & \text{for } M_1 \leq 1.4 \\ 1 + (0.5M_1 - 0.4)\left[\frac{1}{A_{is}(M_1,\gamma)} - 1\right], & \text{for } M_1 > 1.4 \end{cases} \tag{4.17}$$

In this equation, M_1 is the stator design Mach number and A_{is} is the area ratio corresponding to an isentropic expansion. This equations has two divisions since it physically means that for subsonic or transonic flows, the blade does not require a diverging section while for supersonic flows a diverging section is necessary. From this equation, the value of $\beta_{opt,\,a1}$ is calculated as follows.

Firstly from isentropic equations the value of M_1 is found. For β_{t1} = 6, P_t = 10e5 Pa, P_1 is equal to 1.66e5 Pa. From the equation 4.18, given as

$$\frac{P_1}{P_t} = \left[1 + \frac{\gamma - 1}{2} M_1^2\right]^{\left(\frac{-\gamma}{\gamma - 1}\right)}, \tag{4.18}$$

M_1 = 1.887.

This gives an area ratio A_{is} equal to 1.829. This value when substituted into equation 4.17, outputs DoD equal to 1.4506. This value of DoD corresponds to a $\beta_{opt,\,a1,\,empirical}$ equal to **1.12**. From the design correlation proposed, the value of $\beta_{opt,\,a1,\,corr}$ is equal to **1.03**.

In figure 4.29, the stator blade design and density contours from empirical and proposed correlations are shown. The DoD for proposed design is higher than that of the empirical design. The density contours show a higher density gradient for the stator designed by means of empirical model, which means higher loss from trailing edge shocks.

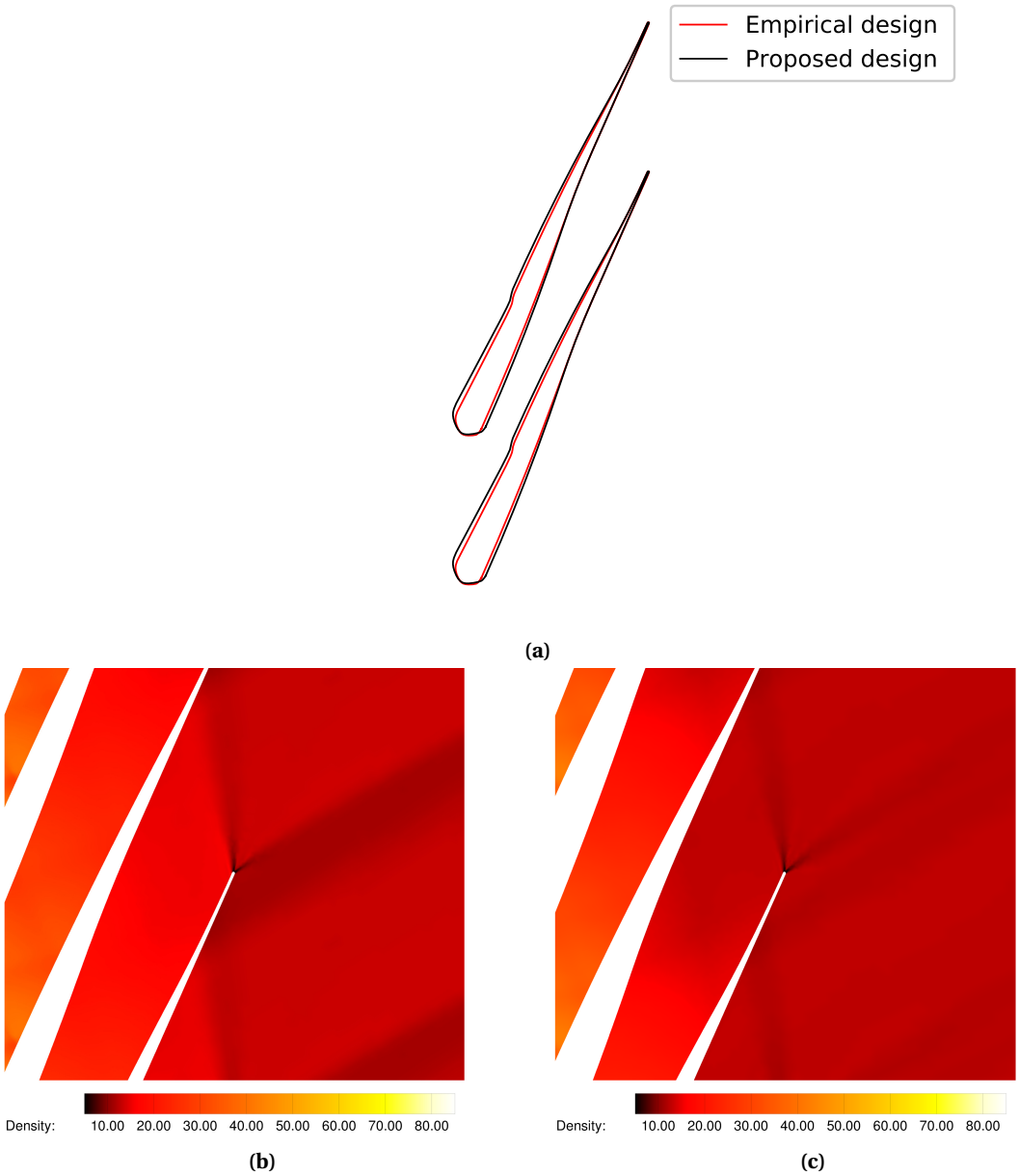

Figure 4.29: (a) Blade geometry comparison for optimum design from empirical and proposed correlation. (b) Density contour for optimum stator blade from empirical correlation. (c) Density contour for optimum stator blade from proposed correlation.

The performance of the two designs were compared with the help of the entropy generation and kinetic energy loss coefficients. Both loss coefficients were found to be lower for $\beta_{\text{opt,a1, corr}}$. The % improvement in terms of entropy coefficient was found to be 2.4% while in terms of kinetic energy loss coefficient was found to be 4.8%. This comparison is tabulated in table 4.10.

Table 4.10: Comparison of stator performance using loss coefficients of entropy generation and kinetic energy loss.

	Empirical	**Proposed**	**% difference**
$\zeta_{\mathbf{2D}}$	0.01262	0.01233	2.4
$\xi_{\mathbf{2D}}$	0.01237	0.01226	4.8

4.6.2. CASE (II)

In this case, the design correlation is tested by comparing the value of loss coefficient obtained from the vane corresponding to value of $M_{\text{a, opt}}$ with that of ±10% and ±20% of $M_{\text{a, opt}}$. The design input parameters used for the test case are: $\sigma = 2$, β_{t1}=7 and ϕ_{blade}= 73°. With these as inputs for equation 4.7, ϕ_{corr} was calculated which was further used as an input in equation 4.16 to find value of $M_{\text{a, opt}}$ which was equal to 1.87.

Figure 4.30 illustrates values of kinetic energy loss and entropy generation coefficient with respect to nozzle exit mach number. The red diamond in the figure represents the loss coefficient value corresponding to the optimum vane design while the black markers represent loss coefficient corresponding to vanes with ±10% and ±20% M_{a}. It is observed that the loss coefficient values of the optimum vane is lower than that of other vanes. This henceforth proves that the interpolated values from the design correlation correspond to the optimum vane design and also back the hypothesis successfully.

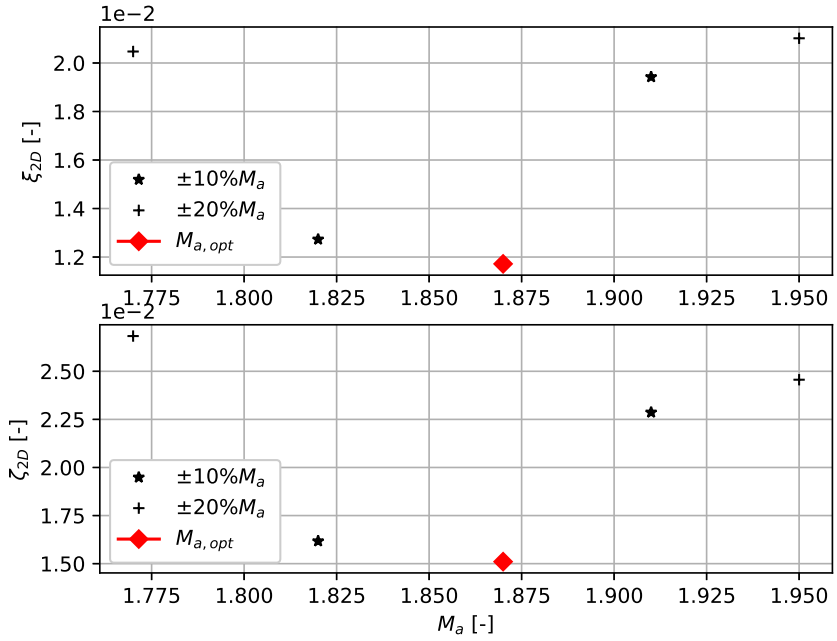

Figure 4.30: Plot of entropy generation and kinetic energy loss coefficient with M_{a}. Red diamond indicates M_{a} corresponding to optimum vane geometry while the asterisk and plus markers represent 10 and 20% Mach deviation from optimum point.

5

CONCLUSIONS AND RECOMMENDATIONS

The objective of this thesis was to study the trend of stator losses with the variation of geometric design variables and inlet conditions, subsequently to qualitatively and quantitatively assess the performance of the blade and finally to propose new design correlations for the organic fluid Toluene. The following sections summarize the results, highlight the conclusions and propose recommendations for future work.

5.1. CONCLUSIONS

VERIFICATION OF HYPOTHESIS

During the preliminary phase of this project, it was concluded from the literature study that viscous, mixing and shock losses are dominant in a supersonic stator vane. Additionally it was hypothesized that the total losses are minimum for a unique value of post-expansion ratio. To test this hypothesis, a semi-automated analysis framework was made, wherein vanes with varying post-expansion ratio (alternatively nozzle exit mach number or degree of divergence) are constructed and numerically simulated to assess the fluid dynamic performance from entropy generation loss coefficient. During the assessment of this hypothesis, design parameters such as blade angle (ϕ_{blade}), total-static expansion ratio (β_{t1}) and nozzle solidity (σ) are constrained within an error margin of 5% so as to enable a consistent comparison.

Upon analysis, it was concluded that there is an optimum value of post-expansion ratio ($\beta_{\text{opt, a1}}$) which corresponds to the best fluid dynamic performance for a set of design variables. Flow assessment of the optimum vane showed that the post-expansion region of the blade is characterized by two weak shock waves at the trailing edge while the other vane designs are characterized by strong shocks or expansion fans at the trailing edge along with boundary layer shock wave interaction at adjacent blades.

VARIATION OF OPTIMUM POST-EXPANSION RATIO WITH DESIGN VARIABLES

After the successful verification of the hypothesis, the framework was used to conduct a study for the sensitivity of the optimum value of post-expansion ratio ($\beta_{\text{opt, a1}}$) with respect to design variables. The primary design variables consisted of the blade angle (ϕ_{blade}) and total-static expansion ratio (β_{t1}) while the secondary design variable studied was the nozzle solidity (σ). From this study the following conclusions were drawn:

- $\beta_{\text{opt, a1}}$ increases with ϕ_{blade}. A loss breakdown of Δs_{2D} into the post-expansion (PE) and nozzle region entropy generation (Δs_{PE} and Δs_{nozzle}) indicated that Δs_{PE} is a quadratic function of the post-expansion ratio (β_{a1}) for each ϕ_{blade}. The optimum β_{a1} corresponding to Δs_{PE} is invariant with ϕ_{blade}. On the other hand, Δs_{nozzle} is a linearly decreasing function of β_{a1}. With increase in ϕ_{blade}, the slope of this linear function is found to be more negative. This means a higher β_{a1} leads to a lower Δs_{nozzle}. Hence for higher values of ϕ_{blade}, the optimum vane design expands more in the PE region, thus corresponding to a higher value of $\beta_{\text{opt, a1}}$. This forms the reasoning for an increase of optimum post-expansion ratio with respect to ϕ_{blade}.
- $\beta_{\text{opt, a1}}$ increases with β_{t1}. A loss breakdown of 2D loss into PE and nozzle loss showcases that for a higher β_{t1}, the PE loss contribution to 2D loss decreases. This means that for a higher β_{t1}, more expansion in the PE region leads to lower losses. This lower contribution of PE loss is due to lower mixing loss as calculated from the analytical correlation proposed by Denton [21].

- The effect of σ on the trend of $\beta_{\text{opt, a1}}$ is insignificant. 2D losses show a marginal increase with nozzle solidity but the trend of optimum post-expansion ratio is not definitive.

VARIATION OF OPTIMUM POST-EXPANSION RATIO WITH FLOW NON-IDEALITY

Numerical simulations of stator vanes with three sets of inlet conditions led to the conclusion that the optimum post-expansion ratio increases with non-ideality. The primary reason identified was the decrease in PE region loss contribution to the 2D loss. Further investigation led to two major observations which backed the primary reason. They are listed as:

- The separation bubble formed at the suction side of the adjacent blade due to the boundary layer-shock wave interaction shows a lower rise in entropy with non-ideality.
- The mixing loss coefficient computed is observed to decrease with non-ideality.

Both of these are observed in the post-expansion region thus reaffirming that with non-ideality, the post-expansion region loss contribution decreases.

VARIATION OF FLOW DEVIATION ANGLE WITH DESIGN VARIABLES

Flow deviation angle is an important design consideration in a supersonic regime because a greater flow deviation leads to more mixing losses and thus higher 2D losses. Their significance in incorporating into the design stage is higher in transonic-supersonic regime as compared to the highly subsonic flow regime [1]. Thus the variation of flow deviation angle corresponding to the optimum vane design was studied.

It is observed that if the working fluid undergoes more expansion in the post-expansion region, the stator exit flow loses flow turning which means the deviation angle tends towards a negative value. The reason for this observation is that the fluid at the pressure side of the trailing edge undergoes higher expansion as compared to the suction side due to formation of an expansion fan. This phenomena deflects the fluid exiting axially downwards. Thus with increase in ϕ_{blade}, as the optimum post-expansion ratio increases, the flow deviation angle became more negative. This trend was observed again with respect to total-static expansion ratio. With increase in the value of total-static expansion ratio, the flow deviation value for the optimum point became more negative. Thus it is concluded that with more expansion in the PE region, stator vanes lose flow turning.

The increase in the value of optimum post-expansion ratio with non-ideality, attributed to higher nozzle loss contribution, led to the conclusion that the flow deviation angle corresponding to the optimum vane design tends to more negative values with non-ideality.

FORMULATION OF DESIGN LAWS

The sensitivity analysis in the previous studies produced a trend of the optimum post-expansion ratio with design variables. Surrogate modeling was used to generate a second order polynomial with the design variables as inputs and the optimum M_{a} as output. M_{a} was selected to be the output parameter since it is more relevant to a designer. This fitted polynomial is the design correlation and mathematically it showcases a greater dependence of the optimum value of M_{a} on the blade angle and total-static expansion ratio as compared to nozzle solidity. A similar second degree equation relating blade angle to nozzle solidity, total-static expansion ratio and corrected blade angle was also generated.

5.2. RECOMMENDATIONS FOR FUTURE WORK

They are as following:

- **Use of Machine Learning to identify trends and correct low fidelity models**: The data generated from numerical experiments is significant and intelligent pattern recognition algorithms could be used to assist in identifying trends. The author suggests the use of Machine Learning algorithms to plug an overlook of information and highlight trends that could be difficult to identify by a human. This study makes use of RANS-SA turbulence model which is a low fidelity model that can generate trends in CFD simulation at the cost of accuracy. ML algorithms thus can be used to correct the RANS stress fields by training on flow data obtained from experiments or high fidelity models such as LES. This can then be used to improve the velocity/pressure fields and achieve more accuracy.

- **Further classification of Loss mechanisms**: The loss mechanisms were largely analyzed as nozzle and post-expansion losses. The mixing and shock losses were not analyzed separately and nor were the boundary layer and the BL-shock interaction loss. If this could be achieved, it would pave way for more understanding in the effect of shock waves on the trends. Hence, better shock capturing techniques to study shock-boundary layer interaction should be employed. In this work, traditional shock detection methods using the pressure contours have been employed. Advanced methods such as flow property gradients to detect for shock and expansion waves or a method based on characteristics can be employed [38].

- **Extending this study to the 3rd dimension and for radial flows**: This study performed is for a two dimensional stator blade which accounts for viscous dissipation, mixing, TE and shock losses within the expansion region. The existence of an optimum value of the post-expansion ratio has been proved for axial 2D stator blades. A stronger assertion of this hypothesis will be if this existence of $\beta_{\text{opt, a1}}$ is proved within the 3 dimensional domain too. The proposed study will be more complex due to the existence of secondary flows and end-wall losses. Nevertheless, taking into account these losses will give forth a more accurate design correlation which can then be compared with experimental results. Furthermore, this study can be extended to radial flows which is supposed to be the final objective. In the case of 3D radial stator vanes, isolating the effect of post-expansion ratio on loss coefficients will be challenging because of greater geometric and flow complexity.

- **Experimental study**: This study is performed under assumptions such as adiabatic walls and using equations of states which are essentially models themselves. The trend analysis and the design correlations proposed should be compared to the results from an experimental study under similar physical conditions. This would help in estimating the error percentage and improving the design correlations.

- **Statistical Indicators**: In this study, outliers in the trend of post-expansion ratio and loss coefficient were excluded manually. Thus, an automatic statistical analysis tool should be developed for such large amounts of data. This tool could help in excluding outliers and determining the uncertainty in the results and hence the observed trends.

BIBLIOGRAPHY

[1] M. Pini, *Lecture 5, 2018-2019, axial turbines,* https://brightspace.tudelft.nl/d2l/le/content/133558/viewContent/1230972/View, accessed on 2019-06-11.

[2] J. Giacaman, M. Pini, and N. Anand, *Design Guidelines for Radial Supersonic Stators,* (2018).

[3] P. Lampart, S. Yershov, A. V. Rusanov, and M. Szymaniak, *Tip leakage / main flow interaction in multi-stage hp turbines with short-height blading,* (2004).

[4] J. D. Denton and L. Xu, *The Trailing Edge Loss of Transonic Turbine Blades,* Journal of Turbomachinery **112**, 277 (1990).

[5] C. H. Sieverding, M. Stanislas, and J. Snoek, *Base Pressure Problem in Transonic Turbine Cascades.* American Society of Mechanical Engineers (Paper) **102**, 711 (1979).

[6] I. E. Agency, *World energy outlook, 2018,* https://webstore.iea.org/download/summary/190?fileName=English-WEO-2018-ES.pdf (2018), accessed on 2019-02-7.

[7] E. E. Commission, *Report from the commission to the european parliament and the council 2017 assessment of the progress made by member states towards the national energy efficiency targets for 2020 and towards the implementation of the energy efficiency directive as required by article 24(3) of the energy efficiency directive 2012/27/eu,* https://eur-lex.europa.eu/legal-content/EN/TXT/PDF/?uri=CELEX:52017DC0687&from=EN, accessed on 2019-02-7.

[8] T. Hung, T. Shai, and S. Wang, *A review of organic rankine cycles (ORCs) for the recovery of low-grade waste heat,* Energy **22**, 661 (1997).

[9] P. Colonna, E. Casati, C. Trapp, T. Mathijssen, J. Larjola, T. Turunen-Saaresti, and A. Uusitalo, *Organic Rankine Cycle Power Systems: From the Concept to Current Technology, Applications, and an Outlook to the Future,* Journal of Engineering for Gas Turbines and Power **137** (2015), 10.1115/1.4029884.

[10] H. Tabor and L. Bronicki, *Establishing criteria for fluids for small vapor turbines,* in *SAE Technical Paper* (SAE International, 1964).

[11] Enerdata, *Global energy statistical yearbook 2018,* https://yearbook.enerdata.net/total-energy/world-consumption-statistics.html (2018), accessed on 2019-02-7.

[12] A. Kluwick, *Internal flows of dense gases,* Acta Mechanica **169**, 123 (2004).

[13] E. Bufi and P. Cinnella, *Design methodology for supersonic orc turbine blades,* (2017).

[14] E. Rinaldi, R. Pecnik, and P. Colonna, *Unsteady operation of a highly supersonic Organic Rankine cycle turbine,* Journal of Turbomachinery **138** (2016), 10.1115/1.4033973.

[15] M. Deich, *Atlas of Axial Turbine Blade Cascades: By M.E. Deich, G.A. Filippov and L. Ya. Lazarev*, C.E. Trans. 4563-4564 (CEGB Information Services, 1965).

[16] N. Anand and M. Pini, *Design guidelines for supersonic radial stator vane operating with non-ideal flow conditions* . , 1 (2019).

[17] P. M. Schobeiri, ed., *Turbomachinery Flow Physics and Dynamic Performance* (Springer Berlin Heidelberg, Berlin, Heidelberg, 2005) pp. 1–12.

[18] J. Doe, *Fluid dynamic design of organic rankine cycle turbines,organic rankine cycle (orc) power systems: Technologies and applications,* (Elsevier Inc., 2016) pp. 253–297.

[19] J. D. Coull, *Endwall loss in turbine cascades,* Journal of Turbomachinery **139**, 1 (2017).

[20] S. L. Dixon and C. A. Hall, *Fluid Mechanics and Thermodynamics of Turbomachinery* (Elsevier, 2010).

[21] J. D. Denton, *Loss mechanisms in turbomachines,* Journal of Turbomachinery **115**, 621 (1993).

[22] J. Denton and N. Cumpsty, *Loss mechanisms in turbomachines.* (1987) pp. 1–14, cited By 13.

[23] J. Denton, *The trailing edge loss of trans-sonic turbine blades,* Journal of Turbo-machinery, Volume 112, Issue 2 (1989).

[24] C. Carcasci and R. Ferraro, *Thermodynamic optimization and off-design performance analysis of a toluene based rankine cycle for waste heat recovery from medium-sized gas turbines,* (2012).

[25] M. Oehlschlaeger, D. Davidson, and R. Hanson, *Thermal decomposition of toluene: Overall rate and branching ratio,* Proceedings of The Combustion Institute - PROC COMBUST INST **31**, 211 (2007).

[26] E. W. Lemmon and R. Span, *Journal of Chemical and Engineering Data*, Vol. 51 (2006) pp. 785–850.

[27] N. Anand, *Supersonic Turbine Design,* (2016).

[28] M. Zucrow and J. Hoffman, eds., *Gas Dynamics Vol. 1* (Wiley, 1976).

[29] D. Pasquale, A. Ghidoni, and S. Rebay, *Shape optimization of an organic rankine cycle radial turbine nozzle,* Journal of Engineering for Gas Turbines and Power **135**, 042308 (2013).

[30] L. Piegl and W. Tiller, *The NURBS Book* (1995).

[31] T. D. Economon, F. Palacios, S. R. Copeland, T. W. Lukaczyk, and J. J. Alonso, *SU2: An open-source suite for multiphysics simulation and design,* AIAA Journal **54**, 828 (2016).

[32] M. Pini, S. Vitale, P. Colonna, G. Gori, A. Guardone, T. Economon, J. J. Alonso, and F. Palacios, *SU2: The Open-Source Software for Non-ideal Compressible Flows,* Journal of Physics: Conference Series **821** (2017), 10.1088/1742-6596/821/1/012013.

[33] J. S. Lopez-Echeverry, S. Reif-Acherman, and E. Araujo-Lopez, *Peng-Robinson equation of state: 40 years through cubics,* Fluid Phase Equilibria (2017), 10.1016/j.fluid.2017.05.007.

[34] S. Hickel, *Lecture 5, 2017-2018, rans - cfd for aerospace engineers,* https://brightspace.tudelft.nl/d2l/le/content/133552/viewContent/1044780/View, accessed on 2019-06-11.

[35] C. . A. P. M. at SimScale GmbH, *What is y+,* `https://www.simscale.com/forum/t/what-is-y-yplus/82394`, accessed on 2019-011-11.

[36] E. W. Lemmon and R. Span, *Short fundamental equations of state for 20 industrial fluids,* Journal of Chemical & Engineering Data **51**, 785 (2006), https://doi.org/10.1021/je050186n .

[37] scikit-learn developers, *An introduction to machine learning with scikit-learn,* `https://scikit-learn.org/stable/tutorial/basic/tutorial.html`, accessed on 2020-03-01.

[38] W. Ziniu, X. Yizhe, W. Wenbin, and R. Hu, *Review of shock wave detection method in cfd post-processing,* Chinese Journal of Aeronautics **26** (2013), 10.1016/j.cja.2013.05.001.

Appendices

A

MESHING OF GEOMETRY

A.1. TOOL

The tool used for meshing of the geometry is UMG2 which creates unstructured and hybrid mesh grids in two dimensions. In this work, a hybrid mesh has been created using this tool. A hybrid grid is a combination of unstructured and structured portions. The boundary layer and the trailing edge is captured using a structured grid as they have higher resolution as compared to unstructured grids.The remaining flow domain is meshed with an unstructured grid. This can be seen distinctly in the figure 3.8a.

A.2. INPUT PARAMETERS

The meshing tool requires a number of input files, the most important being the *geometry* file. This file is used to set up the domain, the surfaces it consists and the blade co-ordinates (in case of turbo-machinery). A supplementary file called the *spacingcontrol.stator* file is used to provide the co-ordinates of the trailing edge of the stator and the axial pitch. Lastly, an *options* file is used to give the input for whether the geometry is Periodic or not, number of boundary layers, boundary layer thickness and whether the mesh is hybrid or not. All these input files combined are used to first make the geometry, set up the mesh sizing parameters, set the general mesh parameters and finally create the 2D mesh.

A.3. QUALITY OF MESH

The quality of a mesh can be judged based on Skewness, smoothness and the aspect ratio of individual cells. For tetrahedral cells, the skewness is defined as:

$$\text{skewness} = \frac{\text{optimal cell size - cell size}}{\text{optimal cell size}} \tag{A.1}$$

while for a quad:

$$\text{skewness} = \max\left[\frac{\theta_{\max} - 90}{90}, \frac{90 - \theta_{\min}}{90}\right] \tag{A.2}$$

Regarding smoothness, the change in cell size with respect to the adjacent cell should be smooth, as sudden jumps in the cell size might cause erroneous results in the nearby nodes. In case of the aspect ratio, it is the ratio of the longest to the shortest side of the cell. to ensure best results it should be one. A large aspect ratio in the mesh, could lead to large interpolation errors.

A.4. GRID INDEPENDENCE STUDY

A grid independence study was performed so as to ensure the discretization and solution errors were small enough after sufficient number of iterations. The procedure to perform a grid independence study is to refine the mesh and compare the solutions to coarse meshes. Due to the presence of a large number of geometries, this study was carried out for one nozzle solidity=1.75 and four stator outlet flow angles - 66°, 71°, 76° and 81°. This design parameter changes the meshing domain the most, hence the author considers exploring these four meshes a sufficient representation of the entire design space. The DoD is chosen as the median

of the DoD design space and the target variable for the independence study is chosen as the entropy generation coefficient. The figure A.1 showcases the variation of the converged value of the ζ_{2D} with respect to the number of elements. Higher the number of elements, more is the mesh said to be refined.

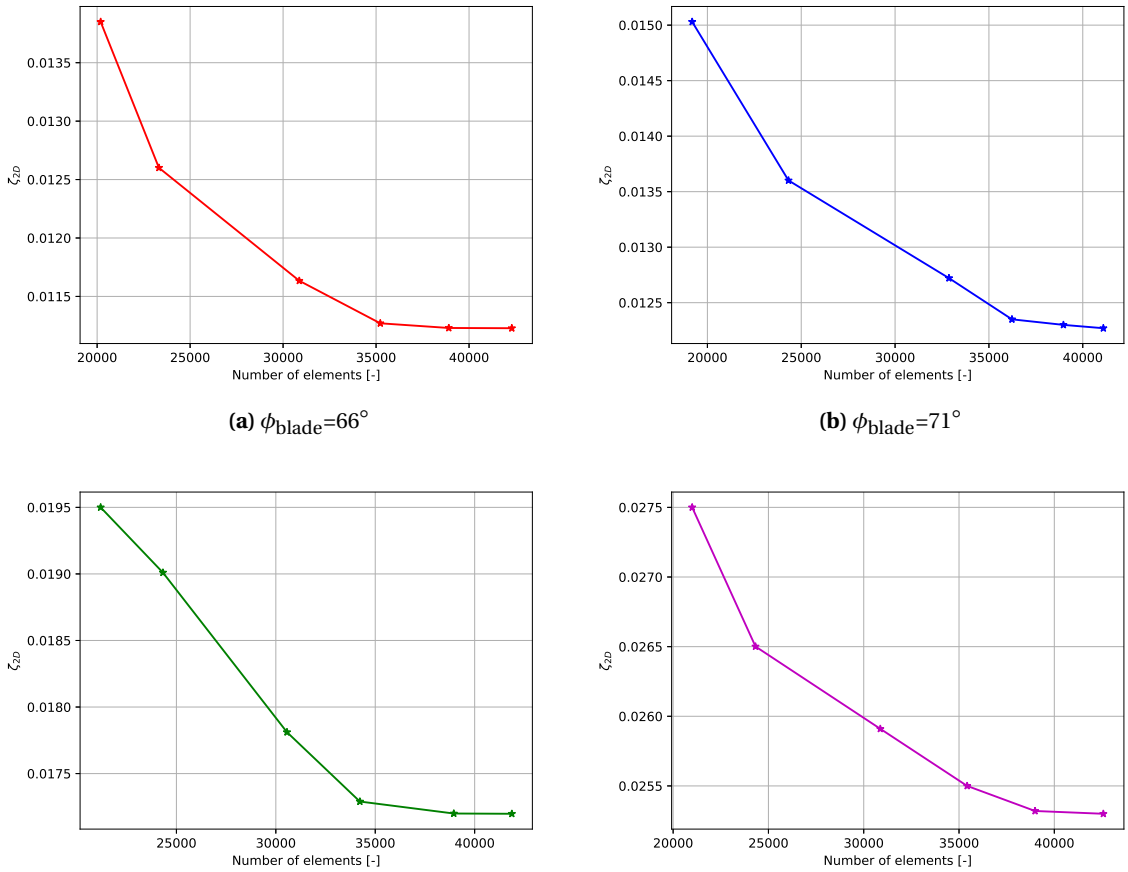

(a) ϕ_{blade}=66°

(b) ϕ_{blade}=71°

(c) ϕ_{blade}=76°

(d) ϕ_{blade}=81°

Figure A.1: Convergence of target variable of entropy generation loss coefficient wrt. mesh refinement for $\phi_{\text{blade}} \in [66, 71, 76, 81]°$

B

NOZZLE SOLIDITY DEFINITION

The nozzle solidity definition is slightly involved. The procedure is elaborated through the figure B.1. The equation used is:

$$\text{Nozzle solidity} = \frac{\textbf{chord}}{\textbf{pitch}} = \frac{\text{chord}}{A_o} \times \frac{A_o}{A_a} \times \frac{A_a}{\text{pitch}} = \text{Nozzle Aspect Ratio} \times \frac{1}{\text{DoD}} \times \cos(\phi_{\text{blade}}) \tag{B.1}$$

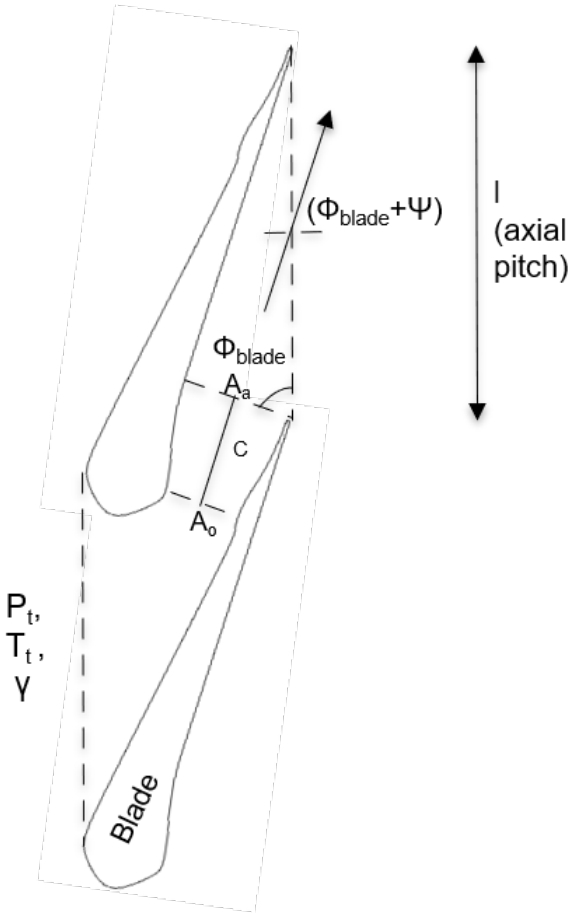

Figure B.1: Schematic diagram of the flow domain for derivation of nozzle solidity expression.

C

INPUT CONFIGURATION FILES

C.1. AST CONFIGURATION

```
TOOL_TYPE = SSS

## What kind of Stator RADIAL or AXIAL
STATOR_KIND = AXIAL
outFileMoc = Nozzle_coords.out

### Stator DESIGN Parameters ###
nBlades = 18
AxialPitch= 0.061898506
radiusOut = 0.11908
 kernelRadiusRatio = 1
ActualRin = 0.1685
ActualRout = 0.11908
RealRout = 0.11
ScaleNoz = 8
TEminT = 0.0005
ScaleMax = 50
```

Geometrical constraints X

```
Mode Simulation_Loop # Simulation_Loop # Visualization

flowAngle =  XXXXXXX #81
```

Blade Design Parameter

```
### MESH ###
ScaleMesh = 10
nPointsScale = 2
CoordsName stator_coords.out
UMG2Name stator

### PLOT ###
plotName Stator_boundaries.eps
SpecsName stator_specs.out
nBldPlt = 2
```

C.2. MOC CONFIGURATION

```
TOOL_TYPE = MOC

# 'CoolProp' = Perfect Gas, EoS = Equation of State,
 EoS_TAB = Using Table, CoolProp = CoolProp
GAS_EQU CoolProp
FLDNAME = Toluene

# REAL GAS PROP - SI Units (Toluene) (ref: Wiki)
Tc = 591.79   #591.79        # K
Pc = 4.109e6#2.09e6        # Pa
Vc = 0.000316           # m^3/mol
M = 0.09214  #0.09214            # kg/mol
To = 580       # K
Po = 31.95e5       # Pa
R = 8.314           # mol/Kg/K
Ho = 676.019            # J/Kg
so = 0.9
gamma = 1.055          # cnst
```

Inlet Conditions

```
# Input: Throat Design
rho_t YYYYYYY
y_t 1
rho_d YYYYYYY
n 10
tolerance_v 1e-6  # 1e-3 -> Best result
tolerance_x 1e-6       # 1e-3 -> Best result

#
dtau 0.01          # 0.2 # 1.0 -> Best Result
```

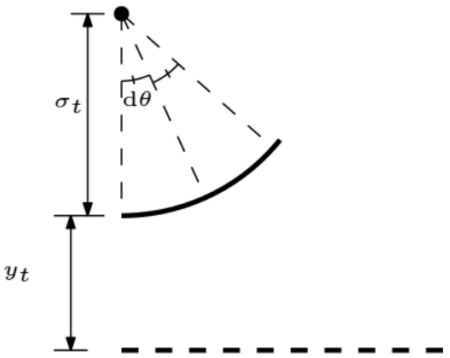


```
#Reflex:
n_ref = 40
```

```
# Design Output: Output Mach Number
Noz_Design_Mach  XXXXXXX
```

Primary Design Parameter for nozzle

```
# PlotResults: Plotting Results
PlotResults = YES # YES/NO
File_Name_Plot moc.png

# WriteData: Writing Variables
File_Name_NProp Nozzle_prop.out
VAR x y u v M rho SoS T P
File_Name_NCods Nozzle_coords.out
```

Output Files

C.3. CFD CONFIGURATION

The CFD configuration file has described in detail in the SU2 website.

As described in section 3.4.2, the RANS solver is used with the one-equation Spallart Almaras turbulence model used to model the Reynolds stress tensor. The inlet total Pressure, Temperature and free stream density are given as inputs. For the boundary conditions at the inlet and outlet, Riemann or reflecting boundary conditions have been imposed. The gradients of the convective term in the equation 3.6 are approximated using the ROE numerical method which employs MUSCL_FLOW to attain second order accuracy in the spatial domain. This ensures that the solution does not oscillate due to discontinuities from shock waves in the flow. A linear approximation is used to calculate the value of the conserved variable at the face of the discretized cell. The linear approximation is given by:

$$\phi_f = \phi_p + \psi_p \delta\phi_p \mathbf{x}_f \tag{C.1}$$

where ψ_p is the slope limiter function that is used to remove discontinuity. The slope limiter reduces the gradient at every discrete cell such that the monotonicity of the conserved values as compared to the neighboring cells is maintained. The slope limiter used in this case is the VAN_ALBADA_EDGE. The target variable for convergence was rho_energy and the minimum order of magnitude for acceptable convergence was selected as 4 orders beneath the initial value.

D

ADDITIONAL RESULTS

D.1. SEMI-IDEAL CASE

The second order polynomial for ψ and $M_{\text{a,opt}}$ are of the form:

$$\psi = a_0 + p(\sigma) + q(\beta_{01}) + r(\phi_{\text{blade}}) + s(\sigma^2) + v(\beta_{01}^2) + x(\phi_{\text{blade}}^2) + t(\sigma\beta_{01}) + r(\sigma\phi_{\text{blade}}) + w(\beta_{01}\phi_{\text{blade}}) \quad \text{(D.1)}$$

The coefficients for equation D.1 are listed in the table D.1. Value of a_0 is equal to 1.9278.

Table D.1: Polynomial fit coefficients for flow and blade angle relation

Coeff.	Value	Coeff.	Value	Coeff.	Value
p	8.68e-3	**q**	-5.79e-4	**r**	-4.638
s	-2.94e-3	**t**	-5.663e-3	**u**	2.477e-3
v	-8.108e-3	**w**	1.114e-1	**x**	2.523

$$M_{\text{a,opt}} = a + b(\sigma) + c(\beta_{01}) + d(\phi_{\text{blade}}) + e(\sigma^2) + h(\beta_{01}^2) + j(\phi_{\text{blade}}^2) + f(\sigma\beta_{01}) + g(\sigma\phi_{\text{blade}}) + i(\beta_{01}\phi_{\text{blade}}) \quad \text{(D.2)}$$

The constants of the equation D.2 are showcased in the table D.2. Once this step was completed, the 3D contour plot was created using the interpolated values and is visualized in the figure D.1.

Table D.2: Polynomial fit coefficients

Coeff.	Value	Coeff.	Value	Coeff.	Value
b	9.39e-5	**c**	-1.76e-2	**d**	6.009e-2
e	-6.59e-5	**f**	-9.963e-3	**g**	2.878e-3
h	-2.364e-2	**i**	3.141e-3	**j**	-5.653e-4

a is the intercept. It's value is equal to -4.086. From the table D.2, it can be seen that the optimum M_a varies strongly with β_{t1} and ϕ_{blade}, while the variation with σ is diminished. This is also observed in the 3D contour plot D.1. If the axis of ϕ_{blade} is observed, with increasing ϕ_{blade}, the optimum M_a decreases, signaling an increase in the optimum β_{a1}. With increasing β_{t1}, the optimum M_a increases but the trend of β_{a1} cannot be concluded from this as the stator outlet pressure and hence the M_1 is different. With σ, the change in M_a is almost negligible.

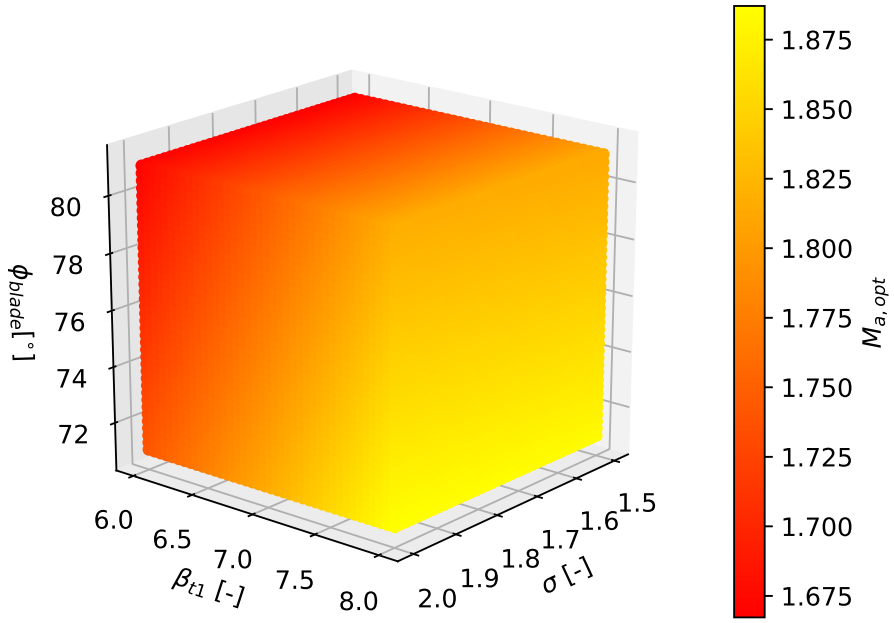

Figure D.1: Optimum M_a with σ, ϕ_{blade}, β_{t1} for the semi-ideal case where Z [0.74, 0.94]

D.2. NON-IDEAL CASE

The coefficients for equation 4.13 are listed in the table 4.8. Value of a_0 is equal to 1.9068.

Table D.3: Polynomial fit coefficients for flow and blade angle relation

Coeff.	Value	Coeff.	Value	Coeff.	Value
p	8.68e-3	**q**	-5.79e-4	**r**	-4.638
s	-2.94e-3	**t**	-5.663e-3	**u**	2.477e-3
v	-8.108e-3	**w**	1.114e-1	**x**	2.523

$$M_{\text{a,opt}} = a + b(\sigma) + c(\beta_{01}) + d(\phi_{\text{blade}}) + e(\sigma^2) + h(\beta_{01}^2) + j(\phi_{\text{blade}}^2) + f(\sigma\beta_{01}) + g(\sigma\phi_{\text{blade}}) + i(\beta_{01}\phi_{\text{blade}}) \quad \text{(D.3)}$$

The constants of the equation D.3 are showcased in the table D.4. Once this step was completed, the 3D contour plot was created using the interpolated values and is visualized in the figure 4.26.

Table D.4: Polynomial fit coefficients

Coeff.	Value	Coeff.	Value	Coeff.	Value
b	-9.748e-5	**c**	-4.077e-2	**d**	7.587e-2
e	-4.343e-5	**f**	-3.663e-3	**g**	2.477e-3
h	-1.364e-3	**i**	-6.141e-4	**j**	-4.523e-4

a is the intercept. It's value is equal to -4.612. From the table D.4, it can be seen that the optimum M_a varies strongly with β_{t1} and ϕ_{blade}, while the variation with σ is diminished. This is also observed in the 3D contour plot D.2. If the axis of ϕ_{blade} is observed, with increasing ϕ_{blade}, the optimum M_a decreases, signaling an increase in the optimum β_{a1}. With increasing β_{t1}, the optimum M_a increases but the trend of β_{a1} cannot

be concluded from this as the stator outlet pressure and hence the M_1 is different. With σ, the change in M_a is almost negligible.

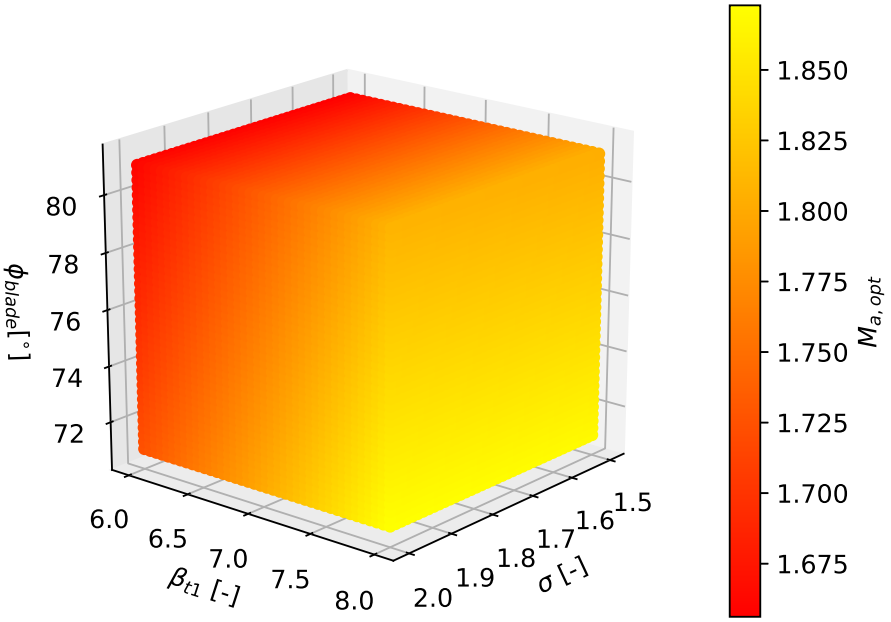

Figure D.2: Optimum M_a with σ, ϕ_{blade}, β_{t1} for the non-ideal case where Z [0.57, 0.92]